STUDY OF MAGNETIC, THERMAL AND DIELECTRIC PROPERTIES OF SOME RARE-EARTH BASED OXIDES

By

Moumita Das

PHYS05201504008

Condensed Matter Physics Division

Saha Institute of Nuclear Physics, Kolkata

A thesis submitted to the
Board of Studies in Physical Sciences

In partial fulfillment of the requirements

For the Degree of

DOCTOR OF PHILOSOPHY

of

HOMI BHABHA NATIONAL INSTITUTE

JUNE 2020

Homi Bhabha National Institute

Recommendations of the Viva Voce Board

As members of the Viva Voce Board, we recommend that the dissertation prepared by **Moumita Das** entitled **"Study of magnetic, thermal and dielectric properties of some rare-earth based oxides"** may be accepted as fulfilling the dissertation requirement for the Degree of Doctor of Philosophy.

-- **Date :**
Chairman : Prof. Pradeep Kumar Mohanty

-- **Date :**
Guide : Prof. Prabhat Mandal

-- **Date :**
Member : Prof. Biswajit Karmakar

-- **Date :**
Member : Prof. Satyaranjan Bhattacharya

-- **Date :**
Member : Prof. Dipten Bhattacharyya

-- **Date :**
External Examiner : Prof. K. G. Suresh

Final approval and acceptance of this dissertation is contingent upon the candidate's submission of the final copies of the dissertation to HBNI.

I hereby certify that I have read this dissertation prepared under my direction and recommend that it may be accepted as fulfilling the dissertation requirement.

-- **Date :**
Guide : Prof. Prabhat Mandal

STATEMENT BY AUTHOR

This dissertation has been submitted in partial fulfillment of requirements for an advanced degree at Homi Bhabha National Institute (HBNI) and is deposited in the library to be made available to borrowers under rules of the HBNI.

Brief quotations from this dissertation are allowable without special permission, provided that accurate acknowledgement of source is made. Requests for permission for extended quotation from or reproduction of this manuscript in whole or in part may be granted by the Competent Authority of HBNI when in his or her judgment the proposed use of the material is in the interests of scholarship. In all other instances, however, permission must be obtained from the author.

Moumita Das

DECLARATION

I, hereby, declare that the investigation presented in the thesis has been carried out by me. The work is original and the work has not been submitted earlier as a whole or in part for a degree/diploma at this or any other Institution or University.

Moumita Das

To my parents and husband

ACKNOWLEDGEMENTS

First, I would like to express my gratitude to my thesis supervisor Prof. Prabhat Mandal, Saha Institute of Nuclear Physics, Kolkata. It would not been possible to complete my thesis without his advise and constant support throughout my Ph.D. His encouragement, guidance and discussion during my Ph.D tenure able me to get the success of my thesis. It was a pleasure working environment with all of my lab mates. I am very much thankful to my seniors, Dr. Arnab Kumar Pariari, Dr. Ratnadeep Singha and Dr. Arup Ghosh from whom I was accustomed to handle the instruments in the Lab. Dr. Nazir Khan, Dr. Arindam Midya, Dr. Prasenjit Sarkar, Dr. Moumita Nandi and Dr. Prithwis Dutta are also thanked for various fruitful discussion whenever I have needed in my research. They really helped me when I have asked any of my quires. I would like to express special thanks to my senior Dr. Susmita Roy. I have really enjoyed her company and friendliness behaviour during my Ph.D. My friend Shubhankar Roy and two of my juniors Suchanda Mandal and Shubhankar Purkait helped me in various ways in the lab during my research. Due to their friendly behaviour the work culture of our lab was very nice. I like to give special thank to Mr. Arun Kumar Paul for his technical help while performing the experiments. With his assist I would able to reconstruct the experimental set up whenever I had need urgently. I acknowledge all the members of the Condensed Matter Physics division, SINP and workshop of our institute for heir help at various level. I am very thankful to SINP, Department of atomic energy, Government of India for financial support for caring out my doctoral work. I have expressed my thanks to my Post M.Sc friend Diboshree Choudhury to overcome my stress in various way in my Ph.D tenure. Finally, my deepest gratitude to my family, without whom this thesis would not possible. My parent's constant support and encouragement for higher studies and also some times their scarifies in various thing help me to achieve my doctoral work. The unconditional psychological support and mental boost of my husband as well as my friend Ashis Koley helps me to overcome the various difficulties during my Ph.D.

List of Publications

A. Published journal articles included in PhD thesis

1. “Anomalous magnetic properties of $RCrTiO_5$ (R=Dy and Ho) compounds”, **Moumita Das**, Susmita Roy, Krishnan Mahalingam, V. Ganesan and Prabhat Mandal, *Journal of Physics: Condensed Matter,* 32, 035802 (2020).

2. “Giant magnetocaloric effect in an exchange-frustrated $GdCrTiO_5$ antiferromagnet”, **M. Das**, S. Roy, N. Khan and P. Mandal, *Physical Review B,* 98, 104420 (2018).

3. “Giant reversible magnetocaloric effect in a multiferroic $GdFeO_3$ single crystal”, **M. Das,** S. Roy, and P. Mandal, *Physical Review B,* 96, 174405 (2017).

4. “Non-Griffiths-like cluster formation in double perovskite Gd_2CoMnO_6: Evidence from critical behaviour”, **Moumita Das**, Prosenjit Sarkar and Prabhat Mandal, *Physical Review B,* 101, 144433 (2020).

5. “Nonlinear Magnetodielectric and Magnetocaloric properties of Double Perovskite Ho_2FeCoO_6”, **Moumita Das** and Prabhat Mandal, *Physica B*, 571, 32-35 (2019).

B. Conference papers/presentations included in PhD thesis

1. “Nonlinear Magnetodielectric and Magnetocaloric properties of Double Perovskite Ho2FeCoO6”, **Moumita Das** and Prabhat Mandal, presented in *International Conference on Magnetic Materials and Applications (ICMAGMA-2018).*

2. “Giant magnetocaloric effect in an exchange-frustrated $GdCrTiO_5$ antiferromagnet”, **Moumita Das,** Susmita Roy, Nazir Khan and Prabhat Mandal, presented in *Condensed Matter Days 2018.*

3. “Giant reversible magnetocaloric effect in a multiferroic $GdFeO_3$ single crystal”, **Moumita Das**, Susmita Roy and Prabhat Mandal, presented in *International Conference on Condensed Matter Physics (organized by ISI, Kolkata, 2017).*

4. “Large magnetic entropy changes in multiferroic $HoFeO_3$ single crystal”, **Moumita Das** and Prabhat Mandal, presented in *62nd DAE Solid State Physics Symposium (organized by Department of Atomic Energy, Govt. of India)* The Proceeding has been published in AIP Conference Proceedings 1942, 140007 (2018).

5. “Magnetic properties of $GdFeO_3$ single crystal”, **Moumita Das**, Susmita Roy and Prabhat Mandal, presented in *Condensed Matter Days 2017.*

C. Accepted journal articles included in PhD thesis

NIL

D. Under Review journal articles included in PhD thesis

NIL

E. Other journal articles not included in PhD thesis

1. “Large low-field magnetic refrigeration in ferromagnetic insulator $EuTi_{0.9}V_{0.1}O_3$”, S. Roy, **M. Das**, and P. Mandal, *Physical Review Materials,* 2, 064412 (2018).

2. “Effect of hydrostatic pressure on ferromagnetism in two-dimensional CrI_3”, Suchanda Mondal, Murugesan Kannan, **Moumita Das**, Linganan Govindaraj, Ratnadwip Singha, Biswarup Satpati, Sonachalam Arumugam, and Prabhat Mandal, *Physical Review B* 99, 180407(R) (2019).

3. “Enhanced Magnetic Properties of In-Mn-Codoped Plasmonic ZnO Nanoflowers: Evidence of Delocalized Charge Carrier-Mediated Ferromagnetic Coupling”, Sumana Paul, Biswajit Dalal, **Moumita Das**, Prabhat Mandal, and Subodh Kumar De, *Chemistry of Materials*, 31, 8191-8204 (2019).

4. “Unveilling ferrimagnetic ground state, anomalous behaviour of the exchange-bias field around spin reorientation, and magnetoelectric coupling in YbCr1-xFexO3 ($0.1 \leq x \leq 0.6$)”, Biswajit Dalal, Babusona Sarkar, S Rayaprol, **Moumita Das**, V. Siruguri, Prabhat Mandal, and Subodh Kumar De, *Physical Review B,* 101, 144418 (2020).

Contents

SYNOPSIS

Introduction: Among various kinds of magnetic oxides, the rare-earth transition metal based ones are more interesting for their fascinating properties which are important from fundamental point of view as well as for technological applications like in magnetic refrigeration [1], magnetic switching [2], magnetic storage [3] and spintronic devices [4], etc. In last few decades, manganites and cobaltites are extensively investigated for their rich phase diagram and colossal magnetoresistive properties [5]. On the other hand, rare-earth (R) ortho-ferrites RFeO$_3$ (RFO) [2], orthochromates RCrTiO$_5$ (RCTO) [6] and double perovskites $R_2MM\prime O_6$ (M and $M\prime$ are the transition metals) [7] are relatively less studied. The complex interplay of R^{3+} and M^{3+} sublattices, antisymmetric Dzyaloshinskii–Moriya (DM) interaction [8], single-ion anisotropy [9] and magnetic frustration [10] are the main ingredients for their rich physical properties. In this thesis work, I have investigated the role of single-ion anisotropy and DM interaction on exotic magnetic properties of RCTO [11]and RFO series of compounds. The contribution of exchange frustration in enhancing the magnetocaloric properties of GdCrTiO$_5$ compound has been investigated [12]. The single crystal of RFeO$_3$ has been studied as a potential magetocaloric material [13]. The critical magnetic behavior of double perovskite Gd$_2$CoMnO$_6$ [14] and the magnetodielectric properties of Ho$_2$FeCoO$_6$ have also been explored [15] .

Experimental Details: The pollycrystalline RCrTiO$_5$ (R=Dy, Ho and Gd) and $R_2MM\prime O_6$ (R=Gd and Ho, M=Co and Fe and $M\prime$=Mn and Co) have been synthesized by standard solid state reaction method. The single crystals of RFeO$_3$ (R=Gd and Ho) were grown in a four-mirror floating zone furnace. Phase purity and the structural analysis have been done using high-resolution powder x-ray

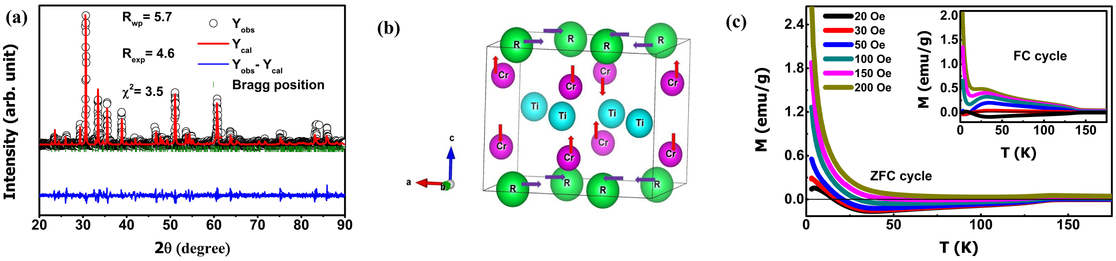

Figure 1: (a) The XRD pattern of DyCrTiO$_5$ as a representative and (b) schematic magnetic structure of the RCrTiO$_5$ where the arrow indicates the spin of the two sublattices and (c) the main panel shows $M(T)$ for ZFC mode and inset shows for FC mode of DyCrTiO$_5$ compounds.

diffraction (XRD). We did not observe any peak due to an impurity phase in the studied compounds. The quality and orientation of the crystals were determined by the Laue diffraction technique. The magnetic measurements were done in a 7 T MPMS3. The heat capacity (C_p) and thermal conductivity were measured in a 9 T physical property measurement system. The dielectric properties have been measured in a 9 T cryogen free commercial system.

Anomalous magnetic properties of RCrTiO$_5$ (R=Dy and Ho) compounds: There are very few reports on physical properties of RCrTiO$_5$ series, the daughter compounds of well known multiferroics RMn$_2$O$_5$ [16]. In order to understand the complex magnetic behavior of RCrTiO$_5$ series, for the first time, we have successfully synthesized two unexplored compounds DyCrTiO$_5$ (DCTO) and HoCrTiO$_5$ (HCTO) and studied their magnetic and thermodynamic properties in details over wide range of temperature and magnetic field. In Fig. 1(a), the x-ray diffraction pattern of DyCrTiO$_5$ is shown, as a representative. The schematic magnetic structure of RCrTiO$_5$ is shown in Fig. 1(b) with possible spin configuration for R^{3+} and Cr^{3+} sublattices. The temperature dependence of low-field ($H \leq$200 Oe) dc magnetization M for DyCrTiO$_5$ has been measured both under zero-field-cooled (ZFC) and field-cooled (FC) mode [Fig. 1(c)]. It is clear from

Fig. 1(c) that, depending on temperature and field strength, M can be positive as well as negative. Also, the nature of $M(T)$ curves for various fields in ZFC mode is quite different from the corresponding FC mode. In Fig. 2(a), the complex nature of $M(T)$ has been displayed pictorially along with the relative orientation of Dy^{3+} and Cr^{3+} spins. Due to the antisymmetric nature of DM interaction, antiferromagnetic ordering of Cr^{3+} moments with a weak ferromagnetic (FM) component has been observed below 140 K. $M(T)$ curve shows a broad maximum near 4.5 K but this anomaly is not due to the long-range antiferromagnetic (AFM) ordering of Dy^{3+} moments as evident from heat capacity. Anisotropic exchange between Dy^{3+} and Cr^{3+} spins creates an effective magnetic field at Dy^{3+} sites. Above 4.5 K, M decreases rapidly due to the faster decrease of Dy^{3+} moment and the net M becomes zero close to 16 K, this is the compensation temperature T_{comp1} and above T_{comp1}, M becomes negative. Again, M becomes zero at T_{comp2} and positive for $T > T_{comp2}$. Near T_{SR}=37 K, the Cr^{3+} moments reorient their spins. A small fraction of spins aligns along the direction of applied magnetic field, as a result M is positive for 100 Oe in FC mode but the M is still negative for ZFC mode. So the role of single-ion anisotropy is more clearly manifested in ZFC mode as shown in Fig. 2(b). For high field at 500 Oe, M is positive over the entire temperature range, i.e., no compensation in magnetization occurs. With the increase in magnetic field strength, T_{comp1} and T_{comp2} shift toward higher and lower temperature, respectively and they merge at $H\sim$200 Oe to a value 80 K as shown in the inset of Fig. 2(b). The $M(T)$ curve in ZFC mode as well as for FC mode is shown in Fig. 2(c) for the second compound HCTO. The nature of $M(T)$ curve for HCTO is qualitatively similar to that for DCTO, except the absence of spin reorientation phenomenon. The anomalies are observed at T_N^{Cr} (=140 K) and T_{comp}=128 K in

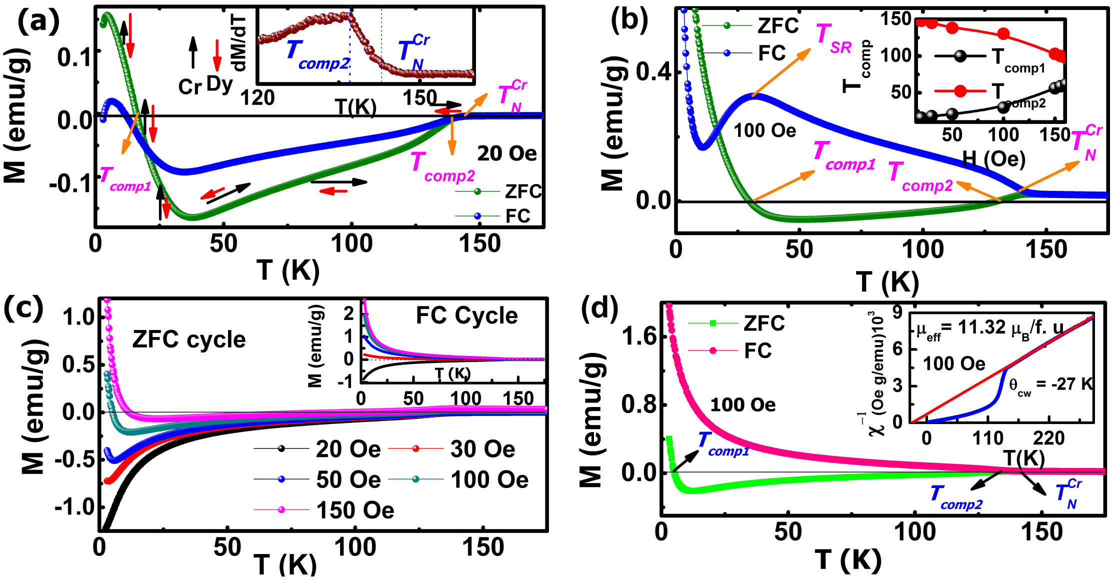

Figure 2: (a) The main panel shows the $M(T)$ curve at 20 Oe. The red and black arrows indicate the moment of Dy and Cr, respectively and the length of the arrow denotes the value of the net moment. The inset shows the derivative of moment with temperature near ${T_N}^{Cr}$ and T_{comp}. (b)The main panel shows the $M(T)$ at 100 Oe and inset shows the variation of T_{comp1} and T_{comp2} with magnetic field of DCTO. (c) The main panel shows temperature dependence of magnetization at low fields (20–150 Oe) in ZFC mode and the inset shows same plot for FC mode for HCTO compound. (d) The main panel shows the $M(T)$ at 100 Oe and inset shows the Curie–Weiss plot for HCTO compound for 100 Oe.

both ZFC and FC modes. For 100 Oe, M tends to be positive in ZFC cycle and in FC cycle it is positive below 15 K as depicted in Fig. 2(d). The crucial parameter that should be taken into account to compare and contrast the magnetic ground state of these two systems is the single-ion anisotropy of rare-earth ions which is three times larger in Dy^{3+} than in Ho^{3+} [17]. Above 150 K, χ follows the Curie-Weiss law $\chi(T)= C/(T - \Theta_{CW})$ as shown in inset of Fig. 2(d). The calculated value of θ_{CW} is -27 K, indicating the AFM interaction is dominating for HCTO. To confirm the above mention phase transitions the heat capacity has been measured for both the samples down to 1.8 K. Fig. 3(a) shows the $C_p(T)$

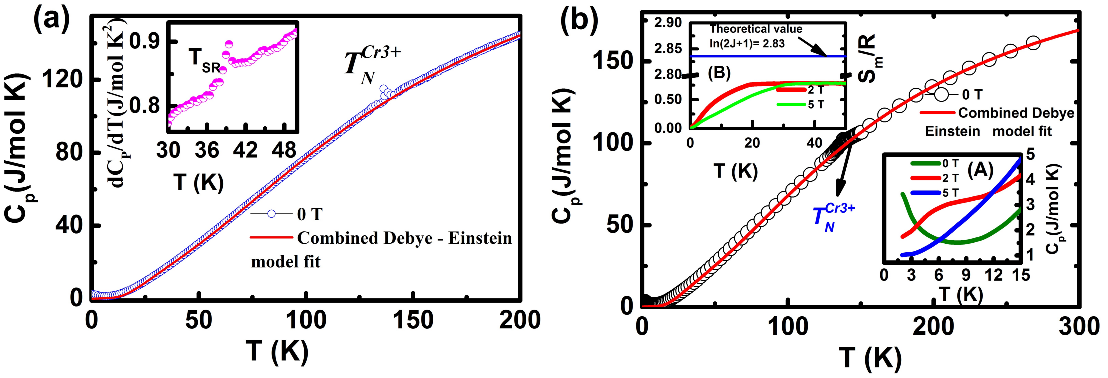

Figure 3: (a)The main panel shows the zero field C$_p$ and inset shows anomaly near T_{SR} for DCTO and (b) the main panel shows the zero field C$_p$ where red curve is combined Debye Einstein model fitting and inset (A) shows the field dependence heat capacity and (B) shows magnetic entropy for HCTO.

for DCTO where a peak has been observed at T_N^{Cr} (=140 K) but no λ - like peak has been observed due to the long range ordering (LRO) of the Dy^{3+} down to 1.8 K. Also we did not observe any anomaly near T_{SR} but dC$_p(T)$/dT shows a weak anomaly at T_{SR} as shown in inset of Fig. 3(a) this suggests that spin reorientation is a very weak thermodynamic phenomenon for this compound. Fig. 3(b) shows $C_p(T)$ for HCTO where a peak has been seen at T_N^{Cr} (=137 K) and the $C_p(T)$ decreases below T_N^{Cr}. C_p exhibits an upturn below 7 K but no peak. With application of magnetic field the upturn suppresses while C_p increases in the high temperature region, as a result the magnetic entropy shifts towards higher temperature as shown in inset (A) of Fig. 3(b). The calculated normalized value of entropy is five times smaller than the theoretical value 2.83 as shown in inset B of Fig. 3(b) for HCTO. The main panel of Fig. 4(a) shows $M(H)$ curve at some selective temperatures for DCTO as a representative compound. The inset (A) of Fig. 4(a) shows $M(H)$ at 130 K which is slightly below T_N^{Cr} and exhibits a weak hysteresis at low fields while it is almost linear at high fields, like a typ-

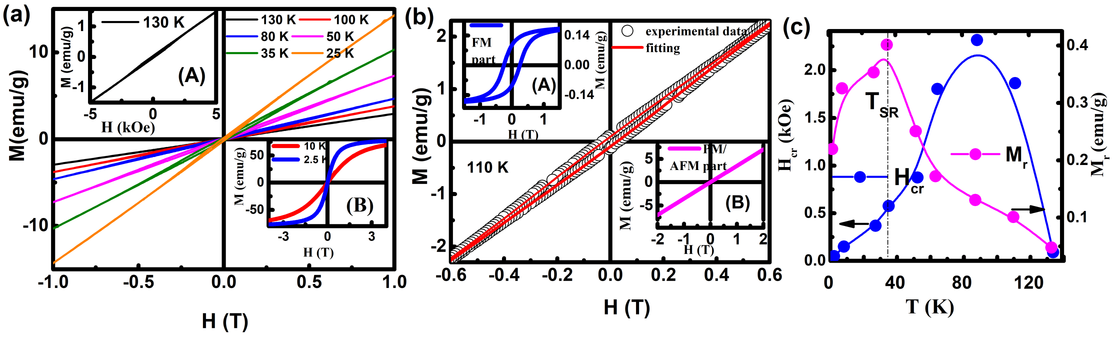

Figure 4: (a) The main panel shows the $M(H)$ plot of some selective T and inset (A) shows the $M(H)$ near T_N^{Cr} and (B) at low T. (b) The main panel shows the fitting of SC expression on $M(H)$ and insets (A) and (B) shows FM and AFM contribution respectively. (c) Shows the temperature dependence of H_{cr} and M_r for DCTO.

ical canted AFM [18]. Inset (B) shows the $M(H)$ loop for well below T_N^{Cr}. The value of saturation magnetization is 6.3 μ_B/f.u and 7.4 at 2 K and 7 T for DCTO and HCTO respectively. The experimental values of saturation moment for both DCTO and HCTO are significantly smaller than the theoretical values of the free Dy^{3+} and Ho^{3+}. This discrepancy is due to the strong single-ion anisotropy. To determine the contribution of FM and AFM/PM counterparts to the total $M(H)$ we have fitted the measured $M(H)$ data to Stearns and Cheng (SC) expression [19], $M(H)$=$(2M_s/\pi)\tan^{-1}[(H \pm H_{cr})/H_{cr}(\tan\pi$ S$)/2] + \chi H$, where the first term is the FM hysteresis loop and the second term takes care of the linear component of AFM/PM contribution. Here, S, defined as S=M_r/M_s, and M_s is the saturation magnetization. The fitted curve at 110 K is shown in the main panel of Fig. 4(b) as a representative. The extracted FM and AFM/PM contributions are shown in the insets (A) and (B) of Fig. 4(b), respectively. In Fig. 4(c) we have plotted the coercive field H_{cr} and remnant magnetization M_r deduced from the $M(H)$ loop as a function of temperature are plotted. Both show nonmonotonic temperature dependence. The nature of $H_{cr}(T)$ is like a typical canted antiferromagnet. M_r

shows a peak near T_{SR}. The nonmonotonic temperature dependence of H_{cr} is the manifestation of the interplay of the two sublattices.

Giant magnetocaloric effect in an exchange-frustrated $GdCrTiO_5$ antiferromagnet: Magnetocaloric properties of highly exchange frustrated AFM $GdCrTiO_5$ has been investigated. The competing magnetic exchange interaction of the Gd^{3+} and Cr^{3+} sublattices leads to the strong frustration. With the application of magnetic field, the ground state degeneracy is removed, as a result, a huge change in magnetic entropy ΔS_m occurs [20]. Fig. 5(a) shows the $M(T)$ curve for an applied field of 500 Oe. No LRO is observed down to 2 K. Above 150 K, χ follows the Curie-Weiss law. The calculated value of θ_{CW} is -24 K, indicating dominant AFM interaction. The deviation from the Curie-Weiss law occurs below 150 K, which is significantly higher than θ_{CW}. This indicates strong spin fluctuations in the PM state due to short range magnetic correlations. As a result of strong spin fluctuation, the long range magnetic ordering in this compound takes place at very low temperature (0.9 K). The frustration index is defined as θ_{CW}/T_N which is as high as $\simeq$ 30 for GCTO [21]. The inset (B) of Fig. 5(a) shows the $M(H)$ curve of GCTO up to 7 T in the temperature range 2-35 K. $M(H)$ looks like a Brillouin function of a paramagnet. At 2 K and 7 T, the moment is 7.4 μ_B/f.u which is about 6% higher than the spin only moment of Gd, indicating a small contribution from Cr sublattices. The field-induced magnetization indicates the large entropy change in GCTO. The magnetic entropy change has been calculated using the Maxwell's equation $\Delta S_m = \int_0^H (dM/dT)dH$. The calculated ΔS_m has been plotted in the main panel of Fig. 5(b) and the inset shows the ΔS_m vs H. The maximum value of ΔS_{max} reaches to 36 J/kg K for the field change 0-7 T which is significantly larger than that reported for several rare-earth based oxides

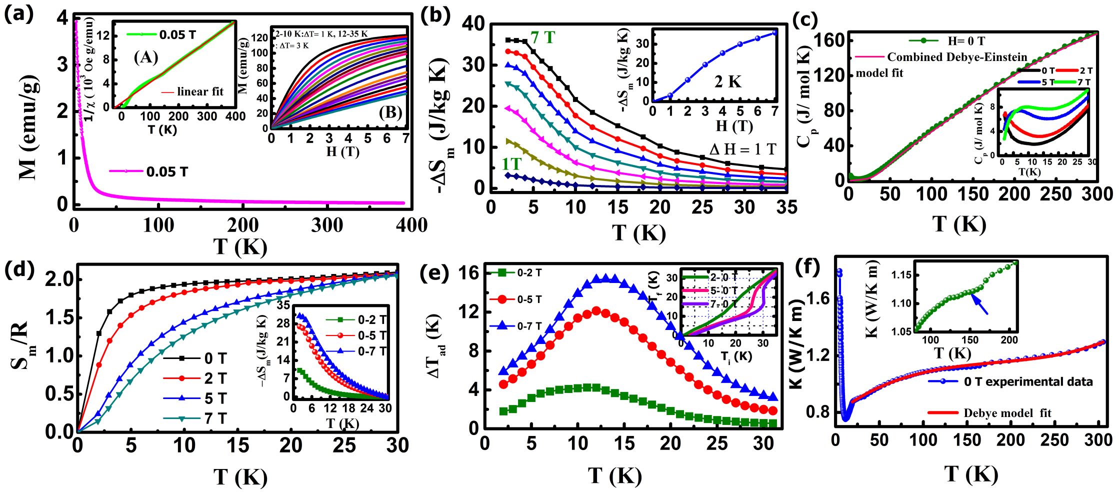

Figure 5: (a) The main panel shows $M(T)$ for 500 Oe and inset (A) shows the $(\chi^{-1})(T)$ and inset (B) shows the $M(H)$ for some selected T. (b) Main panel shows $\Delta \mathrm{S}_m(T)$ and inset shows $\Delta \mathrm{S}_{max}(H)$. (c) The main panel shows the zero-field heat capacity (C_P) for $\mathrm{GdCrTiO_5}$ compound and the solid line is the combined Debye-Einstein model fitting and inset shows $\mathrm{C}_P(H)$. (d) The main panel shows $\mathrm{S}_m/\mathrm{R}(H)$ and the inset shows the variation of ΔS_m calculated from the heat capacity data. (e) The main panel shows the temperature dependence of $\Delta T_\mathrm{ad}(H)$ for $\mathrm{GdCrTiO_5}$ and the inset shows final temperature T_f as a function of initial temperature T_i in the adiabatic demagnetization process. (f) The main panel shows the temperature dependence of thermal conductivity for $\mathrm{GdCrTiO_5}$ and the inset shows the Debye-fitting to the experimental data where the arrow indicates the anomaly near 150 K.

and intermetallic [22, 23]. The Fig. 5(c) shows the $C_P(T)$ curves at different fields. No anomaly has been observed down to 1.8 K due to LRO. After subtracting the lattice heat capacity, determined using combined Debye-Einstein model [24], the magnetic entropy S_m has been calculated by integrating C_m/T and plotted in Fig. 5(d). The estimated normalized entropy S_m/R is close to the theoretical value 2 for J=7/2. The inset of Fig. 5(d) shows that $\Delta \mathrm{S}_m$ determined using the $C_P(H, T)$ data is close to that calculated from the $M(H)$ curve. Fig. 5(e) shows the temperature variation another important parameter related to MCE, the adiabatic temperature change $\Delta \mathrm{T}_{ad}$. The maximum value of $\Delta \mathrm{T}_{ad}$ has been reached to 16 K

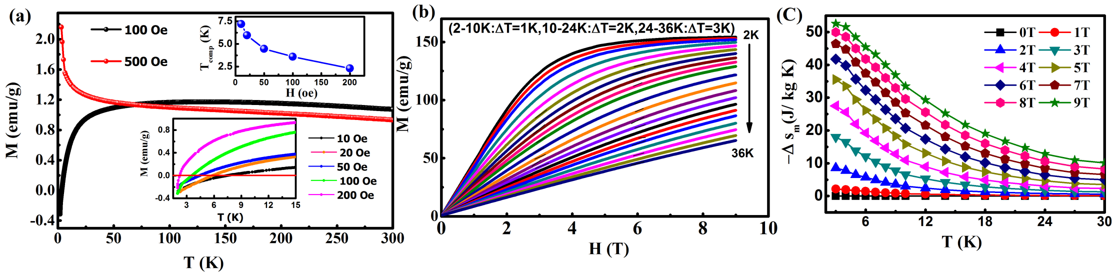

Figure 6: (a) Main panel shows $M(T)$ for 100 Oe and 500 Oe and lower inset shows $M(T)$ for different fields and upper inset shows $T_{comp}(H)$. (b) Shows the $M(H)$ for some selected T. (c) $\Delta S_m(T)$ for various fields for $GdFeO_3$ single crystal.

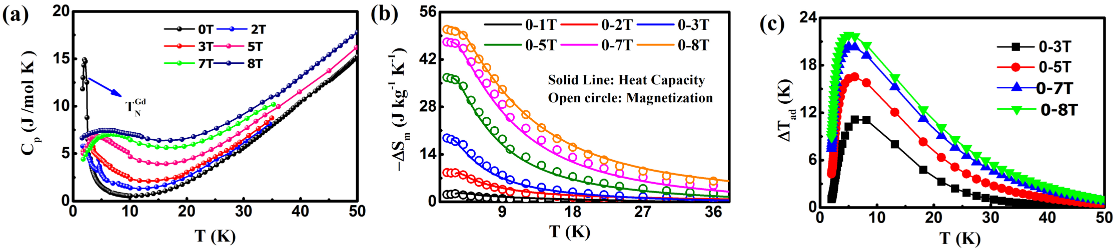

Figure 7: (a) shows the $C_P(T)$ for various applied fields and (b) shows the comparative ΔS_m extracted from $M(H)$ and $C_P(H)$ and (c) shows the $\Delta T_{ad}(T)$ for $GdFeO_3$ single crystal.

for 0-7 T field change and the inset shows the plot of final temperature (T_f) that can be reached by adiabatic demagnetization for different fields. Fig. 5(d) shows the thermal conductivity $\kappa(T)$ at low T. The value of κ reaches to 1.8 W/K which is reasonably good and comparable to several MCE materials [25].

Giant reversible magnetocaloric effect in a multiferroic $GdFeO_3$ single crystal: Magnetocaloric properties of the ortho-ferrite $GdFeO_3$ single crystal have been investigated in the temperature range 2-36 K by dc magnetization and heat capacity measurements. In this compound, Fe^{3+} moments order antiferromagnetically below 650 K along the c axis with a weak canted FM component along b axis due to the DM interaction and Gd^{3+} moments order at 2.5 K [26]. Fig. 6(a) shows $M(T)$ for two different fields 100 and 500 Oe. The anisotropic exchange or pseudo-dipolar interaction between the Gd and Fe moments produces an effective field at the Gd site which is antiparallel to the canted moment. Due to this competing interaction, the negative magnetization has been observed at low applied magnetic field below 200 Oe, as shown in the lower inset of Fig. 6(a). With application of magnetic field the compensation temperature T_{comp} shifts towards the lower T side and vanishes for $H > 500$ Oe, as shown in the upper inset of the Fig. 6(a). The field dependence of magnetization has been plotted in Fig. 6(b). At 2 K and 9 T, the value of magnetic moment is about 7.2 μ_B/Gd which is 3% higher than the spin only moment of Gd (7 μ_B/Gd). Using the $M(H)$ data, we have calculated the isothermal magnetic entropy change ΔS_m as shown in the Fig. 6(c). The value of ΔS_m is remarkably high, 52.5 J/kg K, at 2 K and 7 T. ΔS_m for $GdFeO_3$ is more than double the reported values of ΔS_m for other members of the ortho-ferrite series [27]. The temperature dependence of heat capacity $C_P(T)$ for different applied magnetic fields is shown in Fig. 7(a). The zero field C_P exhibits a prominent λ-like anomaly at around 2.5 K, indicating a paramagnetic-to-AFM transition of the Gd sublattice. With the application of field, the peak broadens due to the Schottky effect and shifts toward higher temperature. ΔS_m calculated from the heat capacity data is shown in Fig. 7(b) as a function of temperature. It is clear from the plots that the values of ΔS_m calculated from the magnetization and heat-capacity data are close to each other. Fig. 7(c) shows the adiabatic temperature change $\Delta T_{ad}(T)$ and the maximum value of the ΔT_{ad} has been reached as high as 22 K near 5 K, 8 T. Thus, both ΔS_m and ΔT_{ad} are very large in $GdFeO_3$ ortho-ferrite.

Unusual critical behavior in double perovskite Gd_2CoMnO_6: The Griffiths phase (GP) has been reported in some double perovskites such as Tb_2NiMnO_6,

Pr_2CoMnO_6, Ho_2NiMnO_6, etc., whereas Dy_2NiMnO_6 and Lu_2NiMnO_6 do not show GP-like behavior. The presence of "Griffiths-like" clustered phase in the above mentioned compounds has been claimed solely from the downturn behavior of χ^{-1} curve slightly above the T_C. However, this downturn in χ^{-1} is not sufficient to claim the formation of GP in the temperature region $T_C < T < T_{GP}$. The analysis of critical behavior is one of the important techniques to confirm the GP formation. In this work, we present the detailed analysis of critical behavior of ferromagnetic double perovskite Gd_2CoMnO_6 (GCMO). The critical behavior has been investigated by dc magnetization measurement. The compound shows a FM transition due to the superexchange interaction between the ordered Co^{2+} and Mn^{4+} ions near 123 K as shown in the main panel of Fig. 8(a). Besides this, $M(T)$ shows a broad downturn below 43 K due to the interplay of AFM interaction of Gd and Mn/Co sublattices. The anomaly at 43 K progressively suppresses and M shows a sharp increase due to the contribution of large PM moment of Gd^{3+} at low temperature for field above 1 kOe, as shown in the upper inset of Fig. 8(a). The lower inset of Fig. 8(a) shows the $M(H)$ curves at different temperatures below T_C. With increasing T, $M(H)$ curve shows saturation-like behavior as in the case of a typical ferromagnet. The transition temperature (T_C), determined from the $M(T)$ curve is also confirmed through heat capacity (C_p) data as shown in Fig. 8(b). The continuous change in magnetic entropy ($S_m(T)$) around T_C indicates that the transition is second-order in nature. The main panel of Fig. 8(c) presents the temperature dependence of inverse dc susceptibility, χ^{-1} ($=H/M$), for various applied fields which shows a downward deviation below 250 K. Often, this deviation has been attributed to the formation of the Griffiths phase. However, the deviation of inverse χ is not due to the onset of Griffiths phase. The expected nature of field

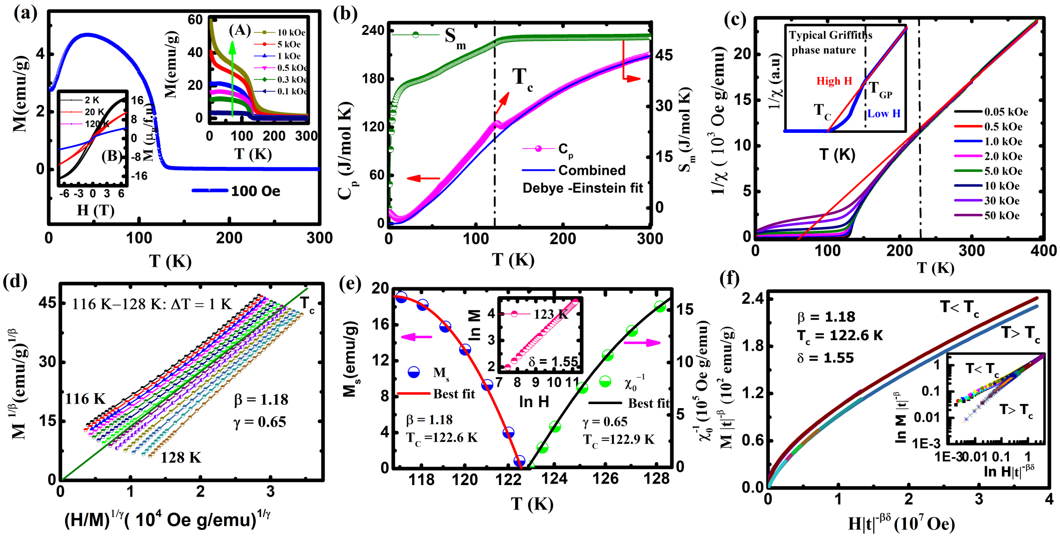

Figure 8: (a) The main panel shows the $M(T)$ at $H = 100$ Oe and inset (A) shows $M(T)$ curves for different H where the arrow indicates the direction of increase of magnetic field strength and the inset (B) displays $M(H)$ hysteresis loop for different temperatures. (b) $C_p(T)$ along with the combined Debye-Einstein model fit (solid line) and magnetic entropy (S_m) of GCMO. (c) The main panel shows the temperature dependence of inverse dc susceptibility ($\chi^{-1} = H/M$) of GCMO for different applied fields. The red line shows the linear fit to the Curie-Weiss law. The inset shows the expected nature of the Griffiths phase. (d) Modified Arrott plot $[M^{1/\beta}$ vs. $(H/M)^{1/\gamma}]$ using $\beta = 1.18$ and $\gamma = 0.65$. (e) The main panel shows the temperature dependence of spontaneous magnetization (M_S) and initial inverse susceptibility (χ_0^{-1}) and the lines represent the best-fit curve according to equation 1 and 2 where the inset shows log-log plot of $M(H)$ isotherm for 123 K. (f) Scaling plots below and above T_C and the inset shows the same plot in log-log scale.

dependence of χ^{-1} in the GP is shown in the inset of Fig. 8(c). In GP phase, χ^{-1} becomes linear at high fields, which does not happen even at 5 T for GCMO. Also, χ^{-1} should follow the power-law, $\chi^{-1}(T) = A(T - T_C^R)^{1-\lambda}$, where T_C^R is the critical temperature below which χ diverges and λ is an exponent such that $0< \lambda <1$ for $T_C < T < T_{GP}$ and λ=0 for $T > T_{GP}$ [28, 29]. We observe that GCMO does not follow this power-law expression and T_C^R=75 K is significantly smaller than T_C. The nature of magnetic phase transition in this double perovskite system has been analysed using the scaling theory. In the vicinity of a second-order transition, the diverging correlation length leads to the universal scaling laws for spontaneous magnetization (M_S), initial susceptibility (χ_0) and magnetization at T_C via a set of critical exponents β, γ and δ, which are defined as [30],

$$M_S(0,t) \sim (-t)^{\beta}, \qquad t < 0, \tag{1}$$

$$\chi_0{}^{-1}(0,t) \sim (t)^{\gamma}, \qquad t > 0, \tag{2}$$

$$M(H,0) \sim (H)^{1/\delta}, \qquad t = 0, \tag{3}$$

where t=$(T - T_C)/T_C$ is the reduced temperature. All the three exponents β, γ and δ are not independent of each other, rather they are related via Widom scaling relation, $\delta = 1 + \gamma/\beta$. To calculate the critical exponents and T_C, we use the modified Arrott plot (MAP) based on the Arrott-Noakes equation of state, $(H/M)^{1/\gamma} = a$t $+ bM^{1/\beta}$ where a and b are constants [31]. The MAP in Fig. 8(d) shows almost parallel straight lines in the high field regime. The convergence in the fitting is achieved for $\beta = 1.18$ and $\gamma = 0.65$. The obtained values of exponents are quite far from any conventional universality class. Here, we would like to mention that in several related double perovskite systems, magnetization is reported to follow conventional scaling behavior. La_2NiMnO_6 [31] and Y_2NiMnO_6 [32] obey scaling behavior belonging to 3D Heisenberg and 3D Ising class, respectively while the critical exponents for Pr_2CoMnO_6 [33] and Lu_2NiMnO_6 [34] are close to that for mean field one. From Fig. 8(d), it is clear that an isotherm between 122 and 123 K will pass through the origin, suggesting T_C is very close to 122.5 K. The intersections of these isotherms for T<T_C on $M^{1/\beta}$ axis and for T>T_C on $(H/M)^{1/\gamma}$ axis give the values of M_S and χ_0^{-1}, respectively. The temperature dependence of M_S and χ_0^{-1} are shown in Fig. 8(e). The power-law fitting to M_S and χ_0^{-1} according to the equation 1 and 2, respectively reveals $\beta = 1.18 \pm 0.06$ with $T_C = 122.6 \pm 0.2$ K and $\gamma = 0.65 \pm 0.01$ with $T_C = 122.9 \pm 0.3$ K. Another exponent δ has been determined from $M(H)$ curve at $T = 123$ K, the nearest one to the critical isotherm. The log-log plot of $M(H)$ curve at $T = 123$ K reveals δ=1.55±0.03 (see equation 3), which is shown in the inset of Fig. 8(e). With the obtained values of β, δ and T_C, we have plotted the scaling relation $M|t|^{-\beta}$ vs. $H|t|^{-\beta\delta}$, which is shown in Fig. 8(f). Depending on the sign of t, the magnetization data fall on two branches of the curve. This suggests that the critical exponents and T_C are reasonably accurate. Moreover, one can see that the Widom scaling relation is also satisfied. Indeed, the critical exponent δ is found to be unusually large in several colossal magnetoresistive compounds due to the presence of GP. On the contrary, the small value of δ in GCMO implies the non-Griffiths-like behavior of the clustered phase.

Nonlinear magnetodielectric properties of double perovskite Ho_2FeCoO_6: The magnetic and magneto-dielectric properties of double perovskite (DP) Ho_2FeCoO_6 have been explored. Fig. 9(a) shows the temperature dependence of magnetization at an applied field of 500 Oe. $M(T)$ shows clear anomalies at T_N^{Fe}=270 K and T_{SR}=45 K, due to antiferromagnetic transition and continuous reorientation of Fe^{3+} spins, respectively. At low temperature below 15 K, M increases sharply due to the dominating contribution from Ho^{3+} moments. The transitions at T_N^{Fe} and T_{SR} become broader with increasing magnetic field as shown in the inset (A) of Fig. 9(a). Above 270 K, the inverse susceptibility χ^{-1} has been fitted with the Curie-Weiss law as shown in inset (B) of Fig. 9(a). Fig. 9(b) shows the temperature dependence of real part of dielectric constant $\epsilon\prime$ at a frequency f=1

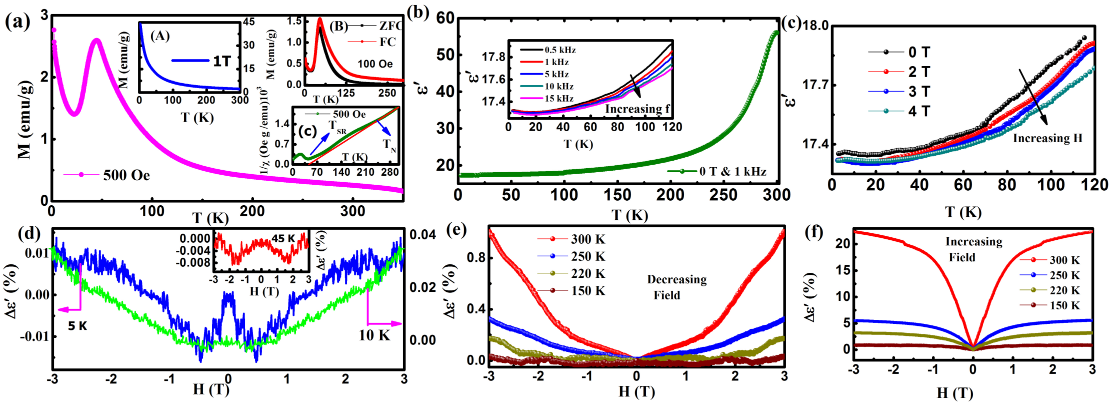

Figure 9: (a) The main panel shows the $M(T)$ for 500 Oe where inset (A) shows the $M(T)$ for 1 T and (B) shows the $\chi^{-1}(T)$ for 500 Oe. (b) The main panel shows the $\epsilon(T)$ for 0 T and 1 kHz and inset shows the frequency variation of ϵ. (c) The field dependency of ϵ. (d) The main panel shows the variation of $\Delta\epsilon$ (H) for some representative temperatures and inset shows for 45 K. (e) The $\Delta\epsilon$ (H) at high temperature in decreasing fields. (f) The $\Delta\epsilon$ (H) at high temperature in increasing fields.

kHz. The dielectric properties that arise from the dipolar relaxation as a result of asymmetric hopping of charge carriers under the applied electric field is shown in Fig. 9(b) for $T\leq120$ K. At low temperature, the dielectric constant is temperature and frequency independent, as shown in the inset of Fig. 9(b), which indicates the intrinsic nature of dielectric properties. The strong frequency dependency and large variation of $\epsilon\prime$ with T, for $T\geq120$ K denote the extrinsic polarization due to the Maxwell-Wagner effect [35]. The systematic variation of the $\epsilon\prime$ with magnetic field below 120 K has been shown in the Fig. 9(c). The magnetodielectric effect is defined as MD [$\Delta\epsilon\prime$(H)/$\epsilon\prime$(0)] % = [($\epsilon\prime$(H) - $\epsilon\prime$(0))/$\epsilon\prime$(0)]%, where $\epsilon\prime$(H) and $\epsilon\prime$(0) are the dielectric constant under applied and zero magnetic field, respectively. The main panel of Fig. 9(d) demonstrates the magnetic field variation of dielectric constant $\Delta\epsilon\prime$(H) at 5 and 10 K. Above 10 K, i.e., far from the AFM ordering of Ho^{3+} moments, the magnetodielctric effect suppresses and completely disappears above T_{SR} (=45 K), suggesting that the magnetic ordering of Ho^{3+} ions and the dielectric properties of the materials are interconnected. The nonlinear variation of the $\epsilon\prime$ has been observed in the temperature range 10 K $< T <$ 45 K due to the Ho^{3+} and Fe^{3+} interaction. At high temperatures above 150 K, $\Delta\epsilon\prime$ starts to develop again and a large hysteresis has been observed between the cooling and heating cycles which is shown in the Fig. 9(e) and Fig. 9(f) respectively. The much enhanced MD even above T_N^{Ho} originates from the extrinsic effect accompanied by the increase of dielectric loss which is influenced by grain boundaries or material-electrode interfaces.

Bibliography

[1] K. A. Gschneidner Jr. *et al.*, Rep. Prog. Phys. **68**, 1479 (2005).

[2] S. J. Yuan *et al.*, Phys. Rev. B **87**, 184405 (2013).

[3] L. D. Stevens *et al.*, Journal of Research and Development **25**, 5, (1981).

[4] A. Hoffman *et al.*, Phys. Rev. Appl. **4**, 047001 (2015).

[5] X. Liu *et al.*, Phys. Rev. B **62**, 15112 (2000).

[6] J. Hwang *et al.*, Phys. Rev. B **85**, 024415 (2012).

[7] H. J. Zhao *et al.*, Nature. Com. **5**, 4021 (2014).

[8] I. Dzyaloshinskii *et al.*, J. Phys. Chem. Solids **4**, 241, (1958).

[9] D. Jeffrey *et al.*, Chem. Sci. **2**, 2078, (2011).

[10] M. E. Zhitomirsky, Phys. Rev. B **67**, 104421 (2003).

[11] M. Das *et al.*, J. Phys.: Condens. Matter **32**, 035802 (2020).

[12] M. Das *et al.*, Phys. Rev. B **98**, 104420 (2018).

[13] M. Das *et al.*, Phys. Rev. B **96**, 174405 (2017).

[14] M. Das *et al.*, Phys. Rev. B **101**, 144433 (2020).

[15] M. Das *et al.*, Physica B **571**, 32-35 (2019).

[16] G. R. Blake *et al.*, Phys. Rev. B **71**, 214402 (2005).

[17] Y. S. Vishnyakov *et al.*, J. Exp. Theor. Phys. **30**, 1059–61 (1970).

[18] R. S. Fishman *et al.*, Phys. Rev. B **70**, 140402 (2004).

[19] V. Singh *et al.*, Phys. Rev. B **82** 054417 (2010).

[20] S. Pakhira *et al.*, Phys. Rev. B **94**, 104414 (2016).

[21] T. Katsufuji *et al.*, Phys. Rev. B **64**, 104419 (2001).

[22] A. Rostamnejadi *et al.*, J. Magn. Magn. Mater. **323**, 2214 (2011).

[23] L. Li *et al.*, Appl. Phys. Lett. **100**, 152403 (2012).

[24] E. Gamsjager *et al.*, Monatsh Chem. **149**, 357–368 (2018).

[25] X. M. Wang *et al.*, Phys. Rev. B **82**, 094405 (2010).

[26] J. D. Cashion *et al.*, J. Phys. C: Solid State Phys. **3**, 1612 (1970).

[27] Y. J. Ke *et al.*, Sci. Rep. **6**, 19775 (2016).

[28] W. Jiang *et al.*, Phys. Rev. B **77**, 064424 (2008).

[29] D. Bhoi *et al.*, J. Phys. Chem. C **117**, 16658 (2013).

[30] N. Khan *et al.*, Phys. Rev. B **82**, 064422 (2010).

[31] X. Luo *et al.*, J.Phys.: Condens. Matter **20**, 465211 (2008).

[32] H. Nhalil *et al.*, AIP Conf. Proc. **1728** 020184 (2016).

[33] L. Zhang *et al.*, J. Alloys Compd. **763**, 613 (2018).

[34] I. N. Bhattia *et al.*, Phys. B: Condens. Matter **558**, 59 (2019).

[35] S. H. Oh *et al.*, J. Phys. D: Appl. Phys. **48**, 445001 (2015).

List of Figures

List of Tables

1

Introduction

1.1 General background

Oxides contain the most abundant chemical element "Oxygen", on our planet. Among the various kinds of magnetic oxides, the rare-earth(R) transition metal based ones are more enthralling for their fascinating properties, which are important from fundamental point of view as well as for technological applications in our modern life. In the last few decades, manganites ($R\mathrm{MnO}_3$) and cobaltites ($R\mathrm{CoO}_3$) have been extensively investigated for their rich phase diagram and colossal magnetoresistive properties. The next-generation device technology is in a search for novel magnetic materials with outstanding functionality such as spin switching, magnetization (M) reversal (negative magnetization), spin reorientation, large magnetocaloric effect and multiferrocity. These materials have received considerable attention due to their potential for several technological applications such as in ultra-fast photomagnetic recording, laser-induced ultrafast spin reorientation, ambient multiferroics, non-thermal spin dynamics, inertia-driven spin switching and magnetic refrigeration. In particular, the spin dynamics in canted antiferromagnets, with multiple exchange interactions, is approximately two orders of magnitude faster than that in simple metallic or insulating ferromagnets. The most important characteristic of this type of system is the presence of both ferromagnetic (FM) and antiferromagnetic (AFM) interactions in a single compound. Moreover, novel and exotic physics is expected to emerge when more than one type of spin sublattice participates in magnetism. Undoubtedly, these materials are quite promising for future device applications. So far, the families of ferrimagnets, rare-earth garnets and orthovanadates are the well known examples where the magnetization reversal (MR) and spin switching have been discovered, whereas the rare-earth ortho-ferrites and orthochromites are famous for their spin reorientation transition. Large magnetocaloric effect for exchange frustrated system is also a trending topic now, rather than the geometrical frustrated spin lattices such as pyrocholre lattice, spin ice etc.

In the last few decades, the critical analysis of the perovskite manganites and cobalites have been investigated. But the debate on the critical scaling analysis on the double perovskite still persists and the presence of Griffiths cluster is also a interesting topic in these kinds of materials. The double perovoskites are also now in the front row of the new-fashioned class of materials owing to their magnetodielectric effect near room temperature. The magnetic properties of the materials investigated are governed by the Dzyaloshinskii-Moriya (DM) exchange interaction, single-ion anisotropy and frustration. On the basis of the above-mentioned aspect of physics in magnetism, interesting properties such as magnetocaloric effect, critical behaviour and magnetodielectric effect of some lesser studied rare-earth transition metal oxides are investigated. We briefly discuss the Dzyaloshinskii-Moriya exchange interaction and canted antiferromagnetism in the next section of this chapter. Then the role of single-ion anisotropy to the magnetic properties is introduced. In the following section the role of magnetic frustration is discussed. A brief history of the magnetocaloric materials, their underlying working principles and potential applications are reviewed in the section that follows. In the next section the magnetic phase transition and critical behaviour of double perovskites are discussed. Subsequent section a brief discussion on the magnetodielectric properties of the oxides are given. Finally, the major findings of this thesis are summarized.

1.2 Dzyaloshinskii-Moriya (DM) exchange interaction and canted antiferromagnetism

The exchange interaction is a quantum mechanical effect that occurs between identical or indistinguishable particles, and very crucial parameter for magnetization. The exchange interaction may be symmetric or antisymmetric depending on the sign of the wave function, upon the application of the exchange symmetry or symmetry operator. The Hamiltonian of the symmetric Heisenberg exchange interaction can be expressed as $H= -J(S_i\ S_j)$ which contains the dot product of the two spins S_i and S_j. J is the exchange operator [1]. This is positive for AFM and negative for FM case. The energy is lowest if they have a collinear orientation (parallel for ferromagnetic case, antiparallel for the antiferromagnetic case with the negative sign of J). Any deviation from the parallel (antiparallel, respectively) configuration is associated with an energy penalty. The Heisenberg exchange interaction is symmetric as suppose the S_i is fixed, and S_j has an angle with S_i,

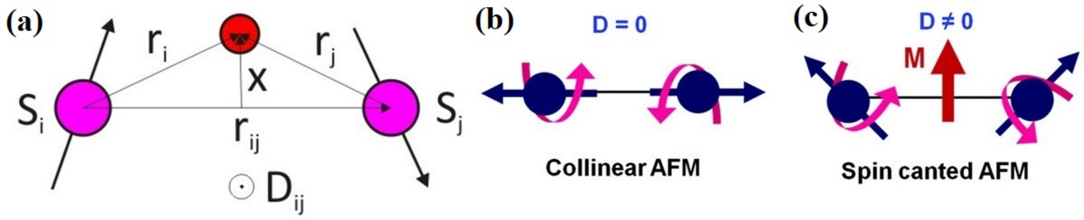

Figure 1.1: (a) The pictorial representation of Dzyaloshinskii-Moriya interaction and spin orientation for the (b) collinear magnet and (c) non collinear magnet.

as the same energy penalty occurs, regardless the deviation from collinearity from either side.

For the Dzyaloshinskii-Moriya interaction (DMI) [2, 3, 4], the Hamiltonian can be written as H=-$D[S_i \times S_j]$ and contains the cross product $S_i \times S_j$ which is a vector perpendicular to S_i and S_j, times the DM vector D as shown in Figure 1.1(a). This means that energy can be gained by introducing an angle between S_i and S_j. However, the deviation from collinearity has to be in the right direction as the opposite direction is energetically costly. Thus spin rotation is favored for one particular sense. Hence, DMI is an asymmetric interaction. The DMI favours the spins for perpendicular alignment. In general DMI is weak because it is just a relativistic correction as proposed by I. Dzyaloshinskii in 1960 [3]. Later Moriya proved it on the basis of spin orbit coupling [2]. Similar to spin orbit coupling in the systems where the DM interaction is involved, the interaction between the magnetic ions is recognized as pseudo dipolar interaction. Nevertheless, this interaction is crucial for weak ferromagnetic phenomenon where spins are canted by small amounts and was observed first in case of α-$\mathrm{Fe}_2\mathrm{O}_3$. The presence of DM interaction explained its ferrimagnetic behaviour [5, 6, 7, 8]. In the case of AFM with DM interaction, application of a sufficiently strong magnetic field along the easy axis of magnetization was expected to overturn the sublattice magnetization vectors, giving rise to field induced spin reorientation or spin flop transition. Thus for collinear AFM, the DM vector is zero and and for canted AFM, it is non-zero as shown in Figures 1.1 (b) and (c). This interaction is also very crucial for multiferroic material that has been studied intensively in last few decades [9]. In case of multiferroic materials, a small lattice distortion causes symmetry breaking that generates the DM interaction and that is known as inverse DM interaction [9]. In case of a metallic system, the DM interaction can be understood as an anisotropic exchange (or RKKY) interaction [10, 11]. It vanishes in case the system is centrosymmetric [9]. In this dissertation, we will also see the beauty of the DMI for generating weak ferromagnetism in an antiferromagnetic network. In the case of orthorhombic $R\mathrm{FeO}_3$ and $R\mathrm{CrTiO}_5$, the small octahedral distortion along with the DM interaction cause weak canted ferromagnetism in these systems and thereby various interesting magnetic properties have been observed.

1.3 Single-ion anisotropy

Magnetic anisotropy is a crystallographic direction dependent magnetic property of a material. In absence of external magnetic field, the magnetically isotropic material has no preferential direction for alignment of its magnetic moments. Whereas for the anisotropic magnetic materials, the moments prefer to orient in a particular direction of the crystal axis, which is known as the easy axis of the magnetization. Thus the easy axis is the energetically favorable direction of the spontaneous magnetization. There are several kinds of anisotropy such as crystalline anisotropy [12], shape anisotropy [13] and stress anisotropy [14] etc. However, the crystalline anisotropy is an intrinsic property of the magnetic materials. Magnetocrystalline anisotropy is discussed only here. "Magnetocrystalline anisotropy" refers to the such type of anisotropy that depends on the crystalline symmetry of the materials.

1.3.1 Anisotropy in Cubic crystal

For face centred cubic (FCC) crystal like iron, the magnetization shows a strong anisotropy as depicted in Figure 1.2. The $M(H)$ curves show that along one direction ($< 111 >$), saturation can be achieved with low field, which is called the "easy axis" of magnetization. The direction ($< 100 >$) along which the magnetization saturates at higher fields, as compared to that for the easy axis, is called the "hard axis" of magnetization. The applied magnetic field works against the anisotropic force which tends to turn the magnetization vector away from the easy direction. Therefore, there is a energy stored in the crystal, known as crystal anisotropy energy (E). The anisotropy energy can be expressed in terms of a series expansion of the direction cosines of saturation magnetization (M_s) relative to the crystal axes. In a cubic crystal, if M_s makes α_1, α_2, α_3 angles with the crystal axes then cosines of these angles are called direction cosines [12]. Then

$$E = K_0 + K_1(\alpha_1^2\alpha_2^2 + \alpha_2^2\alpha_3^2 + \alpha_3^2\alpha_2^2) + K_2(\alpha_1^2\alpha_2^2) + ... \tag{1.1}$$

where K_0, K_1, K_2. . . are constants for a given material at a particular temperature. Generally, the higher powers of K are dropped, and sometimes K_2 is so small that K_2 can be neglected. The first term, K_0, is usually ignored as it is independent of angle and we are interested only in the change in the energy when the M_s vector rotates from one direction to another. When K_2 is zero, the direction of easy magnetization is determined by the sign of K_1. If K_1 is positive, then E_{100}

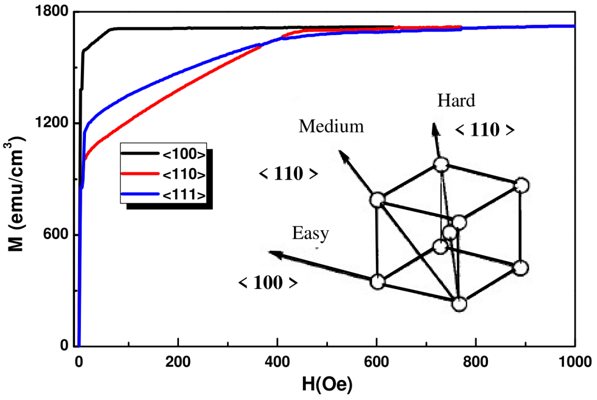

Figure 1.2: Anisotropy for the cubic crystal.

$< E_{110} < E_{111}$, and <100> is the easy direction, because E is a minimum when M_s is in that direction. Thus for iron and the cubic ferrites containing cobalt have positive values of K_1. If K_1 is negative, $E_{111} < E_{110} < E_{100}$, and <111> is the easy direction. K_1 is negative for nickel and for all the cubic ferrites that contain little or no cobalt. When K_2 is not zero, the easy direction depends on the values of both K_1 and K_2.

1.3.2 Anisotropy in Hexagonal crystal

For the hexagonal crystal structure like cobalt, c-axis is the direction of easy axis of magnetization and all directions in the basal plane are found to be equally hard for magnetization as shown in Figure 1.3 [15, 16]. Under these conditions, the anisotropy energy E depends on only a single angle θ, where θ is the angle between the M_s vector and the c-axis, and the anisotropy can be described as

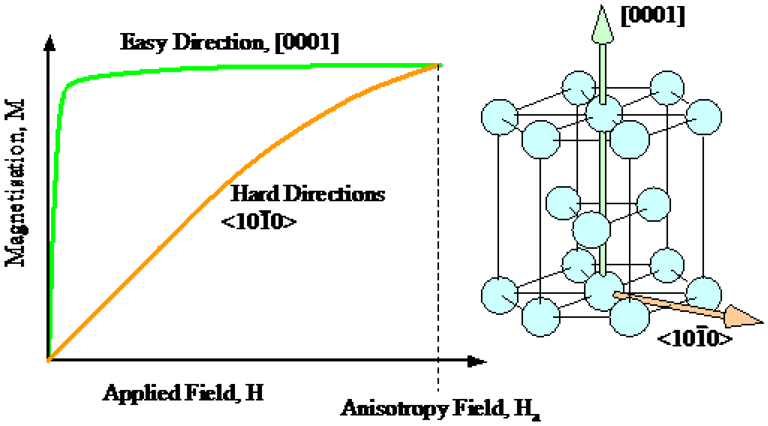

Figure 1.3: Anisotropy for the hexagonal crystal.

uniaxial in this case [17]. Therefore,

$$E = K_0 + K_1 \sin^2\theta + K_2 \sin^4\theta + ... \tag{1.2}$$

For the positive values of K_1 and K_2, the energy E is minimum when θ=0, and the c-axis is the easy axis of magnetization. A crystal with a single easy axis, along which the magnetization can point either up or down, is referred to as a uniaxial crystal. It forms a simple domain structure in the demagnetized state. Elemental cobalt and many rare-earth transitional metal based intermetallic compounds are the examples for uniaxial crystals. If K_1 and K_2 are negative, the minimum value of E occurs for θ=90. This creates an easy plane of magnetization, which is the basal plane of a hexagonal material, lying perpendicular to the c-axis. For the opposite signs of K_1 and K_2, the situation can be very complicated.

1.3.3 Physical origin of the crystalline anisotropy

The crystalline anisotropy mainly arises from the spin orbit interaction of a material [18]. Crystalline anisotropy is determined by the interaction of the orbital state of the magnetic ions with the surrounding crystalline field which is very strong for the anisotropic materials. The spin of the electron interacts with the crystal structure via spin-orbit coupling. Due to the spin orbit coupling, different orientations of the electron spin gives rise to different orientations of the atomic orbital relative to the crystal structure. The anisotropy is more in the rare-earth element (4f electron) with high values of the magnetic moments, as compared to the transition metal elements (3d electron). In Chapter 3 of this thesis, we discuss how the strong anisotropy of the rare-earth elements Dy ($J = 15/2$) and Ho ($J = 8$) determines the magnetic properties in RCTO compounds. Whereas the Gd ($J = 7/2$) based ortho-ferrite shows isotropic magnetic properties making it different from others ferrites as discussed in the Chapter 5.

1.4 Frustration

In condensed matter physics, magnetic frustration is a very interesting phenomenon where due to either the non-trivial atomic positions in a regular lattice or the unequal magnetic interactions in a complex magnetic structure causes conflicting interatomic forces, as a result of which a large number of magnetic ground states have been observed. When the frustration of spins arises due to the lattice geometry, it is known as "geometrical frustration" and when it arises due to different magnetic interaction it is known as "exchange frustration".

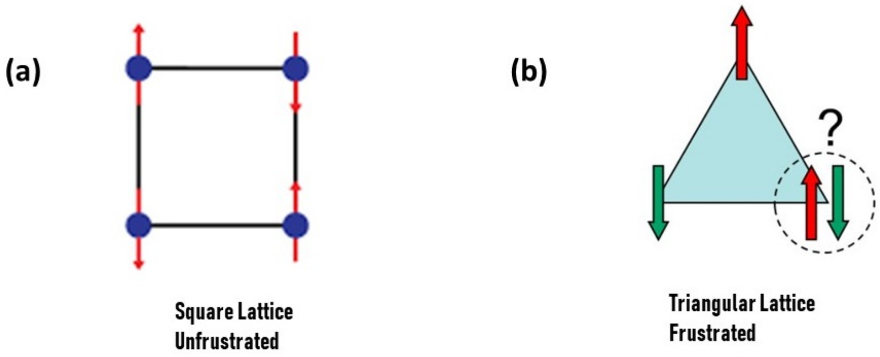

Figure 1.4: (a) Unfrustrated square lattice and (b) frustrated triangular lattice.

1.4.1 Geometrical frustration

In 1950, the geometrical frustration in a spin structure was first investigated by G. H. Wanneier [19]. He studied the triangular lattice with AFM nearest neighbour interactions upon considering the Ising model. Later on, extensive studies on the geometrical frustration for spin glass systems have been conducted by G. Toulouse and J. Vannimenus in 1977 [20, 21]. In a spin system, where both the FM and AFM magnetic interactions are present, the type of the dominating interaction depends on the separation of the spins. Square lattice has no geometrical frustration wherein the ground state of the lattice shows only one spin configuration as shown in Figure 1.4(a). The geometrical frustration has been observed in the triangular lattice [22], pyrochlore lattice [23], honeycomb lattice [24], Kagomoe lattice [25] and garnets [26] where the triangle network of the spins exist. The triangular arrangements, of the spins in these lattices show more than one ground states as shown in Figure 1.4(b). Geometrical frustration plays important role in magnetism which leads to various spin states such as spin glass, spin liquid, spin ice etc. The geometrical frustration can be well demonstrated in the triangular lattice as depicted in Figure 1.5. Now we consider three spins arranged at the corners of

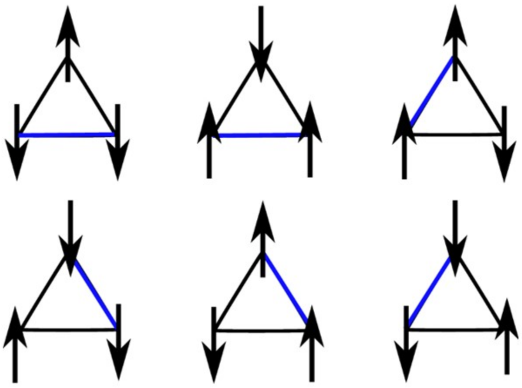

Figure 1.5: Multiple ground states for a frustrated triangular lattice.

a triangular lattice with antiferromagnetic interactions between them. The spins are constrained to point either up or down, and the energy of interaction between any two spins is minimized if the two spins are in opposite directions. Therefore, only two out of the three spins can align anti-parallel, while the interaction of the third remains frustrated as the third spin cannot decide which of the other two neighbouring spins to align anti-parallel with. Since this effect occurs for each spin, the ground state is six fold degenerate. Therefore, the interplay between geometric frustration and spin ordering leads to multiple degeneracy of the ground states.

1.4.2 Exchange frustration

Although the geometrical frustration has been well studied in the last few decades, scientists are now showing interest in an another type of frustration, that is known as exchange frustration [27, 28, 29]. This type of frustration arises due to the bond-dependent anisotropic exchange interactions or competing magnetic exchange interactions in a complex magnetic system. The anisotropic exchange interaction, in general, occurs due the DM interaction as has been discussed in the section 1.2. For the exchange frustrated materials, the DM interaction occurs due to the spin orbit coupling with a broken structural inversion symmetry. The spins show the canted FM in the AFM network due to the DM interaction, as a result of which the spin gets frustrated due to this competing exchange interactions. When the ratio of the two lattice parameters (say c/a) approaches 1 ($\simeq 1$) then also one expects strong frustration. Moreover, when the nearest neighbour exchange interaction and the next nearest neighbour exchange interaction are of opposite signs the system gets frustrated. Bond dependent symmetric and antisymmetric exchange interactions lead to frustration in La_2CuO_4 and as a result multiple ground states occur [30]. As a result of this exchange frustration, the long range AFM ordering gets suppressed and ordering temperature becomes very low, sometimes reaching to sub kelvin temperature. With the application of an external magnetic field, the ground state degeneracy breaks and a large magnetic entropy is released. This entropy change can be used in the magnetic refrigeration technology as we have discussed at length in Chapter 4 for exchange frustrated $GdCrTiO_5$ compound.

1.5 Magnetic refrigeration

1.5.1 History and general background

"Magnetocaloric effect", as the name suggests, is a magneto-thermodynamic phenomenon in which the change in temperature of a magnetic material is caused by an external magnetic field. Thus, magnetocaloric effect (MCE) can be used as a tool in cooling or refrigeration purpose. Nowadays, the refrigeration technology is very useful over a broad range of temperatures ranging from room temperature to ultra low temperature. The room temperature refrigerants are used in domestic and industrial applications like in air conditioner. Whereas the low temperature refrigerants are used in versatile fields like food and medicine storage in supermarket and also for industrial uses like liquefaction of different kinds of gases, superconducting coils, in medical and space sciences and also in research lab to study different physical properties down to very low temperature. These magnetic refrigerants are superior over the conventional gas compressor refrigerants in various aspects. The conventional refrigerants eject harmful ozone depleting green house gas like chlorofluro carbon (CFC) whereas the magnetic refrigerant does not eject such kind of life-threatening gases. Besides, the magnetic refrigerants are more efficient than the conventional ones. The MCE based materials are also more compact. The two basic parameters of MCE, are the isothermal magnetic entropy change (ΔS_m) and adiabatic temperature change (ΔT_{ad}) which should be very large. Besides these, magnetic cooling/heating capacity (MC) is an another parameter which determines the amount of heat transfer between hot and cold reservoirs in an ideal refrigeration cycle should be also large enough.

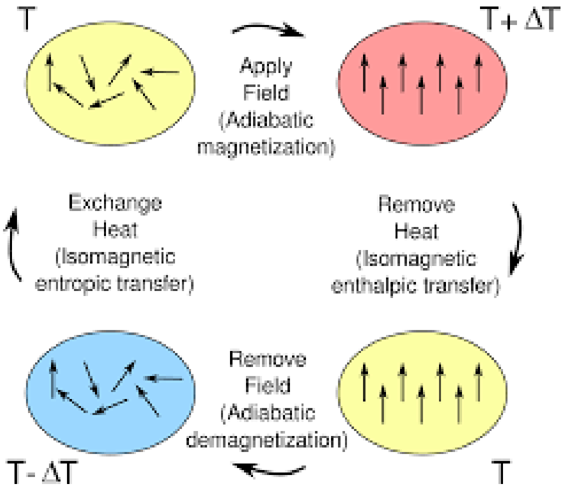

Figure 1.6: Pictorial representation of the outline of a magnetic refrigeration cycle.

1.5.2 Outline of magnetocaloric effect

As the MCE is based on the field response of the magnetic materials, we have to know the behaviour of the magnetic materials under the influence of a magnetic field before it can be used in magnetic refrigeration technology. Any magnetic material contains two types of internal excitation energy, the phonon excitation which is related to the lattice degree of freedom and magnetic excitation which is related to the spin degree of freedom. For an isolated system, total entropy (S) of the magnetic material is fixed and it consists of two parts, lattice and magnetic entropy, i.e., S_L and S_M respectively and $S= S_L + S_M$. The schematic representation of a typical magnetic refrigeration has been depicted in Figure 1.6.

Adiabatic magnetization: When the external magnetic field is not applied on the magnetic material, the spins are in random orientation with initial temperature T. When the field H is applied on the material, the magnetic moments get aligned along the magnetic field direction. So the magnetic entropy will decrease and at the same time to keep the total entropy of the system constant, the lattice entropy increases. As a result, the temperature of the material becomes $T + \Delta T$. This procedure is known as adiabatic magnetization as the magnetic field has been applied in an adiabatic condition.

Isomagnetic enthalpic transfer: In the second step, the increased temperature ΔT is removed by some coolant liquid like helium or cold water. So the temperature becomes T again. The field has been kept fixed in this step, thus the procedure is known as isomagnetic enthalpic transfer.

Adiabatic demagnetization: Then in the third step, the external field is removed and in this adiabatic demagnetization process, the magnetic moments again become random and as a result, the magnetic entropy gets increase and at the same time the lattice entropy decreases. The temperature of the material will decrease and becomes T - ΔT.

Isomagnetic entropic transfer: In the final step, a hot material has been connected with the MCE material which needs to be cooled. So the temperature of the hot material has been reduced by the amount ΔT by the refrigerant material. In this procedure the magnetic field is kept constant to avoid reabsorbing the heat so this is also a isomagnetic procedure.

1.5.3 Suitability of the magnetic refrigerant material

Whether the MCE materials have been used in the low temperature or room temperature region, the main concern with the magnetic refrigerants should have large magnetocaloric effect, large MCE over a wide temperature range. Second order phase transition of the material near the operating temperature is desired as less hysteresis loss can be observed as compared to the first order transition. Moreover, the material under study should has insulating properties as the eddy current loss is very high in the refrigeration cycle for the metallic compound. The thermal conductivity of the refrigerant should be large for fast heat response.

1.5.4 Thermodynamics of the magnetocaloric effect

Since entropy is a state function, the total differential can be expressed as:

$$dS = \left(\frac{\partial S}{\partial T}\right)_{p,H} dT + \left(\frac{\partial S}{\partial P}\right)_{T,H} dP + \left(\frac{\partial S}{\partial H}\right)_{p,T} dH \tag{1.3}$$

For isobaric (dp=0) and isothermal (dT=0) conditions the entropy change depends only on the magnetic field. From the Maxwell thermodynamic relation, the entropy change of a magnetic material under the application of a magnetic field H is related to M with respect to T through

$$\left(\frac{\partial S}{\partial H}\right)_{T} = \left(\frac{\partial M}{\partial T}\right)_{H} \tag{1.4}$$

Therefore, after integrating the magnetic entropy change, $\Delta S_M(T,H)$, for isobaric and isothermal conditions is equal to

$$\Delta S_M(T,H) = S_M(T,H) - S_M(T,0) = \int_0^H \left(\frac{\partial M}{\partial T}\right)_{H} dH \tag{1.5}$$

Since the magnetic entropy change $\Delta S_M(T,H)$ is proportional to the derivative of magnetization with respect to temperature at constant field.

Now from equation 1.3, for reversible adiabatic-isobaric process, the infinitesimal adiabatic temperature rise is equal to

$$\Delta T_{ad}(T,H) = \int_0^H \frac{T}{C_p(T,H)} \left(\frac{\partial M}{\partial T}\right)_H dH \tag{1.6}$$

Therefore, the adiabatic temperature rise is directly proportional to the absolute temperature, to the derivative of magnetization with respect to temperature at constant field and to the magnetic field change; and it is inversely proportional to the heat capacity.

Eq.1.3 and 1.6 have fundamental importance for understanding the behavior of MCE in solids, and serve as a guide for the search of new materials with a large magnetocaloric effect. For a constant magnetic field, the magnetization for paramagnets and simple ferromagnets decreases with increasing temperature [i.e. $\left(\frac{\partial M}{\partial T}\right)_H<0$], then $\Delta S_M(T,H)$ is negative and $\Delta T_{ad}(T,H)$ is positive. For a ferromagnetic material $\left(\frac{\partial M}{\partial T}\right)_H$ is maximum at T_c therefore, $\Delta S_M(T,H)$ should show a maximum at T_c. However, it is not straightforward from Eq. 1.6, because the heat capacity at constant field is also anomalous near the T_c and it has been shown that $\Delta T_{ad}(T,H)$ in ferromagnets show peaks at the Curie temperature when $H \to 0$. $\Delta T_{ad}(T,H)$ and $\Delta S_M(T,H)$ show similar behavior, both gradually decreasing below and above the T_c. For the same value of $\Delta S_M(T,H)$, $\Delta T_{ad}(T,H)$ is larger at a higher absolute temperature, and also when the total heat capacity of the solid is lower.

In the case of high temperature and low field limit, the magnetic entropy of the paramagnet can be expressed as:

$$S_M(T,H) = Nk_B[ln(2J+1) - \frac{J+1}{3J}x^2] \tag{1.7}$$

Magnetic entropy for a completely disordered state reaches at maximum value, which may be realized for the conditions $T \rightarrow \infty$ and $B = 0$. The maximum magnetic entropy is given by:

$$S_M^{max} = Nk_B ln(2J+1) \tag{1.8}$$

So the maximum change of entropy for one mole of magnetic atoms is:

$$\Delta S_M^{max} = N_A k_B ln(2J+1) \tag{1.9}$$

where N_A is the Avogadro number.

1.6 Magnetic phase transition and critical phenomena

Phase transitions are brought about by cooperative interactions between spins, charges, and excitations. A change in the order parameter which defines a phase transition, can be done by thermodynamic parameters such as temperature, pressure, or magnetic field. A universality class (based on the dimensionality of the lattice and the order parameter) is assigned to a system depending on the values of the asymptotic critical exponents that characterizes the phase transition. Universal classes based on theoretical spin-spin interaction models (like the Heisenberg, mean field or the Ising) have been extremely useful in trying to discover the intriguing magnetic transitions in real systems. These critical exponents that define a particular universality class are mentioned in the Table 1.1.

Critical magnetic behavior has a close association with the magnetic phase tran-

Table 1.1: Theoretical values of critical exponents of different models

Models	β	γ	δ
Mean field	0.5	1.0	3.0
3D-Heisenberg	0.365	1.386	4.8
3D-Ising	0.325	1.24	4.82
Tricritical-mean-field	0.25	1.0	5.0
3D-XY	0.346	1.316	4.81

sition. Thus, one possible way to understand a complex magnetic transition is to analyze the critical exponents. The values of the exponents help to probe the interaction mechanism around the Curie temperature of a system. The details literature survey on the experimental and as well as theoretical analysis has concluded some general features of the inherent magnetic interaction and the belonging of the universal class of the different types of materials. The critical exponents for the single-crystalline uniform FM compounds, are found to be the 3D Heisenberg class with nearest-neighbor interaction as in case of $La_{0.67}Sr_{0.33}CoO_3$ single crystal [31]. The deviation of the 3D Heisenberg model to the Ising model may results from the presence of magnetocrystalline anisotropy of a complex magnetic system like $R_{0.6}Sr_{0.4}MnO_3$ (R = Pr, Nd) [32]. The presence of both extrinsic as well as intrinsic inhomogeneities above and below T_C may indicate new scaling relation for Griffiths singularities with high value of β such as $La_{0.7}Ca_{0.3}MnO_3$ [33]. In presence of short-range FM cluster above T_C leads the system in mean field class for polycrystalline compound as in case of $La_{0.8}Sr_{0.2}MnO_3$ [34]. When the complex multiple interactions competes with each other, the critical exponents deviate from these well known universality classes and the values of the exponents fall in between the two classes.

1.6.1 Critical phenomena in double perovskites

The double perovskite, $A_2BB'O_6$ types of material, which can host two different transition metal cations at the B-sites of its perovskite (ABO_3) derived structure that provide the possibility to explore the interplay of localized 3d transition metals. This interplay gives rise to extraordinary magnetic properties. So far, about a thousand of double perovskite compounds have been synthesized, with A site being occupied by divalent cations like Sr, Ca or Ba (some rare cases of Pb or Cd) and trivalent cations like La-group of elements. These combinations leave a large choices also at B site, with an average oxidation state of 4^+ at B site for the choice of divalent A cation and average oxidation state of 3^+ at B site for the choice of trivalent A cation. This basically covers all the cations in the periodic table as a possible candidate for B site in a double perovskite structure. All of the above are the possible configuration for ordered DP. However, defects are most natural to occur during the synthesis. The most prevalent defect or disorder that happens in case of DP is anti-site disorder. In case of anti-site disorder, the position of B and B$'$ site gets switched, generating defect pairs of B-B and B$'$-B$'$ instead of B-B$'$ pairs. The situation gets further complicated by the fact that such anti-site disorder or the phases have been separated by anti-phase boundaries. The critical magnetic behaviour has been investigated on these type of compounds but various debates on the disorders have been still there. For example, Sr_2FeMoO_6, which perhaps the most studied member in the double perovskite family till date and its critical analysis on single crystal shows β= 0.388, γ=1.30, and δ=4.35 which indicates it is close to the 3D-Heisenberg class [35]. Though the disorder has been there but the critical behaviour has not been affected so much [36]. Sr_2CrMoO_6 belongs to the 3D-Ising class with itinerant magnetism [37]. The critical behaviour has been studied on few of the compounds of the DP series $R_2\mathrm{MM'O_6}$ (R: rare-earth ions or Y, La; M, M$'$: transition metal ions) but the contradiction on presence of cluster phase and the nature of the cluster did not investigated in details so far. In the Chapter 6, we will discuss the critical magnetic behaviour of DP compound, $\mathrm{Gd_2CoMnO_6}$ in details.

1.7 Magnetodielectric effect in oxides

In recent times magnetodielctric (MD) effect is one of the thrilling properties of a magnetic material where the dielectric property can be tuned with the application of an external magnetic field. The strong spin-lattice coupling is the most crucial parameter for observing the strong magnetodielectric effect in a material. The materials with two magnetic sublattices (like 3d-4f based compounds) show large magnetodielctric effect near the magnetic phase transition region due to the strong correlation between spin and lattice degrees of freedom. The study of the MD effect of the material is important to explore its inherent interaction between spin and lattice. Sometimes, various properties like short-range magnetic ordering, commensurate-incommensurate transition, spin-gap transition and complex magneto-structural effect etc. can not be identified properly without the MD analysis. The study of the MD effect for chromate spinels $\mathrm{LiMCr_4O_8}$(M = Ga and In) resolves various contradiction related to its phase transition [38]. Not only from the physics point of view but the magnetodielctric effect is also one of the emerging topics in condensed matter research due to the potential applications in spintronics [39], magnetodielctric sensors, magnetic memories and various multifunctional devices, etc [40].

In the linear MD effect, the induced electric polarization or magnetization is proportional to the applied magnetic field H or electric field E, which can be expressed as $P = \alpha H$ or $\mu_0 M = \alpha E$, where α denotes the linear MD coefficient and μ_0 denotes the magnetic permeability of vacuum. However, these materials are restricted by symmetry requirements, involving simultaneous breaking of time reversal and spatial inversion symmetries. First linear MD effect has been observed in Cr_2O_3 in 1960 [41, 42]. For the technological applications, it is important to obtain a larger and constant MD effect in wider temperature and/or magnetic field regions. But the target to get large MD in a compound is very challenging to the scientific community as the strong spin lattice coupling is primary need to observe this effect. But their are various promising oxides which can show large MD near T_c like $DyCrO_4$ [43] and some of them show giant MD even near room temperature [44]. Recently, linear magnetoelectric effect has been reported in many systems such as $MnTiO_3$, $A_2M_4O_9$ (A = Nb and Ta; M = Mn, Fe, and Co), $NdCrTiO_5$, Cr_2WO_6, Co_3O_4, $MnGa_2O_4$, $MnAl_2O_4$, $CoAl_2O_4$, etc [38, 45, 46, 47, 48, 49, 50]
When different magnetic phases are present in a compound, then both linear as well as nonlinear magnetodielectric will generate [51]. Then to consider the higher nonlinear term, the spin-lattice coupled equation becomes

$$\mu_0 M = \mu_0 M(0) + \alpha E + (1/2)\gamma E^2 \tag{1.10}$$

Where $(1/2)\gamma \mathrm{E}^2$ is the nonlinear term. The rare-earth based DP materials such as La_2NiMnO_6 [52], La_2CoMnO_6 [53] are interesting for their large MD properties near room temperature. But if such a rare material can be found where the two effects (magnetodielctric and magnetocaloric) coexist that would be rather more interesting. In Chapter 7, we will discuss in details the magnetodielectric effect of the DP compound Ho_2FeCoO_6.

1.8 Motivation, context and organization of the thesis

As different compounds in manganite and Cobaltite series are extensively studied in last few decades, we have prepared some new and less studied compounds and investigated the role of DM interaction, single-ion anisotropy, frustration and cluster phase on magnetic properties of these compounds. Considering our existing magnetization, heat capacity and dielectric measurements facility, we have focused our research on different exotic magnetic, thermal and dielectric properties in some rare-earth based oxides. Three series of compounds namely, RCrTiO$_5$ (R=Dy,Ho and Gd), RFeO$_3$ (R= Gd and Ho) and double perovskite R_2MM'O$_6$ (R= Gd and Ho and M or M'= Co/Mn/Fe) have been considered for the present thesis. The selection of these interesting magnetic compounds is primarily based on literature survey. In the respective chapters, we discuss the specific motivation behind each study. The organization of the thesis is as follows. In Chapter 2, we describe briefly the method through which we have synthesized the studied materials. A short description on the instruments and the techniques, which have been used to characterize and measure different physical properties of a material, is also given in this chapter. In Chapter 3, we have investigated the nature of magnetic ground state of RCrTiO$_5$ (R = Dy and Ho) through dc magnetization and heat capacity measurements in detail. Due to the strong competition between the Cr^{3+} and R^{3+} sublattice moments, several intriguing phenomena have been observed when the magnetic state is probed at low field. Chapter 4 is devoted to the role of exchange frustration on the magnetocaloric properties of $GdCrTiO_5$. The role of geometrical frustration on the magnetocaloric effect has been previously reported theoretically and experimentally investigated on very few systems. The present results not only suggest that $GdCrTiO_5$ could be considered as a potential magnetic refrigerant at cryogenic temperatures but also promotes further studies on the role of exchange frustration for the magnetocaloric effect. In Chapter 5, the magnetocaloric properties of single crystalline $GdFeO_3$ have been investigated by magnetization and heat-capacity measurements. Remarkably, large and reversible magnetic entropy change, ΔS_m = -52.5 J/kg K, has been observed for a field change of 0-9 T at 3 K. The magnetocaloric parameters remain large down to the lowest temperature measured and are significantly larger than that reported for the other members of rare-earth (R) ortho-ferrites (RFeO$_3$) and several potential magnetic refrigerants in the same temperature range. In Chapter 6, study on critical magnetic behaviour on the double perovskite Gd_2CoMnO_6 is covered. We have shown that this ferromagnetic Gd_2CoMnO_6 compound exhibits the characteristics of clustered phase, which is quite different from that of Griffiths phase, observed in several perovskite compounds, as evidences from critical scaling analysis. In Chapter 7, we have investigated the magnetic, magneto-dielectric and magnetocaloric properties of the double perovskite (DP) compound Ho_2FeCoO_6. Finally, a summary of this thesis work has been presented in Chapter 8.

2

Experimental details

In this chapter, the methods of the studied sample preparation, its characterization and measurement techniques are discussed in details. The pollycrystalline samples RCrTiO$_5$ [R= Dy, Ho and Gd] and R_2MM'O$_6$ [R= Gd and Ho, M=Co and Fe and M' = Mn and Co] were prepared by the conventional solid state reaction method. Whereas the single crystalline RFeO$_3$ [R= Gd and Ho] compounds were prepared by the travelling solvent float zone (TSFZ) method. The powder x-ray diffraction (XRD) technique was used to check the phase purity of all the samples. The quality and the orientation of the crystallographic axes of the single crystal samples RFeO$_3$ [R= Gd and Ho] has been characterized by Laue diffraction technique. The magnetic properties of the materials have been investigated by both superconducting quantum interference device vibrating sample magnetometer (SQUID-VSM)(Quantum Design) and a physical property measurement system (PPMS)(Quantum Design). The thermal properties have been measured by the same PPMS (Quantum Design). A cryogen free measurement system (Cryogenic Ltd.) was used for dielectric properties measurement.

2.1 Sample preparation and Characterization

2.1.1 Polycrystalline sample preparation : Solid state reaction method

The solid state reaction is the most convenient and standard method to prepare polycrystalline samples with very high purity primary oxides or carbonates. The ingredients react at high temperature in their solid phases in air or a controlled atmosphere like O_2 and Ar. The successive steps of the solid state reaction process are weighing of raw oxides, intermediate grindings and heating, preparation of a pellet or cylindrical rods by hydraulic press and sintering at high temperature. To prepare the polycrystalline RCrTiO$_5$ [R= Dy, Ho and Gd], $R_2MM'O_6$ [R= Gd and Ho, M=Co and Fe and M' = Mn and Co] and RFeO$_3$ [R= Gd and Ho] powder samples, a stoichiometric mixture of pre-heated rare- earth oxides R_2O_3 and transition metal oxides were heated at 1000-1100°C for few days followed by intermediate grindings to get the single phase sample. The obtained powder was pressed into pellets or two cylindrical rods by hydraulic press of 5-8 ton and has been sintered finally at 1100°C in the same environment. All the above heat treatments were done in the O_2 environment. x-ray diffraction was used to ensure that the powder material prepared was single phase.

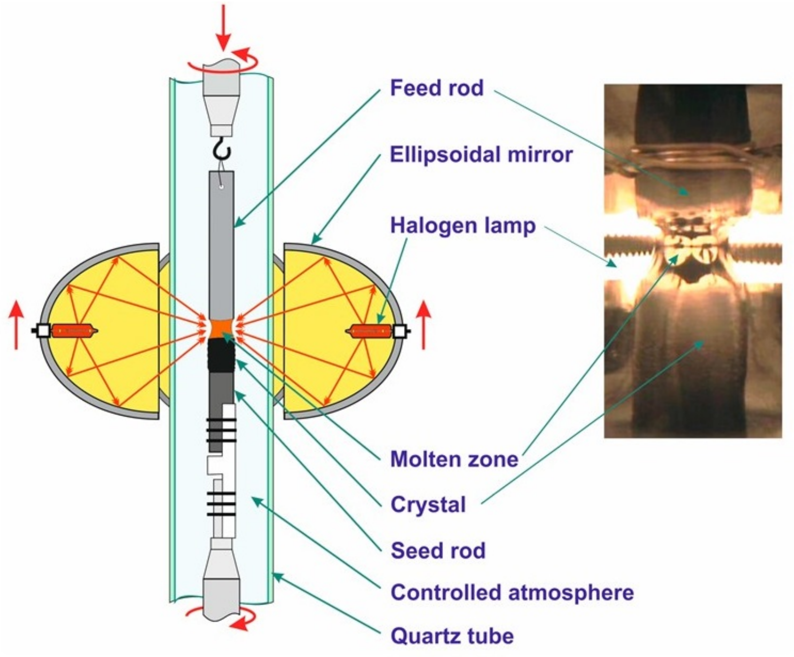

Figure 2.1: The pictorial representation of the travelling solvent float zone (TSFZ) image furnace.

2.1.2 Single crystal preparation : Travelling solvent float zone (TSFZ) method

The travelling solvent float zone method is one of the most powerful tools to prepare a high quality single crystal. The advantage of this method over the other techniques is that it avoids contamination from crucible. With the help of this TSFZ method large single crystal can be grown. Here, we have used a four-mirror optical floating zone furnace FZ-T-10000-H-VPM (Crystal System Co.) as shown in Figure 2.1 which consists of four ellipsoidal mirrors made of Pyrex glass coated with highly reflective aluminum. The maximum operating temperature is 2200 degree and the pressure ranges from 5x10^{-5} to 10 bars. There are various growth atmosphere like air, nitrogen, oxygen, argon, etc. Crystals can be obtained up to

150 mm in length and 10 mm in diameter, with a growing rate of 0.05-27 mm/h and 5-60 rpm rotating speed. This method needs two polycrystalline rods (one is feed rod and another is seed rod). The feed rod is suspended from a platinum hook and the seed rod is put onto a seed holder. The crystal growth takes place inside a quartz tube. The infrared radiation coming from four halogen lamps is reflected by the four mirrors and focused on to the sample rod. A suitable percentage of the total lamp power is applied to melt a small portion in junction ends of these feed and seed rods. After a while, when the molten portions of feed and seed rods take a round shape, they are touched in liquid state. The molten zone is floated in between seed and feed rods due to the competition between gravitational force and surface tension thats why the furnace is named as travelling solvent float zone. There are two shafts (upper and lower) which can move independently or in synchronized mode. The motion of upper shaft controls the feed speed whereas that in the lower shaft controls the seed speed. With a suitable feed and seed speed in synchronized or non-synchronized mode, the molten (floating) zone is translated downward along the length of the feed rod. The end of the molten zone gets solidified as it goes far away from the heating zone and the single crystal grows. During the entire time of crystal growth, the feed and seed rods are rotated in opposite directions to get a homogeneous microstructural texture. During the crystal growth, the growth parameters such as the pressure of the gas which is supplied as the atmosphere of crystal growth, feed or seed speed and lamp power are tuned in a controlled manner the maintain the stable growth.

2.1.3 Powder x-ray diffraction

XRD is an important tool, which is extensively used to determine the structural properties of a studied material. The application ranges of the XRD are versatile from crystalline solids to inorganic, organic molecules to biological systems. Powder XRD is performed on polycrystalline samples, where the crystallographic planes of different grains are oriented randomly. In this technique, a sample is exposed to parallel beams of monochromatic x-ray. As x-ray is an electromagnetic wave, it has been scattered mainly by the atomic electrons. If the wavelength (λ) of the incident and scattered beams remains same, purely elastic scattering occurs. In XRD measurement, we use this elastic scattering technique, which contains the information of electronic distribution of the material. For a periodic atomic arrangement of a crystal lattice, each atom scatters incident x-rays in all possible directions as shown in Figure 2.2(a). The scattered beams interfere with each other either constructively or destructively depending on the path difference of the incident and scattered x-rays. Constructive interference results in enhancement of intensity and which is observed for certain angles determined by the Bragg's law,

$$2d \sin\theta = n\lambda, \tag{2.1}$$

where d is the interplanar distance, θ is the angle between incident x-ray beam and lattice plane, and n is an integer. At present, most x-ray diffractometers operate in Bragg-Brentano geometry as shown in Figure 2.2(b). In this set-up, the x-ray source and detector move towards each other in a circle around the sample so that if the sample is at an angle θ, the detector is always at 2θ with respect to the incident beam. By scanning continuous 2θ values, one can obtain all possible

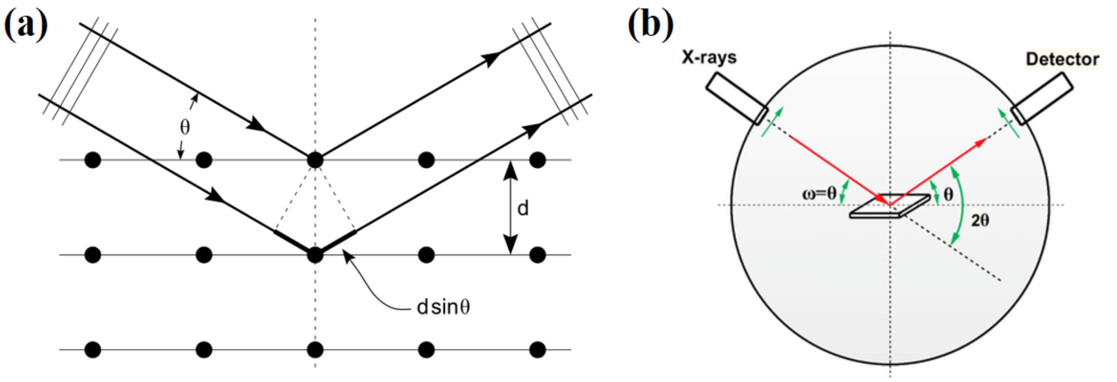

Figure 2.2: (a) Schematic diagram showing the x-ray diffraction by crystallographic planes. (b) Schematic of a x-ray diffractometer operating in Bragg-Brentano geometry.

Bragg's peaks from randomly oriented grains.

For this thesis work, in our laboratory, XRD measurements were performed in a Rigaku x-ray diffractometer (TTRAX III), which operates at 9 kW and uses Cu-$K\alpha$ radiation. The data have been collected by varying 2θ in the range 10° to 90° at intervals of 0.02 °. The samples were prepared by crushing and grinding the single crystals. To extract the space group symmetry and lattice parameters of the material, the experimental data have been analyzed by Rietveld [54] structural refinement using the FULLPROF [55] software package .

2.1.4 Laue diffraction method

The Laue diffraction method is mainly used to determine the orientation of single crystals. It is a very useful technique to identify the different crystallographic axes of a single crystal. The incident radiation can reflects or transmits from the sample. The diffracted beams form arrays of spots, that lie on curves on the film. For a particular set of planes the Bragg angle is fixed in the crystal. Each set of

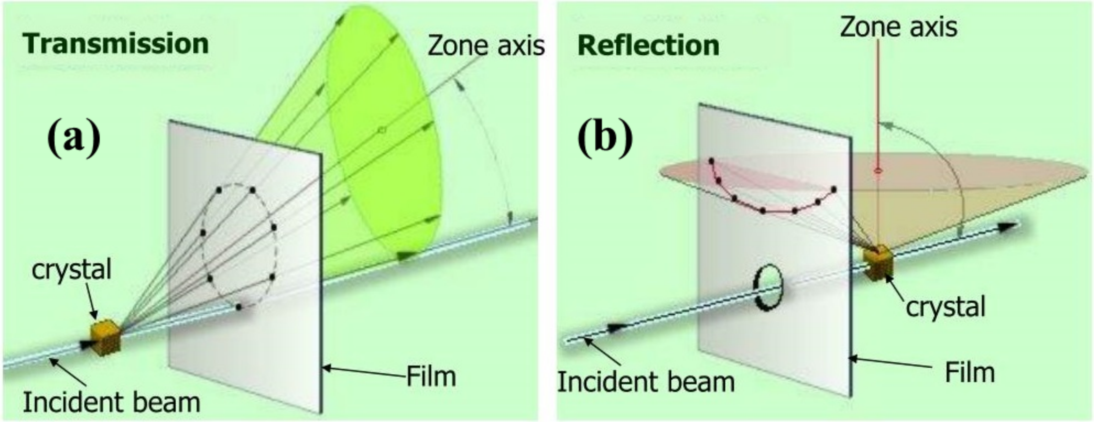

Figure 2.3: Schematic diagram showing the (a) Transmission Laue method and (b) Back reflection Laue method.

planes picks out and diffracts the particular wavelength that satisfies the Bragg law. Each curve therefore corresponds to a different wavelength. The spots lying on any one curve are reflections from planes belonging to one zone. Laue reflections from planes of the same zone all lie on the surface of an imaginary cone. The axis of the cone is known as the zone axis.

There are two practical variants of the Laue method, the transmission Laue method and the back-reflection.

Transmission Laue method: In the transmission Laue method, the film is placed behind the crystal to record beams which are transmitted through the crystal. The figure 2.3(a) demonstrates the transmission Laue method. One side of the cone of Laue reflections is defined by the transmitted beam. The film intersects the cone, with the diffraction spots generally lying on an ellipse.

Back reflection Laue method: In the back-reflection method, the film is placed between the x-ray source and the crystal. In figure 2.3(b) the reflection method of the Laue diffraction method has been shown. The beams which are diffracted in a backward direction are recorded. One side of the cone of Laue reflections is defined by the transmitted beam. The film intersects the cone, with the diffraction spots generally lying on an hyperbola.

Crystal orientation is determined from the position of the spots. Each spot can be indexed, i.e. attributed to a particular plane, using special charts. The Greninger chart is used for back-reflection patterns and the Leonhardt chart for transmission patterns. The Laue technique can also be used to determine the crystal's perfection from the size and shape of the spots. If the crystal has been bent or twisted in anyway, the spots become distorted and smeared out. The Laue diffraction of the as grown single crystal $GdFeO_3$ has been performed, which is shown in chapter 6.

2.2 Magnetic and physical properties measurement technique

2.2.1 DC magnetization measurement

MPMS SQUID-VSM and PPMS VSM were used to investigate the temperature and magnetic field dependence of the magnetization of the studied single crystals and polycrystalline materials. In most of the cases, the effect of demagnetizing field is very less. On the other hand, if the demagnetizing field has a larger value then it reduces the measured inverse susceptibility (χ^{-1}). So the value of Curie-Weiss constant Θ_{CW} changes, but the value of Curie constant as well as the effective paramagnetic moment do not change. To minimize the demagnetizing effect, for the magnetic measurements, we have used approximately parallelepiped shaped pieces with lengths much larger than the other two dimensions and the magnetic field is applied along the length of the samples.

SQUID-VSM:

SQUID-VSM is a very important instrument to detect extremely small magnetic field. The basic working principle of superconducting quantum interference device (SQUID) is based on two parallel Josephson junctions in a loop. A thin insulating layer sandwiched by two superconductors is known as Josephson junction which helps to tunnel of the Cooper pairs. The concept of flux quantization is connected with the sensitivity of SQUID magnetometer. The input current divides equally in these two parallel Josephson junctions. A screening current is produced in this loop to oppose the field when external magnetic field is applied to the superconducting loop. If the magnetic flux associated with superconducting loop is increased by half of flux quantum, then the loop energetically prefers to increase it up to a flux quantum. So induced screening current changes its direction when associated magnetic flux is increased by half integer multiples of flux quantum. If a constant basing current is applied in the superconducting loop, an oscillating voltage has been created across the junction with a period of flux quantum as shown in Figure 2.4. Flux change associated with the superconducting loop can be evaluated by counting the number of oscillations.

We have used the MPMS 3 SQUID-VSM [56] to measure the magnetization of our studied materials. It has the following properties: (i) the operating temperature ranges from 1.8 K to 400 K with a maximum temperature sweep rate of 50 K/min, (ii) the field ranges from - 7 to +7 T with a maximum field sweep rate of 700 Oe/sec, and (iii) the magnetization sensitivity is of 5×10^{-8} emu. The magnetometer has three main sections (a) dewar and probe with VSM motor (b) superconducting

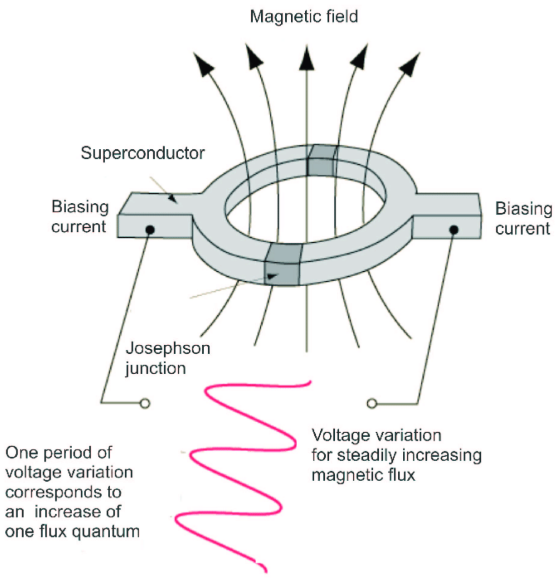

Figure 2.4: Schematic diagram illustrating principle of SQUID device.

magnet and SQUID-VSM detection system and (c) the electronic control system. The dewar consists of an inner liquid helium reservoir and outer liquid nitrogen jacket. The liquid helium is used both for maintaining the superconducting state of the magnet and detector as well as for cooling the sample space. Figure 2.5 demonstrates a schematic of the SQUID-VSM [56] detection system. The superconducting detection coils are configured in such a way so that they could not respond to uniform magnetic field and linear magnetic field gradient. Only local magnetic field produces a current in detection coil. The current in detection coils depends on the sample position where it is assumed that sample dimension is negligible compared to coils dimension. So this signal can be expressed as a function of sample position. The shape of this signal depends on sample size and shape. The current in detection coil is connected with SQUID by an inductive coupling where SQUID works as a current-voltage converter. Here sample vibrates at a certain frequency ω about the center of detection coils and gives a signal as function of

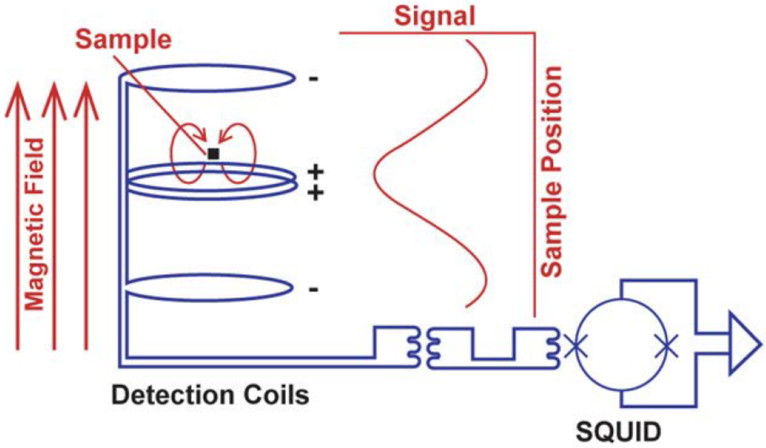

Figure 2.5: A schematic diagram of MPMS SQUID VSM detection hardware.

sample position z. The SQUID signal can be expressed as a function of time t,

$$V(t) = AB^2 \sin^2(\omega t) \tag{2.2}$$

For small vibration amplitude $V(z)$ = Az^2 and z(t) = B sin(ωt). The magnetic moment of the sample has been determined from the scaling factor A. Here B is the amplitude of sample vibration.

Vibrating sample magnetometer in PPMS:

The magnetization measurements were also done with the help of PPMS VSM option [57]. A schematic diagram of vibrating sample magnetometer is shown in Figure 2.6. The VSM option for the PPMS consists of a linear motor transport (head) for vibrating the sample, a coil for detection purpose, electronics for driving the linear motor transport and detecting the response from the pickup coils. The linear motor transport consists of an oscillator and a transducer assembly. The oscillator creates a sinusoidal signal and the transducer assembly translate it into vertical vibration. The sample attached with the sample rod vibrates with a

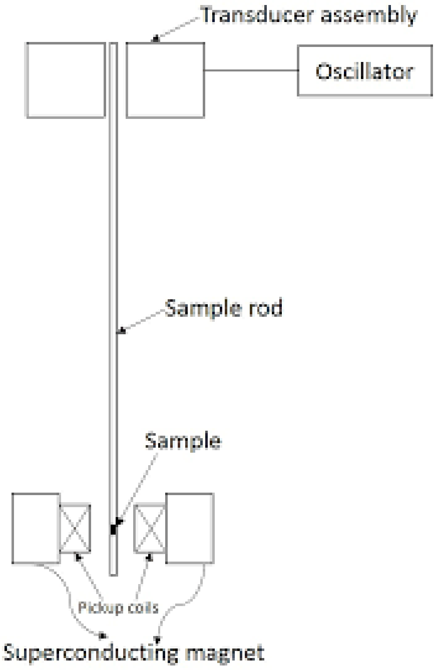

Figure 2.6: Schematic diagram illustrating principle of PPMS-VSM device.

known frequency and amplitude.Vibrating sample magnetometer operates obeying Faraday's laws of induction. This law states that rate of change of magnetic flux induces electromotive force. In this magnetometer, sample oscillates vertically in between two detection pick up coils. A constant magnetic field is applied by superconducting magnets to magnetize the sample. So, a magnetic field is created around the sample due to its magnetization. As sample is vibrating, magnetic flux is changing with time. According to Faraday's laws, a voltage is induced in detection coil. This time dependent induced voltage in pick up coil can be expressed by following equation

$$V_{coil} = d\phi/dt \tag{2.3}$$

where ϕ is magnetic flux enclosed by detection coil and t is time. As a sinusoidal oscillation is given to the sample with a fixed amplitude (A) and frequency (f) then induced voltage can be presented by the following equation,

$$V_{coil} = 2\Pi f m C A \sin(2\Pi f t) \tag{2.4}$$

where C is coupling constant and m is the magnetic moment of the sample. So the induced voltage is directly proportional to the amount of magnetization in the sample. Therefore, the magnetic moment of the sample can be determined by processing induced voltage in detection coil with the help of proper calibration of a known material.

2.2.2 Specific heat measurement

Specific heat measurements of the studied samples were done in PPMS using a two-tau relaxation method [58] which measures the heat capacity at constant pressure

$$C_p = (dQ/dT)_p \tag{2.5}$$

In heat capacity option, a certain amount of heat (Q) is applied to the sample for a certain time with a constant heater power. Then heat is removed during a cooling period. The heat capacity at a particular temperature is measured by recording the differences in temperature between the sample, sample platform, and puck during heating and cooling periods. The schematic diagram of heat capacity probe of Quantum Design PPMS is shown in Fig. 2.7. A heater and a thermometer are connected to the bottom side of the sample platform. Electrical and thermal connections to the platform heater and platform thermometer are done with the help of small wires. Sample platform remains suspended by these wires.

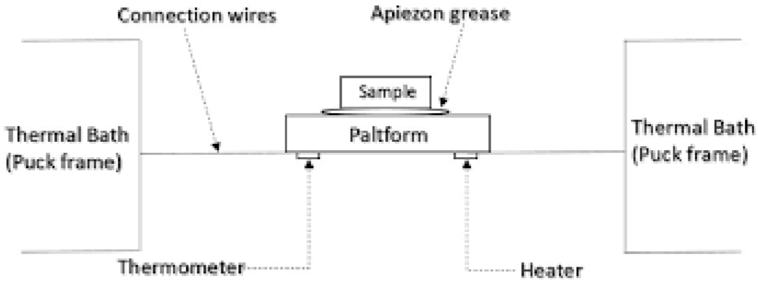

Figure 2.7: Schematic diagram illustrating principle of PPMS-heat capacity setup.

The sample is attached to the platform using Apiezon H or N grease to ensure good thermal contact. The heat capacity puck is then inserted into the PPMS, which is equipped with a 9 T magnet. During the measurement, high vacuum condition is maintained to assure no thermal loss. In high vacuum the thermal conductance between platform and thermal bath occurs only via wires. A single measurement cycle consists of a heating period followed by a cooling period. The heat capacity of an addenda (gress) measurement has been done first. Then the grease's heat capacity is subtracted from the measured signal to determine the sample heat capacity. The power supplied by the heater. The heater power P(t) is a step function, which is fixed at P_0 during the heating stage and is removed during the cooling period.

2.2.3 Dielectric constant measurement

Dielectric constant measurements were done by parallel plate method or capacitor method. In this method, parallel plate capacitor works as a sample holder where sample was sandwiched between two plates. If electric field is applied across the parallel plate capacitor, keeping the dielectric material in between two plates, then the dielectric material is polarized due to the effect of external electric field. More charges are stored in capacitor in presence of dielectric material with respect to vacuum. So dielectric material reduces the effective electric field across the capacitor by neutralizing charges at electrodes. The capacitance is inversely proportional to the electric field between the plates. If C_0 and C are the capacitance without (vacuum) and with dielectric material, they can be expressed as

$$C_0 = \epsilon_0 A/t \tag{2.6}$$

$$C = \epsilon_0 k A/t \tag{2.7}$$

where A is the area of plates; t is the distance between parallel plates; ϵ_0 is the permittivity of vacuum and k is the dielectric constant of sample. So dielectric constant of sample can be calculated using equations 2.8 and 2.9,

$$k = C/C_0 \tag{2.8}$$

Here two parallel surfaces of the sample were covered with silver paint which acts as a parallel plate capacitor and capacitance of the sample was measured by using very sensitive capacitance bridge.

3

Anomalous magnetic properties of RCrTiO$_5$ (R=Dy and Ho) compounds

3.1 Introduction

The compounds with general chemical formula RMn$_2$O$_5$ (R being rare-earth ions) crystallize in an orthorhombic structure with space group *Pbam* and are familiar for their magnetic field-induced ferroelectric behavior due to the strong magneto-electric coupling [59, 60, 61, 62, 63, 64, 65]. In these compounds, the spins are aligned antiferromagnetically along the crystallographic c axis and due to the lattice geometry and small octahedra distortion, a weak FM component of the canted spins develops perpendicular to c axis [60]. The molecular field of transition metal ions partially magnetizes the rare-earth R^{3+} sublattice and this induced moment aligns either antiparallel or parallel to the weak FM vector of Mn^{3+} [60, 61, 62]. On the other hand, the members of the RCrTiO$_5$ family, isostructural to RMn$_2$O$_5$, are much less studied [66, 67, 68, 69, 70, 71]. In RCrTiO$_5$ series, one expects to

Table 3.1: The comparative study of the lattice and fitting parameters of $DyCrTiO_5$ and $HoCrTiO_5$ compounds.

Compounds	Lattice parameters	Fitting parameters
$DyCrTiO_5$	a =7.309, b =8.634, and c =5.829 Å	R_{wp}=5.7, R_{exp}=4.6, χ^2=3.5
$HoCrTiO_5$	a =7.291, b =8.632 and c =5.824 Å	R_{wp}=6.8, R_{exp}=4.3, χ^2=5.3

observe complex and interesting magnetic behavior due to the presence of two magnetic sublattices R^{3+} and Cr^{3+}. However, there are very few reports on physical properties of this series of compounds and those are mainly on preliminary magnetic properties for some selected rare-earths [66, 67, 68, 69, 70].

In this chapter, we have investigated the role of various exchange interactions on the magnetic properties of two unexplored members of RCrTiO$_5$ series. For the first time, we have successfully synthesized $DyCrTiO_5$ (DCTO) and $HoCrTiO_5$ (HCTO) compounds and studied their magnetic properties in details over wide range of temperature and magnetic field. These compounds have been chosen for two main reasons: (1) they have large magnetocrystalline anisotropy as compared to other reported Sm-, Nd- and Gd- (no magnetocrystalline effect) based compounds [66, 68, 70, 71, 72, 73], and (2) among the rare-earth ions, both Dy and Ho have relatively large magnetic moment. The analysis of low-field magnetization data shows several anomalous magnetic properties such as magnetization reversal and spin reorientation transition. $DyCrTiO_5$ exhibits spin reorientation and exchange bias phenomena but no such behavior have been observed in $HoCrTiO_5$. The physics behind these intriguing magnetic phenomena is discussed in the results and discussion section.

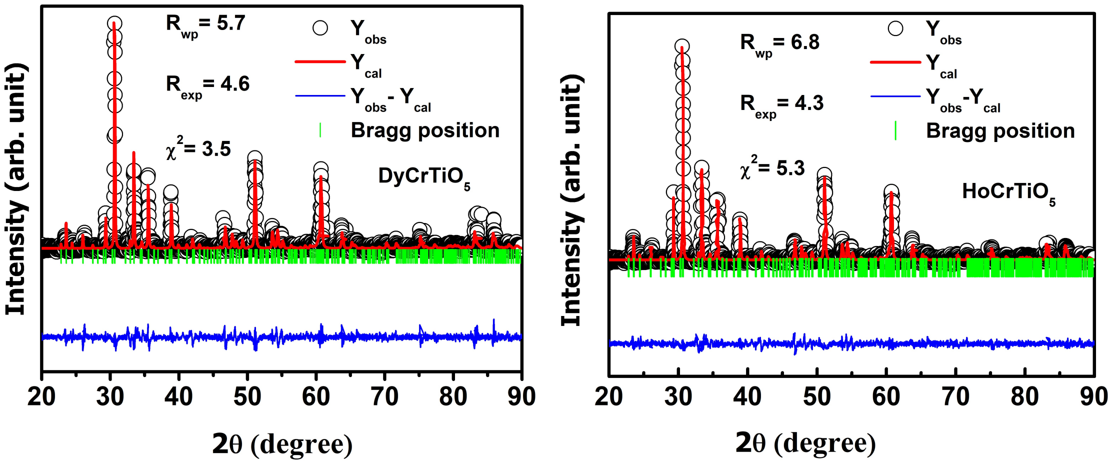

Figure 3.1: The x-ray diffraction pattern for the polycrystalline powder of (a) $DyCrTiO_5$ and (b) $HoCrTiO_5$ compounds and the best fitted results are shown.

3.2 Sample preparation, characterization, and experimental details

The polycrystalline RCrTiO$_5$ (R=Dy, Ho) samples were prepared by conventional solid-state reaction method, using high purity R_2O_3 (99.9%),(R=Dy and Ho) Cr_2O_3 (99.9%) and TiO_2 (99.9%) powders. Before use, R_2O_3 was pre-heated at 1000°C for 24 h. Well-mixed powder of R_2O_3, Cr_2O_3 and TiO_2 in a stoichiometric ratio 1:1:2 was heated at 1150°C for few days with several intermediate grindings. Finally, the green-colored RCrTiO$_5$ sample was reground, pressed into pellets under high pressure and sintered at 1350 °C for 24 h in air followed by slow cooling. The phase purity and crystal structure of these samples were determined by high-resolution x-ray powder diffraction (Rigaku TTRAX III) with CuK$_\alpha$ radiation (λ =1.5406 Å) at room temperature. The Rietveld refinement was done for the structural analysis of diffraction pattern of powdered RCrTiO$_5$

samples with FULLPROF software. The observed peaks in the diffraction pattern have been indexed well with orthorhombic unit cell having *Pbam* crystallographic symmetry. Within the x-ray resolution, we have not observed any peak due to the impurity phase. The experimental x-ray intensity profile along with the theoretical fit and the Bragg positions are shown in Figure 3.1(a) for the Dy-based compound and in Figure 3.1(b) for Ho-based one. The lattice and others fitting parameters determined from the Rietveld profile analysis are shown in Table 3.1. These values of lattice parameters are close to those reported for the $GdCrTiO_5$ (GCTO) compound [69, 74]. For the magnetization measurements, a small piece of rectangular shape sample with length much longer as compared to other two sides ($\sim 4\times 0.5\times 0.6$ mm^3) was cut from the polycrystalline pellet. The temperature and magnetic field dependence measurements were carried out by using a 7 T SQUID-VSM, (Quantum Design). To minimize the demagnetization effect, the magnetic field has been applied along the longest dimension of the sample. The superconducting magnet of the 7 T SQUID-VSM system attains a field history dependence remnant magnetic field that after charging the magnet to high fields in order to neglect this remnant field during the low field measurements we have oscillated the magnetic field very carefully. In this work, we have measured the magnetization using two different protocols: (a) the zero-field-cooled (ZFC) magnetization and (b) the field-cooled (FC) magnetization. In ZFC protocol, the sample was cooled down from room temperature to lowest temperature in absence of any applied magnetic field and data were collected during the warming cycle after switching on the field. In FC cycle, the measurement was performed during the cooling process under applied magnetic field. A small piece of sample was used for the heat capacity (C_p) measurements, in a PPMS (Quantum Design) by the

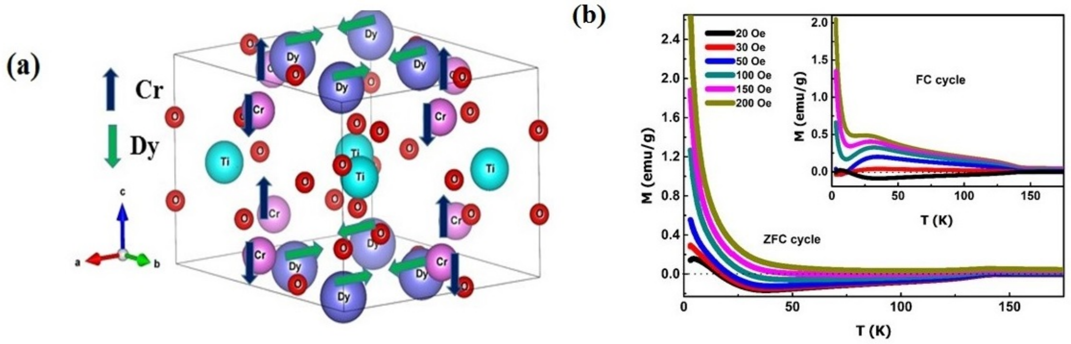

Figure 3.2: (a) Shows the schematic magnetic structure with a possible configuration of spins on each sublattice of $DyCrTiO_5$. In $DyCrTiO_5$, the Cr moments order antiferromagnetically below 139 K but the Dy moments do not show any long-range ordering and (b) the main panel shows temperature dependence of magnetization at low fields (20-200 Oe) in ZFC mode and the inset shows same plot for FC mode for $DyCrTiO_5$.

relaxation technique.

3.3 Results and discussions

3.3.1 Temperature dependence magnetization for $DyCrTiO_5$

The schematic magnetic structure of RCrTiO$_5$ compound with R=Dy, has been shown in the Figure 3.2(a), as discussed in introduction section. In Figure 3.2(a) the possible configuration of spins of two sublattices (Dy^{3+} and Cr^{3+}) have been shown, which are responsible for the magnetic properties of this studied material. The temperature dependence of dc magnetization for $DyCrTiO_5$ has been measured both under zero-field-cooled and field-cooled conditions at various applied magnetic fields in the temperature range 2-300 K. The $M(T)$ curves in ZFC mode for low magnetic fields ($H \leq$200 Oe) are shown in the main panel of Figure 3.2(b) and the inset displays similar plots under FC mode. It is clear from Figure 3.2(b) that the temperature dependence of magnetization is very complex. Depending on temperature and field strength, M can be positive as well as negative. Also, the nature of $M(T)$ curves for various fields in ZFC mode is quite different from the corresponding FC mode. In order to explore the underlying mechanism behind such complex evolution of magnetization in DCTO compound with temperature, we thoroughly discuss $M(T)$ curve for each magnetic field separately. As the nature of the $M(T)$ curves at low fields, $H \leq 50$ Oe, are more exotic, we analyse these results at first in details. Figures 3.3(a)-(c), show $M(T)$ curves in both ZFC and FC modes for 20, 30 and 50 Oe, respectively. The complex nature of these curves is due to the strong coupling between Dy^{3+} and Cr^{3+} sublattice magnetization. The $M(T)$ curve at 20 Oe in ZFC mode has been considered as a representative where we have pictorially displayed the spins for Dy^{3+} and Cr^{3+} to explain the above mentioned competition. Cr^{3+} spins show canted AFM ordering at $T_N^{Cr} \sim 140$ K, determined from the position of the maximum in dM/dT curve. However, the heat capacity measurement, to be discussed later on, reveals slightly lower value for the AFM transition temperature, $T_N^{Cr} = 139$ K. We are basically interested for the temperature region below T_N^{Cr}, where M displays very unusual and nonmonotonic T dependence. At low temperature, M increases rapidly and shows a peak around 4.5 K. Usually, the $M(T)$ curve of several rare-earth transition metal oxides exhibits a peak at low-temperature due to the long-range AFM ordering of rare-earth moments. However, from the heat capacity measurements, we have confirmed that Dy^{3+} does not show any long-range ordering down to 1.8 K. Due to the antisymmetric Dzyaloshinskii-Moriya exchange interaction [75] between the Cr^{3+} spins, a weak FM component starts to develop below T_N^{Cr}. On the other hand, the

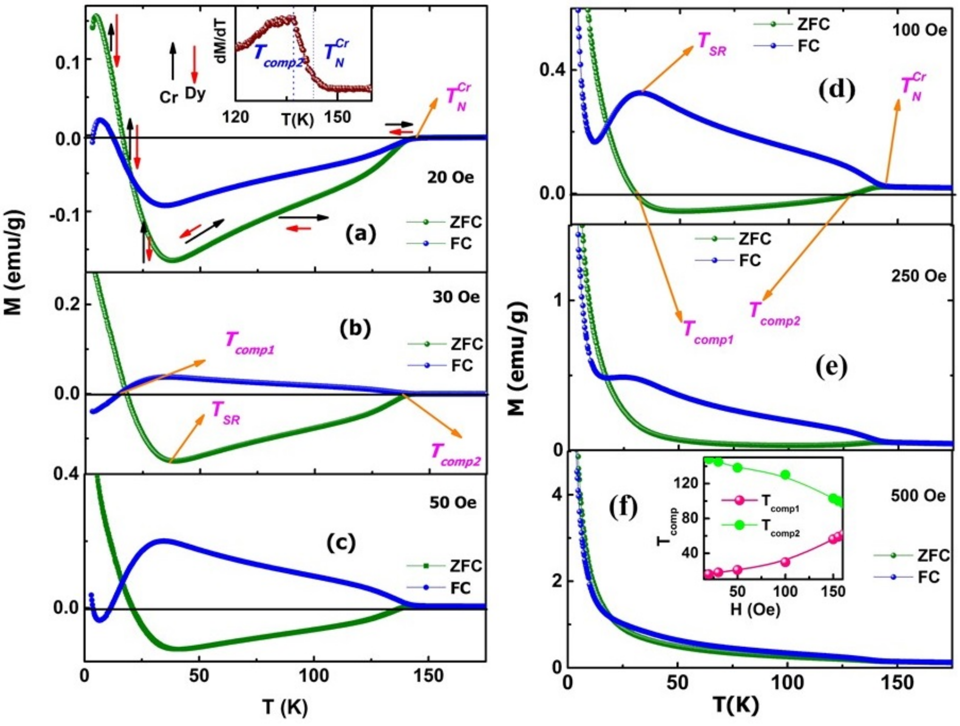

Figure 3.3: (a) The main panel shows the $M(T)$ curve at 20 Oe. The red and black arrows indicate the moment of Dy and Cr, respectively and the length of the arrow denotes the value of the net moment. The inset shows the derivative of moment with temperature near T_N^{Cr} and T_{comp2}, $M(T)$ at (b) 30 Oe , (c) 50 Oe , (d) 100 Oe, (e) 250 Oe and (f) 500 Oe and the inset in (f) shows the variation of T_{comp1} and T_{comp2} with magnetic field for DyCrTiO$_5$ compound.

anisotropic exchange [76, 77, 78] between Dy^{3+} and Cr^{3+} spins creates an effective magnetic field at Dy^{3+} site in the opposite direction to the canted Cr^{3+} moment. Above 4.5 K, M decreases rapidly due to the faster decrease of Dy^{3+} moment. All the local induced-moments of Dy^{3+} and the FM moment of Cr^{3+} cancel with each other at 16 K, as a result, the net magnetization becomes zero, which is the compensation temperature T_{comp1}. Just above T_{comp1}, as the resultant magnetization vector orients along the opposite direction to the external magnetic field, the net magnetization becomes negative. There are various origins for the negative magnetization or temperature induced magnetization reversal: (i) first-order magnetostrictive transition that enhances the orbital angular momentum of transition metal ion in some orthovanadates [79, 80], (ii) strong competition between the single-ion anisotropy of R^{3+} and antisymmetric DM exchange interaction of transition metal ion spins [79, 81] and (iii) different temperature dependence of sublattice magnetization arising from different molecular fields acting on magnetic ions located at to non-identical crystallographic sites as proposed by Neél for ferrimagnet [82, 83, 84]. As RCTO compounds do not exhibit any first-order magnetostrictive transition, we rule out the role of orbital angular momentum. In several systems, the MR phenomenon has been explained by considering the competition between the DM and anisotropic magnetocrystalline interaction [79, 81, 85]. In these systems, the energy scale of the DM and anisotropic magnetocrystalline interaction is comparable with the energy scale associated with the magnetization reversal phenomenon, as a result, MR has been observed at relatively high fields up to few kOe [79, 81, 85]. However, the above mentioned competition may not be the origin for the occurrence of MR in DCTO and HCTO because, in these compounds, MR has been observed at a few tens of Oe only. In the studied compounds, due to the lattice geometry and small distortion of CrO_6 octahedron, a weak FM component of the canted spins develops, as evident from our $M(H)$ measurements below T_N^{Cr}. The local molecular field originates due to this canted Cr^{3+} spin acts on the rare-earth ions, which couples antiferromagnetically with Cr^{3+} spin. As a result, the R^{3+} sublattice moment, with a net effect antiparallel to that of the Cr^{3+} spins and with a different temperature dependence, could give rise to a compensation effect as in the case of $HoCrO_3$, $GdCrO_3$ and $SmMnO_3$ [86, 87, 88]. The magnetization above T_{comp1} decreases rapidly with increasing temperature and displays a pronounced minimum at T_{SR}~37 K, where another magnetic phase transition takes place due to the reorientation of Cr^{3+} spins. Above T_{SR}, the FM moment of Cr^{3+} spin starts to rotate continuously from one axis toward another axis. Though the presence of a weak FM component has already been reported for isostructural RMn$_2$O$_5$ series of compounds[62], the spin reorientation transition has not been reported in RCrTiO$_5$ series so far. We would like to mention that both magnetization reversal and spin reorientation phenomena are absolutely new observation in RCrTiO$_5$ types of compounds, though these behavior have been reported for various perovskites and double-perovskites [89, 90, 91]. With further increase in temperature above T_{SR}, the net magnetization increases slowly and again vanishes at a second compensation temperature T_{comp2}=136 K. Therefore, negative magnetization has been observed in the temperature window 16 K<T<136 K. In the paramagnetic (PM) region above T_N^{Cr}, the overall magnetization becomes positive due to the thermal fluctuation. To show the transitions T_{comp2} and T_N^{Cr} more clearly, we have plotted the first-derivative of M with temperature in the inset of Figure 3.3(a), which shows that the net moment changes sharply below T_N^{Cr}. For FC cycle at 20 Oe, M is also negative between the two compensation temperatures but T_{comp1} is slightly smaller. However, the minimum at T_{SR} is deeper in ZFC cycle as compared to FC magnetization, as a result, a huge bifurcation occurs between these two curves. In the FC cycle also, a clear anomaly has been observed at 4.5 K and T_N^{Cr} in $M(T)$ curve. We would like to mention that T_{comp} does not correspond to any thermodynamic phase transition. Though the nature of $M(T)$ curves in ZFC mode for 30 and 50 Oe fields is similar to that for 20 Oe, no anomaly is visible at 4.5 K in Figures 3.3(b) and (c). Also, the magnetization is slightly less negative for 30 and 50 Oe than that for 20 Oe. This indicates that with increasing field strength, a small fraction of the spins aligns along the applied field direction. As a result, T_{comp1} shifts slightly toward higher temperature for 30 and 50 Oe. On the other hand, the nature of FC magnetization curves for 30 and 50 Oe is completely different from that for 20 Oe. For these two fields, magnetization is positive, except below $\sim$15 K. Due to the dominating contribution of Dy^{3+} moments, M increases rapidly and becomes positive at 50 Oe for T<3 K. $M(T)$ shows a broad peak at T_{SR} for both 30 and 50 Oe, . From the above discussions, it can be concluded that the effect of single-ion anisotropy energy is more clearly manifested in the ZFC mode of magnetization. The above mentioned anomalous magnetic properties at low fields encourage us to study the nature of $M(T)$ curves at relatively higher fields. In Figures 3.3(d)-(f), M is plotted as a function of temperature for 100, 250 and 500 Oe, respectively. The ZFC magnetization curve for 100 Oe is quite similar to that mentioned previously for low fields. However, with the increase in field strength, the range over which M is negative shrinks progressively and the absolute value of M between T_{comp1} and T_{comp2} decreases. For example, at 150 Oe, M is marginally negative in the temperature range 50-130 K (Figure 3.2(b)). The nature of $M(T)$ curve in FC mode for 100 Oe is similar to that for 50 Oe, except the absence of negative magnetization at low temperature. For higher fields, 250 and 500 Oe, ZFC magnetization is positive down to lowest measured temperature and one cannot track T_{SR}. On the other hand, both T_{SR} and T_N^{Cr} are traceable in FC curves up to 500 Oe. At 500 Oe, the hysteresis between FC and ZFC magnetization is very small. Though the spin-reorientation transition broadens with increasing field strength, T_{SR} is found to be almost field independent. At low applied field, the net moment in the PM state aligns along the field direction but realigns opposite to the field slightly below the T_N^{Cr}. However, above 150 Oe, a

Table 3.2: The comparative study on T_N^{Cr}, magnetic moments of rare-earth ions and spin-orbit coupling for different compounds of RCrTiO$_5$ series.

Compounds	Magnetic moment of R^{3+} ions	Spin orbit coupling (L.S)	T_N^{Cr} K	Reference
NdCrTiO$_5$	(L=6, S= 3/2, J= 9/2)	9	21	[68]
GdCrTiO$_5$	(L=0, S= 7/2, J= 7/2)	0	–	[72, 74]
SmCrTiO$_5$	(L=5, S= 5/2, J= 5/2)	12.5	180	[70]
DyCrTiO$_5$	(L=5, S=5/2, J= 15/2)	12.5	139	This work
HoCrTiO$_5$	(L=6, S= 2, J= 8)	12	137	This work

significant fraction of spins does not realign opposite to the field direction when the temperature is reduced below T_N^{Cr}, as a result, the anomalous magnetization reversal vanishes. In the inset of Figure 3.3(f), the variation of T_{comp1} and T_{comp2} with magnetic field have been shown. From this figure, one can see that T_{comp1} and T_{comp2} shift toward higher and lower temperature, respectively with increasing magnetic field strength and slightly below 200 Oe, these two temperatures merge with each other at $\simeq$80 K.

For better understanding of the nature of $M(T)$ curve, we have plotted the inverse susceptibility χ^{-1} ($=H/M$) with temperature in the main panel of Figure 3.4(a) for the FC mode at magnetic field 100 Oe. At high temperature above 150 K, susceptibility follows the Curie-Weiss law, $\chi=C/(T-\theta_{CW})$, where C is the Curie constant and θ_{CW} is the Curie-Weiss temperature. From the linear Curie-Weiss fit, we have deduced the values of θ_{CW} and effective PM moment μ_{eff} as -18 K and 11.3 μ_B/f.u., respectively. The negative value of the θ_{CW} indicates that the AFM interaction dominates magnetism.

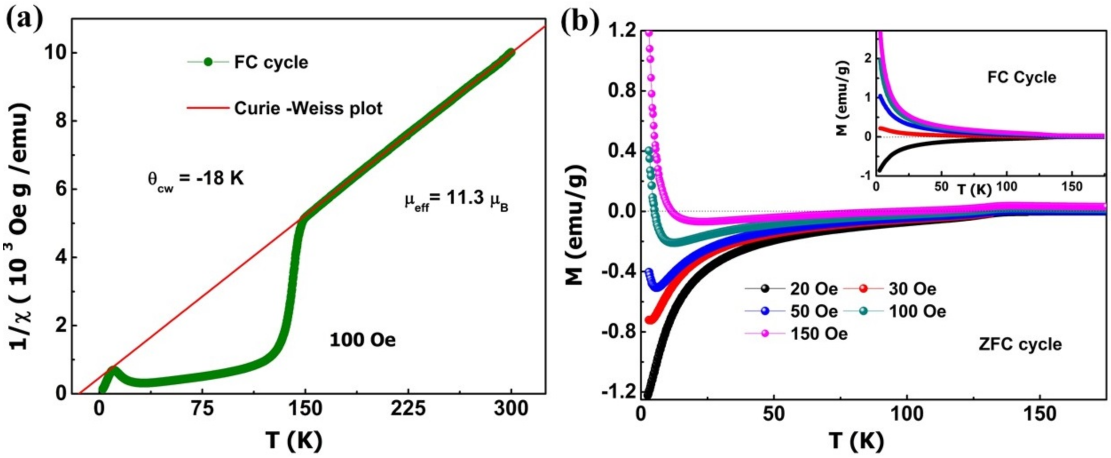

Figure 3.4: (a) The temperature dependence of the inverse-susceptibility χ^{-1} and Curie-Weiss plot for 100 Oe field for the DyCrTiO$_5$ compound. (b) The main panel shows temperature dependence of magnetization at low fields (20-150 Oe) in ZFC mode and the inset shows same plot for FC mode for HoCrTiO$_5$ compound.

3.3.2 Temperature dependence of magnetization for HoCrTiO$_5$

In this section, we present and analyse the results on T dependence of M for HoCrTiO$_5$ at different fields. Ho is the next element to Dy in the periodic table with almost same effective magnetic moment but different magnetocrystalline anisotropy. The thermal variation of M in ZFC mode is shown in the main panel of Figure 3.4(b) for various magnetic fields, whereas the inset shows the behavior of $M(T)$ in FC mode. As in the case of DCTO, magnetization is also negative for HCTO at low fields but over a slightly wider temperature range. In contrast to DCTO, no anomaly is observed in both modes of $M(T)$ curves below 140 K, except the sharp rise at low temperature. In spite of several similarities in the nature of $M(T)$ curves of HCTO and DCTO, there are important differences. In order to identify some differences in the nature of magnetic ground state of HCTO and DCTO systems, we have analysed the $M(T)$ curves of HCTO in details separately at low fields 20, 30, and 50 Oe in Figures 3.5(a)-(c) and at relatively higher fields 100, 150, and 500 Oe in Figures 3.5(d)-(f). $M(T)$ curve for 20 Oe field shows a clear anomaly below 140 K due to the long-range AFM ordering of Cr^{3+} moments as shown in Figure 3.5(a). Thus, T_N^{Cr} for both DCTO and HCTO compounds is almost same. Below T_N^{Cr}, M decreases smoothly with decreasing T and the net magnetization becomes zero at T_{comp}~128 K. With further decreasing T below T_{comp}, M becomes negative for both FC and ZFC cycles. However, the magnetization in ZFC mode is more negative than in FC mode and M does not show any tendency to increase in the positive direction. For 30 and 50 Oe, the qualitative nature of ZFC magnetization curve is very similar to that for 20 Oe, except at low temperature as shown in Figures 3.5(b) and (c). At low temperature, M decreases slowly for 30 Oe whereas M exhibits a clear deep at 5.1 K and increases rapidly below 5 K for 50 Oe field. We would like to mention that this behavior of M is not due to the onset of AFM ordering of Ho moments. Heat capacity measurement reveals that similar to Dy^{3+}, Ho^{3+} moments do not exhibit long-range AFM ordering down to 1.8 K. Such a sharp increase in M at low temperature has also been reported in Ho-based double-perovskite compound Ho_2FeCoO_6 due to the short-range interaction between Ho^{3+} moments [90]. On the other hand, the behavior of FC magnetization curves for 30 and 50 Oe is completely different from that for 20 Oe. In FC mode, M is positive and increases monotonically with decrease in T. Unlike DCTO, the nature of magnetization curves for HCTO is not complex, which may be attributed to the absence of spin reorientation transition of Cr^{3+}. Due to the spin reorientation transition near 37 K, the intense exchange interaction between the Dy^{3+} moments and the weak FM vector of canted Cr^{3+} makes the ground state of DCTO very complex, which is clearly manifested at low

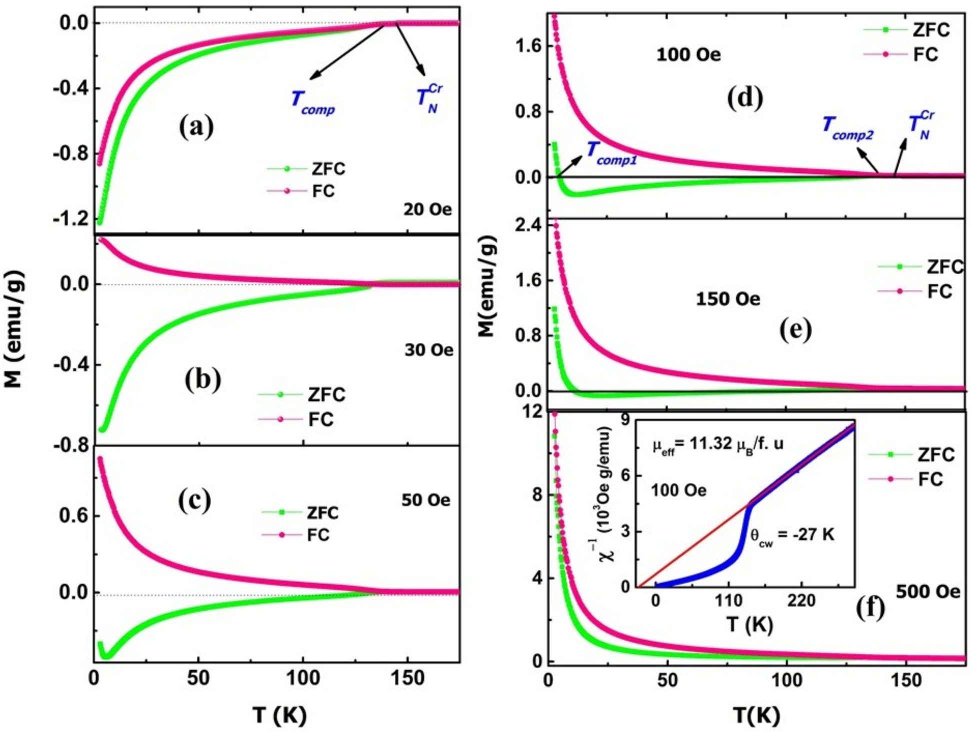

Figure 3.5: $M(T)$ at (a) 20 Oe, (b) 30 Oe, (c) 50 Oe, (d) 100 Oe, (e) 150 Oe and (f) 500 Oe and the inset in (f) shows the Curie-Weiss plot for $HoCrTiO_5$ compound for 100 Oe.

magnetic fields. From the comparative study, one can argue that in case of HCTO, the weak FM component of Cr^{3+} moment arising from the DM interaction does not rotate but is restricted to orient along one of the crystallographic axes, as a consequence, the spin reorientation transition is absent. In this context, we would like to mention that it is not obvious to observe the spin reorientation transition in all compounds of the same series. For example, some members of the $RFeO_3$ series do not show spin reorientation transition [92]. Another very crucial parameter that should be taken into account to compare and contrast the magnetic ground state of these two systems is the single-ion anisotropy of rare-earth ions. The single-ion anisotropy exchange energy is three times larger for Dy^{3+} than that for Ho^{3+} moment [93]. Temperature dependence of ZFC magnetization for 100 and 150 Oe, as shown in Figures 3.5(d) and (e), is similar to that for 50 Oe. The only difference is that the negative magnetization appears in a narrower temperature range and another compensation occurs at low temperature around 5 K. Figures 3.5(d) and (e) show that with increasing field, T_{comp2} shifts toward lower temperature at a faster rate as compared to T_{comp1}. The nature of $M(T)$ curves in FC modes at 100 and 150 Oe is similar to that for FC cycle at 50 Oe. Whatever the differences observed between the DCTO and HCTO systems at low fields, those progressively weaken with increasing field and disappear at high fields. At 500 Oe, M in both ZFC and FC cycles is positive and the nature of $M(T)$ curve in Figure 3.5(f) is very similar to that for DCTO compound. We have also plotted the inverse magnetic susceptibility with temperature for HCTO compound as shown in the inset of Figures 3.5(f). At high temperature above 150 K, χ follows the Curie-Weiss law. From the Curie-Weiss linear fit, we have deduced θ_{CW}= -27 K and μ_{eff} = 11.32 μ_B/f.u. The deduced values of μ_{eff} for DCTO and HCTO are close to the theoretically expected moment calculated using the two-sublattices R^{3+} and Cr^{3+}. We now compare the observed T_N^{Cr} of DCTO and HCTO with that reported for other members of the RCrTiO$_5$ series. For the well studied GdCrTiO$_5$ compound, Cr^{3+} spins do not show any long-range AFM ordering but exhibit a weak anomaly around 150 K due to the short-range ordering [72, 74]. For SmCrTiO$_5$, T_N^{Cr} (=180 K) is slightly higher [70], whereas for NdCrTiO$_5$, T_N^{Cr} is as low as 21 K [68]. The reported nature of $M(T)$ curve for the SmCrTiO$_5$ compound is also very unusual below T_N^{Cr}. A spin reorientation-like feature has been observed around 35 K [70]. In Table 3.2, the magnetic moments of rare-earth ions, spin-orbit coupling ($L.S$) and T_N^{Cr} for this series of materials are presented. From Table 3.2, one can see that the T_N^{Cr} is high for R= Dy, Ho and Sm but almost an order of magnitude smaller for other R ions. This result suggests that both the spin-orbit coupling and magnetic moment of R^{3+} ions play important role for the long-range AFM ordering of Cr^{3+} spins.

3.3.3 Heat capacity of $DyCrTiO_5$ and $HoCrTiO_5$

In order to understand the nature of above mentioned phase transitions more clearly and to determine the transition temperatures accurately, we have investigated the temperature dependence of heat capacity down to 1.8 K, for both the samples. The main panel of Figure 3.6(a) shows C_p versus T plot for $DyCrTiO_5$ compound. At 139 K, a clear peak has been observed, which corresponds to T_N^{Cr}. In the inset (A) of Figure 3.6(a), the enlarged view of the $C_p(T)$ curve in the vicinity of Cr^{3+} moments ordering is shown. Below T_N^{Cr}, C_p decreases with decreasing temperature down to 6 K. With further decrease in temperature below 6 K, C_p increases without showing any peak [inset (B)]. In several rare-earth transition metal oxides, heat capacity rises sharply at low temperature and exhibits a pronounced λ-like anomaly due to the long-range AFM ordering of R moments [69, 94, 176, 96]. It appears from the nature of $C_p(T)$ curve that a peak may appear slightly below 1.8 K. However, it is unlikely that the peak would be λ-like in nature because C_p increases rather slowly with a weak downward curvature. $C_p(T)$ may show a broad peak due to the short-range magnetic ordering of Dy^{3+} moments. Indeed, the detailed analysis of magnetic field dependence of heat capacity and entropy for $HoCrTiO_5$ compound supports this view. There is no visible anomaly in the $C_p(T)$ curve near T_{SR}. However, $dC_p(\mathrm{T})/dT$ shows a faster increase with T above T_{SR} and a maximum slightly above T_{SR}, as shown in the inset (C) of Figure 3.6(a). It may be mentioned that in RMnO$_3$ series, $C_p(T)$ curve of $DyMnO_3$ shows a very

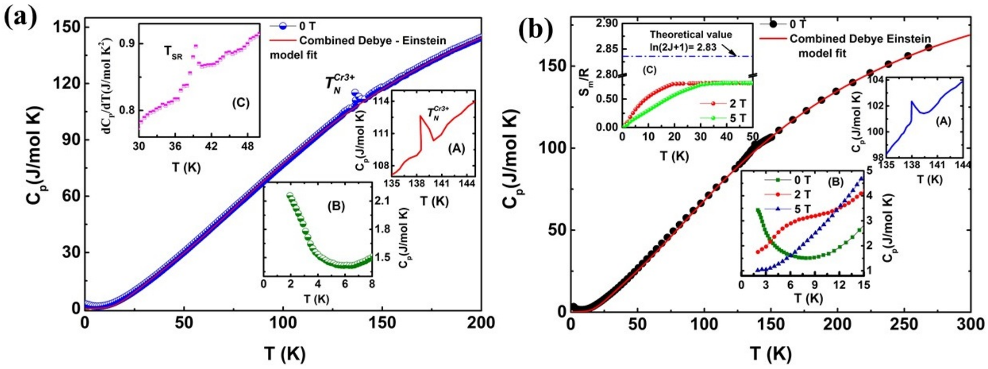

Figure 3.6: (a) The main panel shows the temperature dependence of heat capacity (C_p) whereas the red curve indicates the fitted combined Debye-Einstein model. The inset (A) shows the peak at T_N^{Cr}=139 K due to the AFM ordering of Cr^{3+} moments and the inset (B) shows the sharp increase in C_p at low temperature. Inset (C) shows a weak anomaly at $dC_p(\mathrm{T})/dT$ vs T curve for $DyCrTiO_5$ compound. (b) The main panel shows the temperature dependence of heat capacity (C_p) whereas the red curve indicates the fitted combined Debye-Einstein model. The AFM transition of Cr^{3+} sublattice is shown in inset (A) and the inset (B) shows the field dependence C_p. Inset (C) shows the magnetic entropy at 2 and 5 T fields for $HoCrTiO_5$ compound.

weak peak at T_{SR} while no anomaly is observed for the $HoMnO_3$ compound [97]. In RFeO$_3$ series of materials, spin reorientation transition is known for more than a half-century [98]. They show strong anomaly at T_{SR} in $M(T)$ curve like the present system. However, no anomaly is observed at T_{SR} in the heat capacity data for $DyFeO_3$ and $SmFeO_3$ [99]. This suggests spin reorientation is a very weak thermodynamic transition in these systems. The main panel of Figure 3.6(b) displays the $C_p(T)$ curve for the second studied compound $HoCrTiO_5$. As in the case of DCTO, a clear peak has been observed around T_N^{Cr}=137 K due to the ordering of Cr^{3+} moments. In the inset (A) of the Figure 3.6(b), the magnified view of the AFM transition region of the Cr^{3+} moments ordering has been shown. Below T_N^{Cr}, similar to DCTO, C_p decreases monotonically down to 7 K and then increases slowly with further decrease in T, as shown in the inset (B) of Figure 3.6(b). The magnetic field dependence of heat capacity has also been shown in the inset (B). With the application of magnetic field, the low-temperature upturn suppresses sharply while C_p increases in the high temperature region. Thus magnetic entropy shifts toward higher temperature with the application of magnetic field. At 2 T, $C_p(T)$ shows a very broad anomaly around 6 K. C_p becomes very small at low temperature at 5 T. Although we could not measure C_p below 1.8 K, the analysis of field dependence of C_p and its comparison with $GdCrTiO_5$ will be useful for understanding the nature magnetic ground state of DCTO and HCTO. At zero-field, C_p of $GdCrTiO_5$ increases rapidly below 5 K and exhibits a huge peak at 0.9 K due to the long-range AFM ordering of Gd moments [69]. Though the peak broadens and shifts toward higher temperature with the application of field, the effect is not as strong as in HCTO. In GCTO, peak is clearly visible even at 7 T field [74]. We believe that the broad nature of the $C_p(T)$ peak of HCTO at 2 T could be due to the Schottky anomaly associated with the short-range ordering of Ho moments. To shed some more light on this issue, we have estimated the value of magnetic entropy (S_m) for different applied magnetic fields by integrating (C_m/T). To estimate the magnetic contribution to heat capacity, we have calculated the lattice heat capacity. For this, the $C_p(T)$ curve has been fitted with the combined Debye plus Einstein model above 40 K, excluding the region near T_N^{Cr}. C_m is obtained after subtracting the lattice heat capacity part from C_p. The calculated values of magnetic entropy for 2 and 5 T fields are shown in the inset (C) of the Figure 3.6(b). Below 1.8 K, $C_m(T)$ curve was extrapolated linearly to 0. As expected, $S_m(T)$ for both the fields tends to saturate at a common value. Remarkably, the saturation value of S_m/R is almost five times smaller than the theoretical value (2.83) and very close to the value of ordered Kramer's doublet mole as observed for $DyFeO_3$ [99]. Using the same method, we have also calculated S_m at zero field for both DCTO and HCTO and observe that the calculated values of S_m are close to that for 2 and 5 T. Thus, it is very unlikely that C_p will increase rapidly below 1.8 K. The huge discrepancy between the theoretical and experimental entropy indicates the absence of long-range ordering of Dy^{3+} and Ho^{3+} moments. In this context, we would like to mention that the calculated value of entropy for GCTO compound of the present series is very close to the theoretical value [74].

3.3.4 Isothermal magnetization of $DyCrTiO_5$ and $HoCrTiO_5$

For $DyCrTiO_5$ compound, we have recorded $M(H)$ loops at various temperatures to observe the effect of the above mentioned transitions on coercive field (H_{cr}) and remanent magnetization (M_r). In several rare-earth based compounds, the strong coupling between two magnetic sublattices is clearly manifested in the temperature dependence of H_{cr} [86, 100, 101]. In the main panel of Figure 3.7(a), $M(H)$ curves for DCTO have been shown at some representative temperatures. One can see from the inset (A) of Figure 3.7(a) that, $M(H)$ at 130 K, which is slightly below T_N^{Cr}, exhibits a weak hysteresis at low fields, while at higher fields, M increases almost linearly with H like a typical antiferromagnet/paramagnet. The nature of $M(H)$ curve is qualitatively similar to that observed in other canted antiferromagnets [86, 100, 101]. The inset (B) of Figure 3.7(a) shows the $M(H)$ loop at low temperature $T\leq$ 10 K. At 2 K and 7 T, the value of magnetization is calculated to be 6.3 μ_B/f.u. For the accurate determination of the FM contribution to M, we have fitted the measured $M(H)$ data to well known Stearns and Cheng

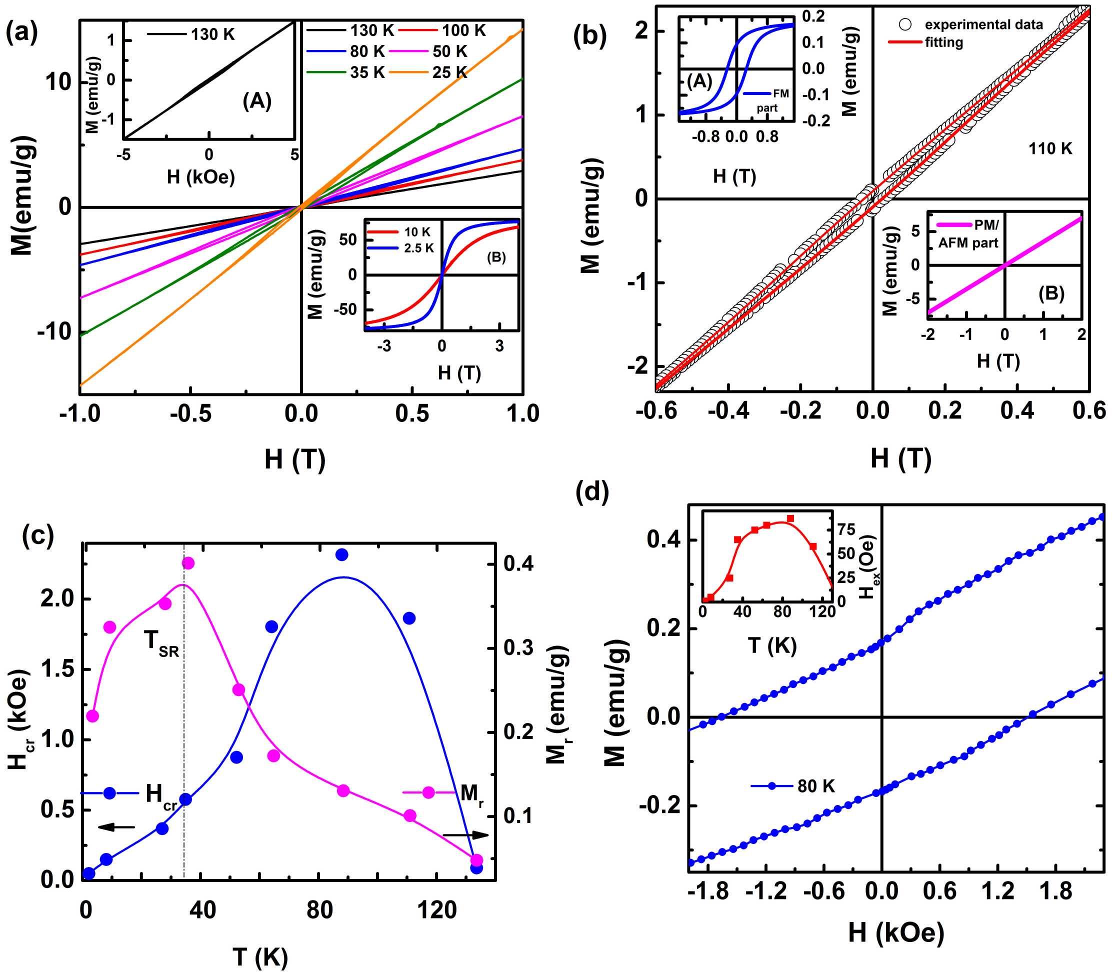

Figure 3.7: (a) The main panel shows $M(H)$ curves below T_N^{Cr} and the inset (A) shows $M(H)$ curves in the vicinity of T_N^{Cr} for the canted antiferromagnetic DyCrTiO$_5$. The inset (B) shows $M(H)$ curves at low temperature below 10 K. (b) The main panel shows $M(H)$ data fitted with the **equation (3.1)** and inset (A) shows the FM part and inset (B) shows the AFM/PM part of the $M(H)$ curve. (c) The temperature variation of the coercive field (H_{cr}) and remanent magnetization (M_r) are shown in the main panel. The solid lines are guide to eye. (d) The main panel and the inset (A) display the enlarge view of asymmetric nature of $M - H$ loop in the low-field region for 80 K and 35 K respectively and the inset (B) shows the temperature dependence of exchange bias for DyCrTiO$_5$ compound.

expression [102, 103],

$$M(H) = \left(\frac{2M_s}{\pi}\right)\tan^{-1}[\left(\frac{H \pm H_{cr}}{H_{cr}}\right)\tan\left(\frac{\pi S}{2}\right)] + \chi H \tag{3.1}$$

where the first term is the FM hysteresis loop and the second term takes care of the linear component of AFM/PM contribution. Here, S, defined as $S{=}M_r/M_s$, where M_s is the saturation magnetization, determines the squareness of the magnetization loop. The fitted curve at 110 K is shown in the main panel of Figure 3.7(b) as a representative. The extracted FM and AFM/PM contributions are shown in the insets (A) and (B) of Figure 3.7(b), respectively. From the obtained FM loops at different temperatures, we have calculated H_{cr} and M_r and plotted them as a function of temperature in the main panel of Figure 3.7(c). These plots show that both H_{cr} and M_r exhibit non-monotonic temperature dependence. Below T_N^{Cr}, H_{cr} increases with decreasing temperature and passes through a broad maximum around 90 K. The maximum value of H_{cr} is about 2.3 kOe. However, the $H_{cr}(T)$ curve is asymmetric about the maximum. This is because H_{cr} decreases at a much slower rate with T below T_{SR}. The qualitative nature of $H_{cr}(T)$ curve is similar to that reported for several canted antiferromagnets [86, 100, 101]. A slope change in $H_{cr}(T)$ curve around T_{SR} has also been observed in $DyFeO_3$ [104]. Figure 3.7(c) shows that the nature of T dependence of M_r is very complicated. With decreasing T, initially M_r increases slowly and then increases rapidly in the region 60-40 K. With further decrease in T below 40 K, M_r decreases slowly followed by an abrupt decrease at low temperature. Thus $M_r(T)$ exhibits a clear peak close to T_{SR}. Anomaly at T_{SR} in $M_r(T)$ curve has also been reported for other material [105]. At low temperature, the $M(H)$ curves are not symmetric about the origin but shifted toward negative H axis. Two representative plots are shown in the main panel and in the inset (A) of Figure 3.7(d) for 80 K and 35 K, respectively. The asymmetric nature of $M(H)$ curves is due to the finite exchange bias (H_{ex}) effect. The temperature dependence of H_{ex} is shown in the inset (B) of Figure 3.7(d). $H_{ex}(T)$ exhibits a broad peak around 85 K similar that observed in $H_{cr}(T)$ curve and decreases rapidly below T_{SR}. Several Cr- and Fe-based perovskites also show exchange bias effect which has been correlated to reorientation of Cr^{3+} and Fe^{3+} spins, respectively [104, 106, 107]. To compare and contrast the observed results of DCTO with HCTO, we have also measured $M(H)$ for HCTO. In the main panel of Figure 3.8(a), the $M(H)$ curves have been shown in the same temperature range as that for DCTO. The $M(H)$ curve at 120 K displayed in the inset (A) of Figure 3.8(a) exhibits a weak hysteresis. We also observe very weak hysteresis in $M(H)$ curve at 130 K, which is close to T_N^{Cr}. The qualitative nature of $M(H)$ curve is similar to that observed in DCTO compound. In the inset (B) of Figure 3.8(a), the $M(H)$ curves at low temperatures ($T \leq 25$ K) are shown. At 2 K and 7 T, the calculated value of magnetization for HCTO is 7.4 μ_B/f.u. This value of magnetic moment is about 17% higher than that observed for DCTO. However, the experimental values of magnetic moment for both DCTO and HCTO are significantly smaller than the theoretical values of the free Dy^{3+} and Ho^{3+}. This discrepancy is due to the strong single-ion anisotropy. We have calculated H_{cr} and M_r at different temperatures below T_N^{Cr} using the same method as in the case of DCTO. In the main panel of Figure 3.8(b), one representative fit with Eq.(1) to experimental data at 50 K is shown. The estimated FM and AFM/PM contributions to M as a function of temperature are shown in the insets (A) and (B) of Figure 3.12(b), respectively. The H_{cr} and M_r are plotted in the main panel of Figure 3.8(c). In this material, no exchange bias effect is observed.

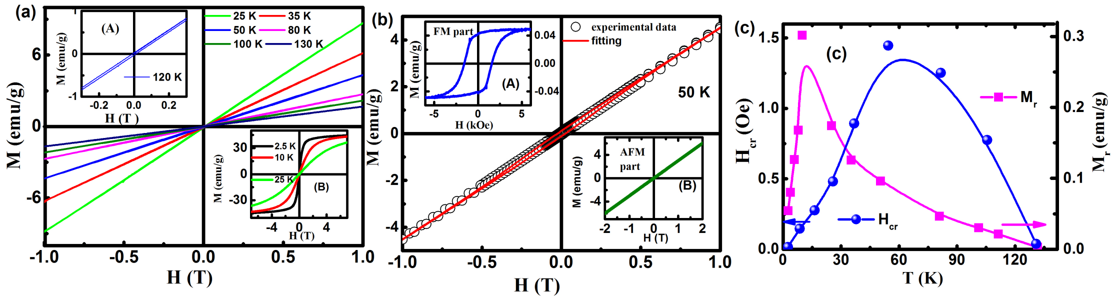

Figure 3.8: (a)The main panel shows the $M(H)$ loops due to the canted antiferromagnetic nature of HoCrTiO$_5$ below T_N^{Cr}. The inset (A) shows the $M(H)$ loop in the vicinity of T_N^{Cr} and inset (B) shows the $M(H)$ curves at low temperature below 25 K. (b) The main panel shows $M(H)$ data fitted with the **equation (3.1)** and inset (A) shows the FM part and inset (B) shows the AFM/PM part of the $M(H)$ curve. (c) The temperature dependence of coercive field (H_{cr}) and remanent magnetization (M_r) for HoCrTiO$_5$ compound. The solid lines are guide to eye.

From the figure, it is clear that H_{cr} exhibits a nonmonotonic temperature dependence similar to DCTO. H_{cr} becomes maximum at 50 K and the maximum value is about 1.4 kOe. With decreasing temperature below 50 K, H_{cr} decreases rapidly and becomes very small ($\sim$ 5 Oe) at low temperature (2 K). Initially, M_r increases with decreasing temperature and then decreases rapidly below 10 K. The rapid decrease of M_r at low temperature may be due to the increase of the short-range interaction of Ho^{3+} moments. In DCTO, a clear anomaly is observed around T_{SR} in $M_r(T)$ curve. However, no such anomaly is observed in $M_r(T)$ for HCTO. The very nature of temperature dependence of H_{cr} is the manifestation of interplay of two magnetic sublattices in RCTO. The initial increase in H_{cr} below T_N^{Cr} is due to the contribution from the Cr^{3+} sublattice moment. The nature of temperature dependence of H_{cr} can be explained by the Stoner-Wohlfarth model [108]. According to this model, H_{cr} is related to magnetocrystalline anisotropy constant (K_A) by the equation H_{cr}=(K_A/M_s). Usually, K_A is proportional to $(M_s)^m$ and m can be significantly larger than 1. Thus, in a simple ferromagnet or canted antiferromagnet, H_{cr} is expected to follow the temperature dependence of M_s, i.e., will increase with decreasing T and saturate at low temperature. Thus, the observed nonmonotonic behavior of H_{cr} with temperature for the present compounds cannot be explained by the magnetocrystalline alone. The decrease of H_{cr} at low temperature as shown in Figures. 3.7(c) and 3.8(c), however, can be explained by taking into account the exchange interaction of Cr^{3+} and R^{3+} sublattice moments. The initial increase in H_{cr} with decreasing temperature is due to the antisymmetric DM interaction in the Cr^{3+} sublattice. As the Cr^{3+}-Cr^{3+} interaction saturates at low temperature, contribution from the paramagnetic R sublattice via anisotropic R^{3+}-Cr^{3+} interaction becomes increasingly dominating which results the decrease in H_{cr}. On the contrary, the isotropic interaction between the two sublattices of RCTO does not contribute to coercivity [101].

3.4 Summary and conclusions

In this work, we have prepared RCrTiO$_5$ (R= Dy and Ho) compounds and studied their magnetic properties in details. New and complex magnetic properties like canted AFM ordering of Cr^{3+} spins and temperature-induced magnetization reversal have been observed. The spin reorientation transition has been observed below T_{SR}~37 K, where the easy axis of FM component of Cr^{3+} moments starts to rotate from one crystallographic axis to another in $DyCrTiO_5$ compound while this phenomenon is absent in $HoCrTiO_5$. Also, $DyCrTiO_5$ shows exchange bias effect. The different temperature dependence of the two sublattices magnetization and the large single-ion anisotropy of rare-earth ions play crucial role for these intriguing magnetic phenomena. The observed magnetic properties encourage further study of magnetic spin texture on single crystal by neutron diffraction or other techniques.

4

Giant magnetocaloric effect in exchange-frustrated $GdCrTiO_5$ antiferromagnet

4.1 Introduction

The environment friendly and low-temperature potential magnetocaloric materials are used in cryogenic technology in space science, for the liquefaction and storage of hydrogen in fuel industry and to achieve sub-Kelvin temperature in laboratory for the basic research [109, 110, 111, 112, 113, 114, 115, 116, 117, 118, 119, 120, 121, 122, 123, 124, 125, 126, 127]. Paramagnetic salts are the standard refrigerant materials to achieve the sub-kelvin temperature using adiabatic demagnetization technique. The high density and very large magnetic moments in a magnetic material enhance the efficiency of magnetic refrigeration [115, 116, 117, 118, 119, 120, 128]. Several rare-earth transition metal oxides and intermetallic compounds carrying large magnetic moments have become attractive candidates for the low-temperature magnetic refrigeration [59, 97, 129, 130, 131, 132, 133, 134, 135, 136]. In these materials, the rare-earth magnetic moments order at low temperature and a strong suppression of the magnetic entropy takes place in the vicinity of the order-disorder phase transition with the application of magnetic field. However, the value of the magnetic entropy change, ΔS_{m}, decreases rapidly and becomes very small just few Kelvin below the transition temperature and thereby limits the lowest temperature achievable by the magnetic refrigeration technique. This is one of the major drawbacks for refrigeration using magnetically ordered materials. Recently, it has been shown that magnetic frustration significantly enhances the cooling power due to the presence of finite residual magnetic entropy well below the Neel temperature [59, 97, 136]. Frustration leads to infinite degeneracy of the magnetic ground state which implies the presence of a macroscopic number of local zero-energy modes in absence of magnetic field. However, in presence of magnetic field, a non-degenerate fully polarized spin state of the antiferromagnet is achieved above the saturation field. Adiabatic demagnetization of this state corresponds to condensation of the above-mentioned local zero-energy modes and thereby produces a large change in magnetic entropy. The role of frustration on the magnetocaloric effect has been investigated theoretically for classical Heisenberg antiferromagnets on different geometrically frustrated systems such as kagome, garnet, and pyrochlore lattices [137, 138]. It has been observed that the pyrochlore lattice is the most frustrated among the above-mentioned three systems and offers the fastest cooling rate under adiabatic demagnetization [137, 138]. The role of frustration, which is due to the bond-dependent anisotropic exchange interactions or competing magnetic exchange interactions, on the magentocaloric effect should be explored for complete understanding the frustration induced enhancement of the magnetic cooling power.

The compounds of the type $R\mathrm{Mn_2O_5}$ (R being rare-earth ions), have attracted a lot of attention due to their magnetoelectric coupling and magnetic-field induced ferroelectric behavior. Besides magnetoelectric properties, $R\mathrm{Mn_2O_5}$ shows the ability to be a good magnetic refrigerant at cryogenic temperature [59, 60, 63, 64, 65]. However, the members of the family $R\mathrm{CrTiO_5}$ isostructural to $R\mathrm{Mn_2O_5}$ were paid very little attention [68, 139, 140]. In orthorhombic $R\mathrm{CrTiO_5}$, the $\mathrm{Cr^{3+}}$ ions are interspaced between the R^{3+} and $\mathrm{Ti^{4+}}$ ions and the $\mathrm{Cr^{3+}}$ spins are collinear along the crystallographic c axis whereas the moments of R^{3+} lie on the ab plane [72, 73]. The schematic crystal structure of $\mathrm{GdCrTiO_5}$ is shown in Figure 4.1(a) and the magnetic structure with spin orientation of magnetic sublattice has been shown in Figure 4.1(b) In the present work, we have studied the magnetic and magnetocaloric properties of $\mathrm{GdCrTiO_5}$ compound. $\mathrm{GdCrTiO_5}$ has chosen as a low-temperature refrigerant material for two main reasons: (i) the large spin momentum of localized $4f$ shell electrons of $\mathrm{Gd^{3+}}$ (S=7/2) and (ii) very low AFM transition temperature (T_N) of Gd sublattice. Magnetic and thermodynamic properties suggest that $\mathrm{GdCrTiO_5}$ is a frustrated magnet [69, 72, 73]. Due to strong frustration, the Gd moments order at very low temperature (0.9 K), whereas the $\mathrm{Cr^{3+}}$ moments do not show any long-range ordering [69, 72]. The competing magnetic exchange interactions from two sublattices are the origin of the frustration in $\mathrm{GdCrTiO_5}$ compound. Also, $\mathrm{GdCrTiO_5}$ is electrically insulating and magnetization does not show thermal and field hysteresis which are important criteria for magnetic refrigeration.

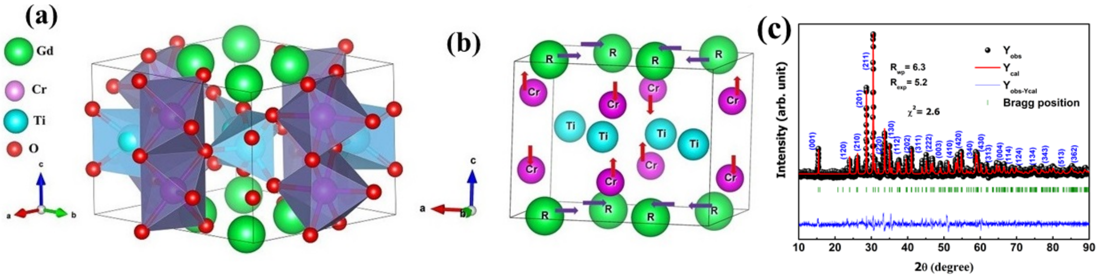

Figure 4.1: (a) The orthorombic crystal structure of $GdCrTiO_5$. The polyhedra formed by chromium (Cr) and titanium (Ti) with oxygen (O) atoms are shown schematically. (b) Magnetic structure of RCrTiO$_5$ and the arrow indicates the orientation of magnetic moment of R^{3+} and Cr^{3+}. In $GdCrTiO_5$, the Gd moments order antiferromagnetically below 0.9 K but the Cr moments do not show any long-range ordering. (c) The x-ray diffraction pattern of the polycrystalline powder of $GdCrTiO_5$.

Table 4.1: The atomic positions obtained from the Rietveld refinement of room temperature XRD of $GdCrTiO_5$ compound.

Elements	X	Y	Z
Gd	0.16081	0.19045	0
Cr	0	0.5	0.15319
Ti	0.11930	-0.15443	0.5
O_1	0.11600	-0.27281	0.25618
O_2	0.15262	0.45428	0
O_3	0.15088	0.40262	0.5
O_4	0	0	0.3004

4.2 Sample preparation and experimental details

The polycrystalline $GdCrTiO_5$ sample was prepared by conventional solid-state reaction method using high purity primary oxide powders. Before use, Gd_2O_3 was pre-heated at 900°C for 24 h. Well-mixed powder of these oxides in a stoichiometric ratio according to the molecular weight in the compound, was heated at 1250°C for few days with intermediate grindings. Finally, the green-colored $GdCrTiO_5$ sample was reground, pressed into pellets under high pressure and sintered at 1400 °C for 24 h in air followed by slow cooling. We have performed the x-ray diffraction experiments on the powder sample and analyzed the data by Rietveld structural refinement using FULLPROF software package. The x-ray diffraction pattern of the studied material is shown in Figure 4.1(c). All the observed peaks in the diffraction pattern can be indexed well with orthorhombic unit cell having Pbam crystallographic symmetry. Within the x-ray resolution, we did not observe any peak due to the impurity phase. The lattice parameters determined from the Rietveld profile analysis are a =7.4385, b =8.5814, and c =5.7782 Å, which are very close to the reported values [69]. The atomic positions obtained from Rietveld refinement of room-temperature XRD are presented in Table 4.1. A small piece of rectangular shape sample was cut from the polycrystalline pellet for the magnetization (M) measurements. The temperature and magnetic field dependence of magnetization measurements have been carried out using a 7 T SQUID-VSM, (Quantum Design). For the isothermal magnetization, the data have been recorded in the field range 0-7 T at different temperatures between 2 and 35 K, and the temperature dependence of magnetization was measured in the range 1.8-400 K. The heat capacity (C_p) measurement was performed by relaxation method down

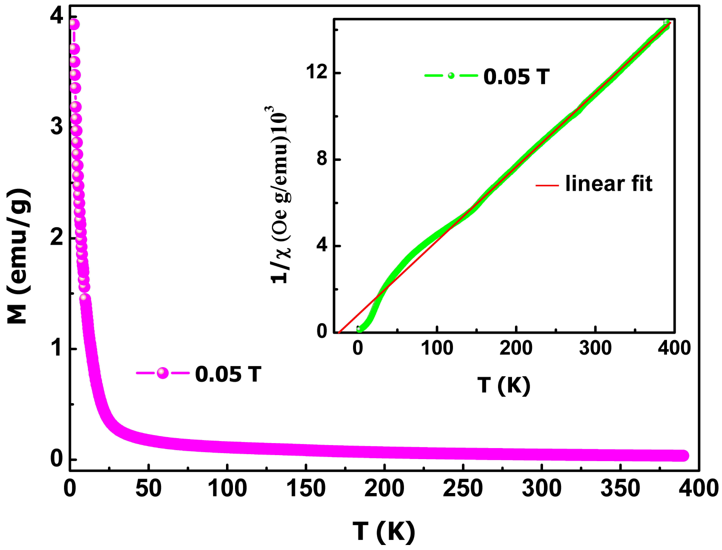

Figure 4.2: The main panel shows the temperature dependence of magnetization for $GdCrTiO_5$ at 0.05 T and the inset shows the Curie-Weiss fit to inverse susceptibility (H/M) at high temperature.

to 1.8 K in applied fields up to 7 T in a PPMS, (Quantum Design). Thermal conductivity was measured via a four-probe technique using the thermal transport measurement option in the same PPMS. The typical dimension of the sample used in thermal transport study is 4×2×1 mm^3.

4.3 Results and discussions

4.3.1 Temperature dependence magnetization

The main panel of Figure 4.2 shows $M(T)$ curve of $GdCrTiO_5$ for an applied field of 500 Oe. M increases with decrease in T but no clear signature of long-range magnetic ordering is observed down to 2 K. For better understanding the nature of magnetic ground state of $GdCrTiO_5$, the inverse dc susceptibility, χ^{-1},

(χ=M/H) has been plotted as a function of temperature in the inset of Figure 4.2. At high temperature above 150 K, susceptibility follows the Curie-Weiss law, χ=$C/(T-\theta_{CW})$, where C is the Curie constant and θ_{CW} is the Curie-Weiss temperature. From the linear fit to the high temperature data, we have calculated the values of effective paramagnetic moment μ_{eff}=8.8 μ_B/f.u. and θ_{CW}=-24 K. These values match well with the previously reported ones [73]. Negative θ_{CW} suggests that the dominating exchange interaction in $GdCrTiO_5$ is AFM. The above value of μ_{eff} is larger than the effective moment of Gd^{3+} (7.94 μ_B/Gd) ion in the PM state, indicating the contribution in susceptibility from both the Gd^{3+} (S=7/2) and the Cr^{3+} (S=3/2) spins. With decreasing temperature, χ^{-1} starts to deviate from the linear behavior below ~150 K, which is quite high. This deviation of $\chi^{-1}(T)$ at high temperatures well above θ_{CW} may be due to the strong spin fluctuations in the PM state as a result of short-range magnetic correlation. Several frustrated rare-earth transition metal oxides exhibit strong spin fluctuations due to their nearly triangular network of the magnetic ions [141, 142, 143, 144]. As a result, the long-range AFM ordering in these compounds sets-in at a much lower temperature than the deduced Curie-Weiss temperature; the magnetic energy scale of the system. The reduction of AFM transition temperature, T_N, is a signature of frustration and the value of the ratio θ_{CW}/T_N can be used as a measure of the spin frustration strength [141, 142, 143]. The spin system is classified as the one with strongly frustrated, if this ratio exceeds 10, because the simple mean-field theory fails to explain such a huge reduction in T_N [143]. In hexagonal manganites (RMnO$_3$), the maximum value of θ_{CW}/T_N is reported to be ~10 and these systems are considered to be strongly frustrated ones [141, 142, 143]. As the present system orders antiferromagnetically below 0.9 K and the observed values of θ_{CW}

are within 24-33 K [69, 73], we find $26<\theta_{CW}/T_N<37$, which is significantly larger than the value reported for the hexagonal manganites. Thus, $GdCrTiO_5$ can be considered as a strongly spin frustrated system like several other multiferroics.

4.3.2 Isothermal magnetization

In RCrTiO$_5$ family of compounds, the detailed analysis of magnetic and thermodynamic properties has not been done so far. There are only few reports on magnetic and magnetoelectric properties of Nd-based compounds. In the previous chapter we have shown that in the presence of two sublattices, the magnetic properties of these materials are very complicated. For $NdCrTiO_5$, the temperature dependence of magnetization shows a very weak anomaly at 21 K and a sharp peak at 13 K. In earlier reports, the peak at 13 K was assigned to AFM transition of Cr^{3+} and Nd^{3+} moments [140]. However, the recent magnetic, magnetoelectric and heat capacity data suggest that the Cr^{3+} moments undergo AFM transition at 21 K and then induce the order of the Nd^{3+} moments via an exchange coupling, in contrast to a direct cooperative ordering of the Nd^{3+} spin subsystem [140]. On the contrary, in $GdCrTiO_5$, significant larger moment of Gd^{3+} as compared to Cr^{3+} causes a strong spin fluctuation and suppresses the ordering of Cr^{3+} sublattice. Only Gd moments show AFM ordering at very low temperature [69]. Basu *et al.* studied the dielectric response and Raman effect in this system as a function of temperature [72]. They observed a clear anomaly in both dielectric constant and loss factor above 100 K and this anomaly pronounces and shifts towards higher temperature side with the increase in frequency. Raman scattering also shows anomaly below 150 K, where the inverse susceptibility curve starts to deviate from linearity. The ob-

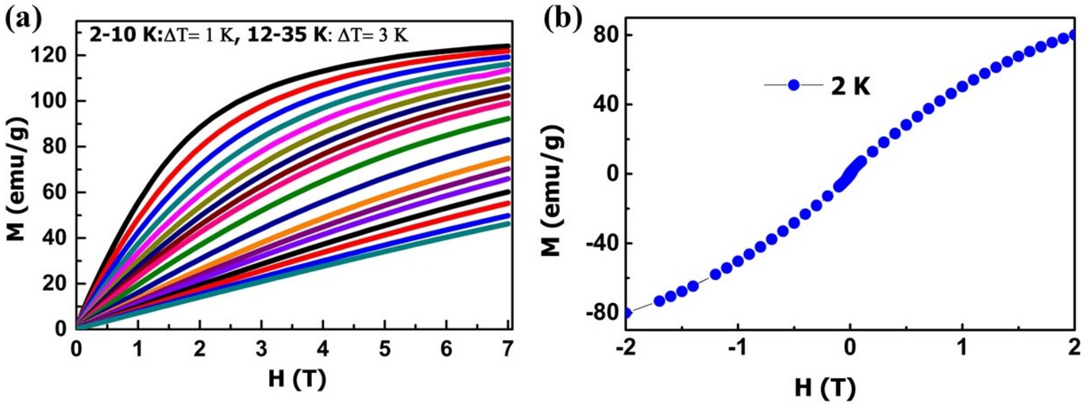

Figure 4.3: (a) The isothermal magnetization plots for $GdCrTiO_5$ in the temperature range of 2-35 K and (b) shows the hysteresis loop at 2 K in the low-field region.

served phenomena have been attributed to short-range ordering of Cr^{3+} moments [72]. In $SmCrTiO_5$, $M(T)$ curve shows a distinct feature at 180 K and downward curvature over a wide temperature range below 180 K which is to some extent similar to that observed in $GdCrTiO_5$ and has been attributed to AFM ordering of Cr^{3+} moments [70].

The nature of phase transition is important in refrigeration technology. The second-order magnetic phase transition is always preferable than the first-order. Generally, second-order phase transition exhibits very low or no hysteresis, whereas the first-order transition may exhibit significant thermal and field hysteresis which is undesirable in magnetic cooling technology because the large hysteresis loss affects the efficiency of the studied material. The sharp λ-like anomaly at 0.9 K in heat capacity of $GdCrTiO_5$ suggests the second order nature of AFM-PM transition [69]. In order to explore the influence of magnetic field on magnetic ground state, we have measured the field dependence of magnetization in $GdCrTiO_5$ up to 7 T at different temperatures in the range 2-35 K. The field dependence of M is shown in Figure 4.3(a). M increases monotonically with the increase in H

and tends to saturate at high fields and low temperature. $M(H)$ curves are like a Brillouin function of a paramagnet. At 2 K and 7 T, the value of magnetic moment is 7.4 μ_B/f.u which is about 6% higher than the spin only moment of Gd, indicating a small contribution from the Cr sublattice. We have measured the field dependence of M between -7 and 7 T at few temperatures. Figurure 4.3(b) shows the five-segment $M(H)$ curve at 2 K for field up to 2 T, as a representative. $M(H)$ does not display any hysteresis or anomaly. However, from the temperature dependence of pyroelectric current measurement below 10 K, it has been proposed that the strong alignment of the PM moments of Gd with an applied field $H>$ 1 T forces a canting of Cr^{3+} moments and the canted moments of Cr^{3+} allow the inverse Dzyaloshinskii-Moriya interaction which breaks the inversion symmetry of the crystal and gives rise to improper spin-driven ferroelectric effect [73]. The absence of any anomaly in magnetization suggests that the effect of field-induced transition of Cr^{3+} moments on magnetic properties is very weak.

4.3.3 Magnetic entropy change

The field-induced isothermal magnetization indicates large magnetic entropy change in $GdCrTiO_5$. In order to test whether this material is suitable for magnetic refrigeration in the low-temperature region, the magnetic entropy change has been calculated using the Maxwell equation, $\Delta S_m = \int_0^H (dM/dT)dH$. As the magnetization measurements are done at discrete field and temperature intervals, ΔS_m is numerically calculated using the following expression,

$$\Delta S_\mathrm{m} = \sum_i \frac{M_{i+1} - M_i}{T_{i+1} - T_i} \Delta H_i \tag{4.1}$$

where M_i and M_{i+1} are the magnetic moments at temperatures T_i and T_{i+1}, respectively for a change in magnetic field ΔH_i. Using the above equation, ΔS_m has been calculated from the magnetic field dependence of magnetization at different temperatures. The temperature dependence of ΔS_m for field variation up to 7 T has been shown in Figure 4.4(a). ΔS_m is found to be very large and negative down to the lowest measured temperature. The maximum value of ΔS_m ($-\Delta S_\mathrm{m}^{max}$) increases with increase in field and reaches as high as 36 J kg^{-1} K^{-1} for a field change of 0-7 T, which is more than double of the previously reported values of ΔS_m for other members of the RMn$_2$O$_5$ family [59, 145, 146]. We would also like to mention that the observed value of ΔS_m is significantly larger than that reported for several rare-earth transition metal oxides and intermetallic compounds [121, 122, 123, 124]. A comparative study of ΔS_m of GdCrTiO$_5$ with other rare-earth based oxide compounds in the same field and temperature range has been shown in Table 4.2.

Apart from the value, the nature of temperature dependence of ΔS_m is very important for magnetic refrigeration. In a typical ferromagnet or antiferromagnet, ΔS_m increases with decreasing T in the PM state but it decreases rapidly below the onset of long-range ordering temperature, i.e., ΔS_m decreases on the both sides of T_C or T_N. In this context, it may be noted that undoped and doped EuTiO$_3$, EuDy$_2$O$_4$ and GdVO$_4$ exhibit huge magnetocaloric effect at low temperature [94, 147, 148, 149, 150]. The values of $\Delta S_\mathrm{m}^{max}$ in these compounds are also comparable to the present system. However, for the compounds mentioned above, $\Delta S_\mathrm{m}(T)$ shows a strong decrease in the low-temperature region and in some cases, ΔS_m becomes small positive. On the other hand, ΔS_m in the present system does not decrease down to 2 K but a saturation-like behavior appears below 5 K for

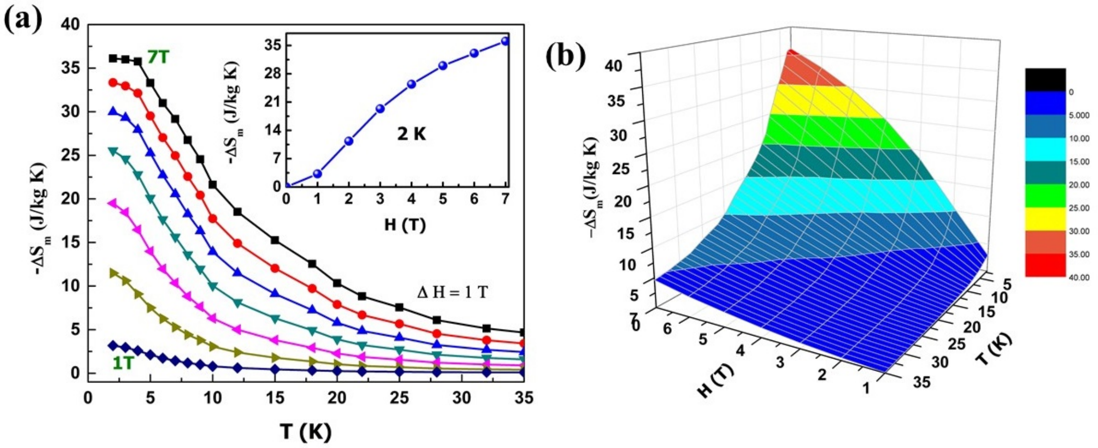

Figure 4.4: (a) The temperature variation of ΔS_m for $GdCrTiO_5$ calculated from the magnetization data and inset shows the field dependence of ΔS_m at 2 K. (b) The contour plot of ΔS_m as functions of temperature and magnetic field for $GdCrTiO_5$.

fields above 5 T. For application, ΔS_m should be reasonably large at low or moderate magnetic field strength. The field dependence of ΔS_m is displayed in the inset of Figure 4.4(a) at 2 K. From the contour plots of ΔS_m with temperature and magnetic field as shown in Figure 4.4(b), one can see that ΔS_m in the low-temperature region is quite large at low field. For example, the values of -ΔS_m at 2 K are 12 and 20 J kg^{-1} K^{-1} for field change of 2 and 3 T, respectively which can be achieved using a permanent magnet. Another remarkable feature of low-field $\Delta S_\mathrm{m}(T)$ curve is that instead of saturation behavior at low temperature, ΔS_m increases with decrease in T ($\mathrm{d}\Delta S_\mathrm{m}/\mathrm{d}T<0$). So, ΔS_m can be significantly large even in the subkelvin region. The saturation-like behavior of ΔS_m down to 2 K is due to the very low AFM transition of $GdCrTiO_5$.

The large magnetocaloric effect in $GdCrTiO_5$ is associated with infinite numbers of degenerate frustrated magnetic ground states. The frustration in the present compound occurs due to the competition between the Dzyaloshinskii-Moriya interaction and the spatial anisotropy exchange interaction which is one of the main characteristics of $R\mathrm{Mn_2O_5}$ series. With application of magnetic field, the degeneracy in the ground state tends to lift and causes the frustrated magnetic moments to polarize in the field direction, as a result, large magnetic entropy change occurs. Theoretical investigation has shown that the enhancement of magnetocaloric effect in frustrated magnet is related to the condensation of soft modes below the saturation field [137]. However, there are very few experimental reports to support such theoretical prediction for large magnetocaloric effect in frustrated systems [136, 138].

4.3.4 Magnetic entropy change of other compounds in the series

To compare the value of the magnetic entropy change of $\mathrm{GdCrTiO_5}$ with the value of the other two compounds in the series $\mathrm{DyCrTiO_5}$ and $\mathrm{HoCrTiO_5}$, we have also calculated the ΔS_{m} with the measured $M(H)$ data as shown in Figure 4.5. The maximum value of the ΔS_{m} has been reached to 14.7 J/kg K for $\mathrm{DyCrTiO_5}$ at 7 K and 7 T as shown in Figure 4.5(a). Whereas for $\mathrm{HoCrTiO_5}$, the maximum value of the ΔS_{m} has been reached to 17.7 J/kg K at 7 K and 7 T as shown in Figure 4.5(b). Therefore there have two major differences of the ΔS_{m} of $\mathrm{GdCrTiO_5}$ and other two studied compounds. The maximum value of ΔS_{m} for Gd-based material is more than double as compared to the other two studied materials in the present series $R\mathrm{CrTiO_5}$. Also the nature of the ΔS_{m} curve for $\mathrm{DyCrTiO_5}$ and $\mathrm{HoCrTiO_5}$ has been decreased below 7 K but for $\mathrm{GdCrTiO_5}$ it does not decrease down to 2 K but a saturation-like behavior appears below 5 K. The value ΔS_{m} should be large in a

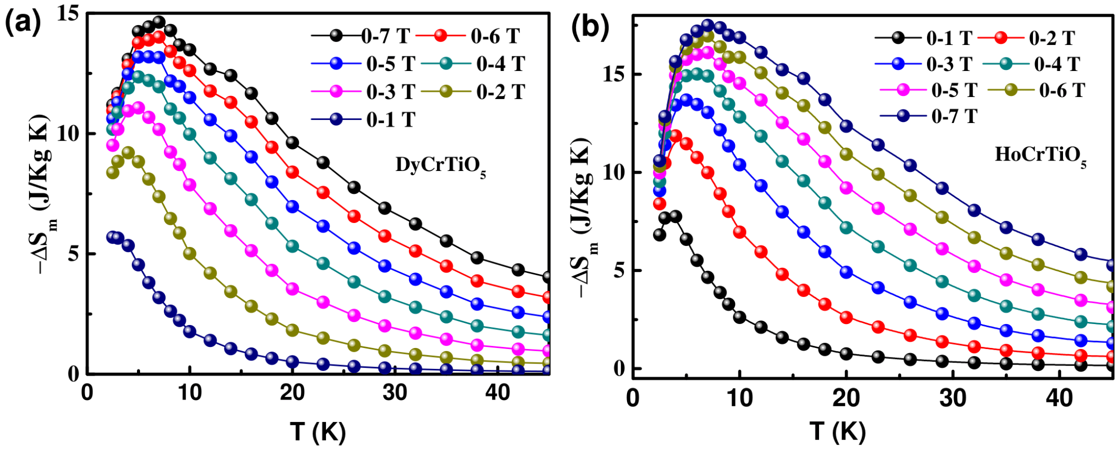

Figure 4.5: (a) The temperature variation of ΔS_m for DyCrTiO$_5$. (b) The temperature variation of ΔS_m for HoCrTiO$_5$ calculated from the magnetization data of chapter 2.

wide range of operating temperature which important for using the MCE material in an application purpose in refrigeration technology. In these respect GdCrTiO$_5$ is superior than DyCrTiO$_5$ and HoCrTiO$_5$.

4.3.5 Mechanical effeciency

For the application perspective, the mechanical efficiency (η) is an important parameter for magnetic refrigeration, if the magnetocaloric effect is driven mechanically using a permanent magnet to generate magnetic field. The heat ($Q = T_0 S_m$) is generated when magnetic field is applied to an isothermal magnetocaloric material at the operating temperature $T_0 = 5$ K. As the direct calorimetric measurement is challenging, Q is calculated using the reported indirect method, i.e., from the temperature dependence of ΔS_m graph. The amount of mechanical work done (W) has been estimated by integrating -MdB using the magnetization data. We have calculated $\eta = \|\mathrm{Q/W}\|$ for GdCrTiO$_5$ and compared with different magne-

Table 4.2: Comparison of magnetic entropy change (ΔS_{m}) and mechanical efficiency (η) of different magnetocaloric materials with respect to $GdCrTiO_5$

Materials	ΔH_0(T)	ΔS_{m}(J kg^{-1} K^{-1})	η(%)	Ref.
$GdCrTiO_5$	2(5)	7.7(25.1)	51(37)	this work
$ErFeO_3$	2(5)	3(12)	47(19)	[133]
$TbCrO_3$	2(5)	4(12)	20(17)	[151]
$HoMnO_3$	2(5)	1(3)	19(18)	[97]
$DyMnO_3$	2(5)	0.2(3.8)	3(2)	[97]
$HoMn_2O_5$	2(5)	1(4)	15(7.4)	[145]
$GdVO_4$	2(5)	0.27(1.06)	44(40)	[150]
$EuDy_2O_4$	2(5)	8(20)	30(20)	[149]
$Er_2Mn_2O_7$	2(5)	1.25(2.24)	7(3)	[152]
Er_2MnTiO_7	2(5)	0.917(2.18)	5(2.9)	[153]

T_0(=5 K), operating temperature; ΔH_0, change in applied magnetic field; data for ΔH_0 = 5 T are presented parenthetically.

tocaloric materials, as shown in Table 4.2 [154]. From the Table 4.2, one can see that the mechanical efficiency of $GdCrTiO_5$ is significantly larger as compared to several magnetic refrigerants in the same temperature and magnetic field range. We would like to mention that the mechanical efficiency of $GdCrTiO_5$ is about an order of magnitude larger than that for several geometrical frustrated systems such as $Er_2Mn_2O_7$ [152].

4.3.6 Heat capacity analysis

In order to understand the nature of magnetic ground state of $GdCrTiO_5$, we have measured the heat capacity. Figures 4.5 (a) and 4.5(b) show the temperature dependence of heat capacity at different applied fields. At zero field, as shown in Figure 4.5(a), initially C_p decreases with decreasing T down to 12 K and then

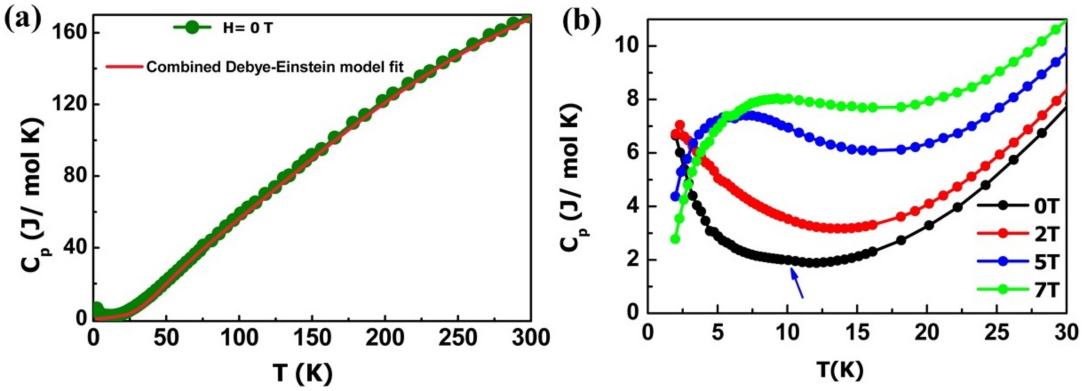

Figure 4.6: (a) The zero-field heat capacity data for $GdCrTiO_5$ compound and the solid line is the combined Debye-Einstein fit. (b) The field dependence of heat capacity for $GdCrTiO_5$. The arrow indicates the short-range ordering of chromium near 10 K.

increases with further decrease in T. No strong anomaly due to the long-range magnetic ordering has been observed within the measured temperature range 1.8-300 K. However, a careful observation reveals an extremely weak anomaly at temperature around 10 K, which is just above our experimental resolution. Similar weak anomaly in C_p has been reported earlier and attributed to short-range ordering [69]. The muon-spin rotation/relaxation study also shows anomaly around 10 K [73]. The nature of anomaly suggests that the transition is very weak and the entropy associated with this transition is negligible. The increase of C_p at low temperature indicates the onset of long-range ordering of Gd^{3+} sublattice below 1.8 K. With the application of magnetic field, the nature of low-temperature $C_p(T)$ curve changes drastically. Up to 2 T, C_p enhances with increase in field strength without showing any peak but a broad peak appears around 7 K at 5 T which shifts further towards higher temperature side as the applied magnetic field is increased from 5 to 7 T.

The zero-field $C_p(T)$ curve can be fitted well with the combined Debye plus Einstein model over a wide temperature range as shown in Figure 4.5(a). At low temperature, however, the fitted curve deviates from the observed experimental data. The lattice heat capacity calculated using the Debye plus Einstein model fitting, was subtracted from the total heat capacity to determine the magnetic contribution (C_m). The magnetic entropy S_m is obtained by integrating $(C_m/T)\mathrm{d}T$. As the AFM transition occurs well below 2 K, we can not determine the magnetic entropy using our heat capacity data for 0 and 2 T fields. However, this is not the case for the $C_p(T)$ curves at 5 and 7 T. For these fields, as the peak in $C_p(T)$ curve appears well above 2 K and the value of C_p is very small at low temperatures, the entropy change can be determined accurately by interpolating the $C_p(T)$ curves between 0 and 2 K using the methods described by others [155]. At high temperature, the entropy is expected to be close to the full saturated value $R\ln(2J+1)$=17.29 J kg^{-1} K^{-1} for the Gd^{3+}. Figure 4.6(a) shows that S_m starts to saturate above 15 K and the saturated value is close to 17.2 J kg^{-1} K^{-1} for both H=5 and 7 T. At high temperatures well above T_N, the saturated value of entropy should nearly be the same for all fields even for the zero magnetic field. Comparing the deduced value of zero-field S_m above 1.8 K with that for 7 T field, we find that at zero field, a significant amount of entropy (10.7 J kg^{-1} K^{-1}) is released below 1.8 K. So, this extra amount was added to the zero-field entropy data to determine S_m for 0 T. For 2 T, the corresponding value is 7.7 J kg^{-1} K^{-1}. As the maximum normalized entropy (S_m)/R is very close to 2, we conclude that a major fraction of 4f spins of Gd^{3+} is taking part in the magnetic ordering. We have also calculated the zero-field magnetic entropy using the reported heat capacity data at low-temperature (0.05-20 K) and observe that the deduced value of S_m is close to that obtained by interpolation which is also shown in the main panel of Figure

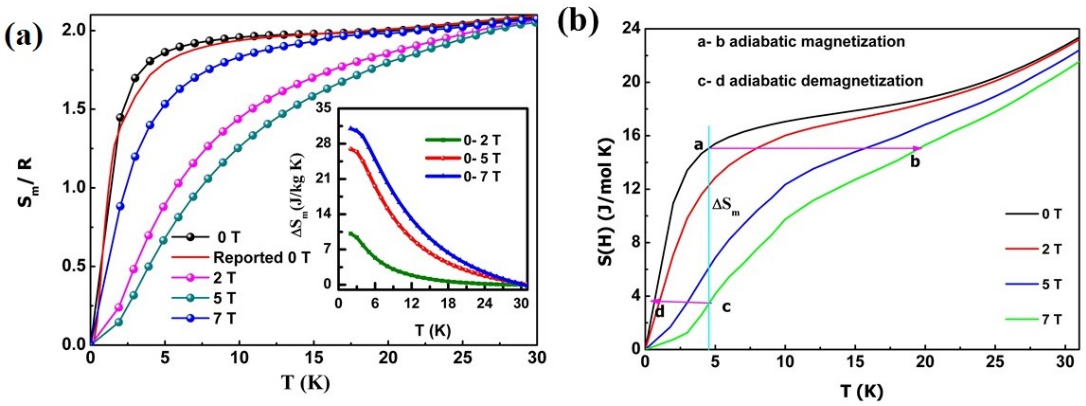

Figure 4.7: The temperature variation of magnetic entropy with field for $GdCrTiO_5$ compound where as the red line represents the zero field entropy calculated from reported data [69] and the inset shows the variation of ΔS_{m} calculated from the heat capacity data. The variation of entropy at different fields. The horizontal arrow from a to b indicates the adiabatic heating and c to d indicates the adiabatic cooling. Whereas the vertical arrow indicates the isothermal entropy change for the magnetic field change 0-7 T.

4.6(a) [69].

4.3.7 ΔS_{m} calculated from heat capacity

To check the consistency in our results on magnetic entropy change estimated from $M(H)$ data, ΔS_{m} has also been calculated independently from the field dependence of heat capacity using the relation

$$\Delta S_m = \int_0^T \frac{[C_p(H_2,T) - C_p(H_1,T)]}{T}\, dT \tag{4.2}$$

where $C_p(H,T)$ is the specific heat at a field H. ΔS_{m} as calculated from the heat capacity data is shown in the inset of Figure 4.6(a) for different fields as a function of temperature. To calculate ΔS_{m}, we have used the reported low-temperature

$C_p(T)$ data at zero field [69]. The calculated values of ΔS_m are very close to that estimated from our zero field $C_p(T)$ curve. It is clear from the plots that the values of ΔS_m estimated from the heat capacity data are close to that calculated from magnetization. For an example, the calculated value of $\Delta S_\mathrm{m}^{max}$ from magnetization is 30 J kg^{-1} K^{-1} whereas that from the heat capacity data is 28.4 J kg^{-1} K^{-1} for the same field change 0-5 T. The small difference in the value of $\Delta S_\mathrm{m}^{max}$ may be due to the underestimation of the magnetic heat capacity.

4.3.8 Adiabatic temperature changes ΔT_ad

Another very important parameter related to magnetic refrigeration is ΔT_ad which is the isentropic temperature difference between $S(H,T)$ and $S(0,\ T)$. For this, we have calculated the entropy $S(H,T)$ at field H after subtracting $\Delta S_\mathrm{m}(H,T)$ determined using the heat capacity data, from the zero-field entropy $S(0,T)$. The temperature variation of entropy at different fields has been shown in Figure 4.6(b). Figure 4.7(a) shows the temperature dependence of ΔT_ad. The maximum value of ΔT_ad reaches as high as 15.5 K at 7 T. Thus, both ΔS_m and ΔT_ad are large for GdCrTiO$_5$. Similar to ΔS_m, ΔT_ad is also quite large at low and moderate field strength. However, there is an asymmetry in the $\Delta T_\mathrm{ad}(T)$ curve about 12 K, when applying a field adiabatically (ΔT_ad heating) and removing the field adiabatically (ΔT_ad cooling). The entropy increases rapidly in zero applied field but increases at a slower rate in presence of magnetic field. So, to interpret the deduced values of adiabatic temperature change, in Figure 4.6(b), we have shown the actual heating (a to b arrow) and cooling (c to d arrow) effects due to adiabatic magnetization and adiabatic demagnetization, respectively. These two processes explain the difference

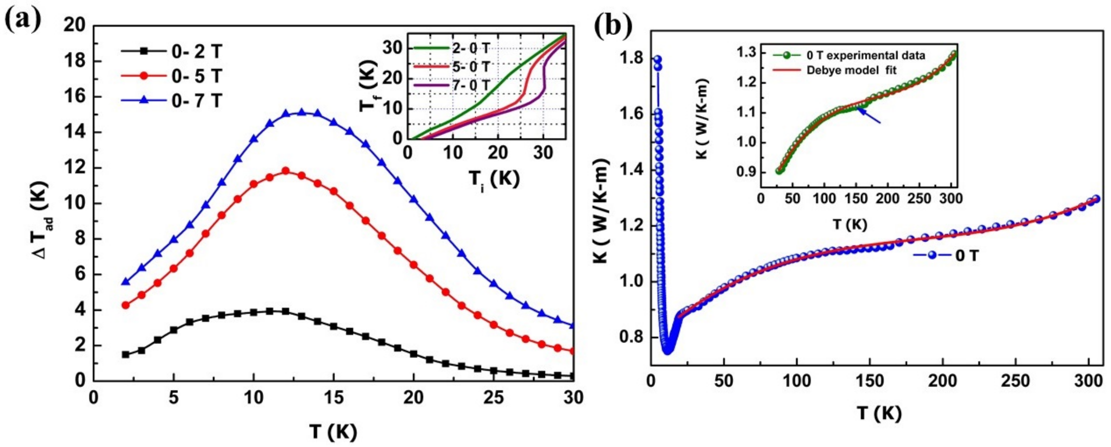

Figure 4.8: (a) The main panel shows the temperature dependence of ΔT_{ad} for GdCrTiO$_5$ at different magnetic fields and the inset shows final temperature T$_f$ as a function of initial temperature T$_i$ in the adiabatic demagnetization process for different magnetic fields. (b) The main panel shows the temperature dependence of thermal conductivity for GdCrTiO$_5$ and the inset shows the Debye-fitting to the experimental data where the arrow indicates the anomaly near 150 K.

between cooling and heating cycles in the magnetocaloric effect of GdCrTiO$_5$.

The cooling effect due to the adiabatic removal of magnetic field can be realized from the inset of Figure 4.7(a). The final temperature (T_f) can be reached by an adiabatic demagnetization from an initial temperature T_i, as presented pictorially in the inset of Figure 4.7(a). For an example, if the sample is initially at 30 K and magnetized by 7 T, decreasing the magnetic field adiabatically to zero causes the sample temperature to drop at 16 K. The lower the T_i, the lower is the T_f. Similarly, the adiabatic removal of magnetic field from 7 to 0 T at initial temperature T_i=20(5 K) leads to T_f=8(0.12 K). So, the present magnetocaloric material GdCrTiO$_5$ can be a good potential material for low temperature magnetic refrigerant.

4.3.9 Thermal conductivity $\kappa(T)$

For magnetic refrigeration, the used material should have reasonably high thermal conductivity (κ) for fast heat exchange and very high electrical resistivity to avoid any loss due to the eddy current. For this reason, we have measured the thermal conductivity of the studied material $GdCrTiO_5$ in absence magnetic field. The main panel of Figure 4.7(b) shows the temperature dependence of κ in the range 4-300 K. κ decreases very slowly with decrease in temperature down to 18 K and shows a deep around 11 K. Below 11 K, κ increases sharply and reaches as high as 1.8 W K^{-1} m^{-1} at 4 K. This behavior of κ is very similar to heat capacity and indicates a magnetic origin. The experimental data above 18 K can be fitted well with the Debye model. In several rare-earth transition metal oxides, κ starts to increase as temperature decreases and approaches towards AFM transition of R^{3+} sublattice, where the phonon contribution becomes less important. The increase of κ with decrease in T at low temperature has been attributed to the suppression of spin-phonon scattering [156, 157, 158, 159, 160, 161]. Besides phonon, magnon can also contribute to thermal conductivity at low temperature. From the inset of Figure 4.7(b), it is clear that thermal conductivity shows a weak anomaly near 150 K where the magnetic susceptibility, magnetodielectric and Raman scattering showed a change. Thermal conductivity measurements with magnetic field down to very low temperature on single-crystalline samples will be useful for understanding the role of different scattering mechanisms. In the context of magnetocaloric effect, we would like to mention that the observed value of thermal conductivity of $GdCrTiO_5$ is comparable with that reported for several low-temperature magnetic refrigerants [161, 162, 163].

4.4 Summary and conclusion

In summary, we have studied the magnetocaloric properties of $GdCrTiO_5$ through magnetization, heat capacity and thermal conductivity measurements. In $GdCrTiO_5$, magnetocaloric parameters are quite large. The maximum values of isothermal entropy change and adiabatic temperature change are 36 J kg^{-1} K^{-1} and 15.5 K, respectively at 7 T. This compound also demonstrates a remarkable magnetocaloric effect even at low and intermediate applied fields. Unlike several potential low-temperature magnetic refrigerants, ΔS_{m} in the present compound does not decrease at low temperature and efficiency is very high due to very low AFM transition of Gd^{3+} sublattice. Our result suggests that $GdCrTiO_5$ could be a potential material for magnetic refrigeration at low temperature.

5

Giant reversible magnetocaloric effect in multiferroic $GdFeO_3$ single crystal

5.1 Introduction

Primarily, the investigation on MCE has been focused on searching new materials that exhibit large entropy and adiabatic temperature change close to room temperature for the domestic and industrial applications [109, 110, 111, 112, 113, 114]. On the contrary, magnetic refrigeration in the low-temperature region has been much less focused. Low-temperature magnetic refrigeration also has several important applications as we have mentioned in chapters 1 and 4. Several rare-earth transition metal oxides and intermetallic compounds become attractive candidates for the low-temperature magnetic refrigeration [97, 130, 131, 132, 133, 134, 135]. In these materials, the rare-earth magnetic moment orders antiferromagnetically at low temperature. With the application of magnetic field, the AFM transition (T_N) suppresses and the magnetic entropy decreases considerably in the vicinity of T_N.

However, the value of magnetic entropy change decreases rapidly at low temperature. As a result, ΔS_{m} becomes very small just few Kelvin below the transition temperature. This is one of the major problems for the refrigeration at low temperature using a magnetically ordered material. In recent past, it has been shown that several rare-earth transition metal based frustrated magnetic systems such as $R\mathrm{MnO_3}$, $\mathrm{HoMn_2O_5}$, etc. exhibit large MCE at low temperature [97, 149, 164]. However, both ΔS_{m} and ΔT_{ad} show a strong decrease below the ordering temperature of the rare-earth moment.

$R\mathrm{FeO_3}$-type system has received considerable attention because it exhibits several complex and interesting phenomena like spin-flop transition, spin-reorientation transition, multiferroicity, anistropic magnetocaloric effect, etc. associated with the three different types of intriguing magnetic interactions R-R, R-Fe, and Fe-Fe [133, 134, 165, 166, 167, 168, 169, 170, 171, 172]. There are few reports on magnetic and structural properties of $\mathrm{GdFeO_3}$ [173, 174, 175]. However, the details isothermal magnetization up to high magnetic field, the field dependence of compensation temperature and magnetocaloric effect in $\mathrm{GdFeO_3}$ have not been studied so far.

In the present work, we have successfully grown high quality single crystal of $\mathrm{GdFeO_3}$ using the floating zone technique and investigated its magnetic and magnetocaloric properties. We have chosen $\mathrm{GdFeO_3}$ as a refrigerant material mainly due to the large angular momentum of the localized 4f shell electrons of $\mathrm{Gd^{3+}}(J=7/2)$. Apart from this, in $\mathrm{GdFeO_3}$, magnetization shows no thermal and field hysteresis and the electrical conductivity is very low which prevents the eddy current loss in presence of magnetic field. Besides large magnetic entropy change, the frequency of refrigeration cycle is another important parameter for the magnetic cooling. Though, $\mathrm{GdFeO_3}$ is insulating, it shows good thermal conductivity due to the lattice contribution which helps for faster heat exchange during the refrigeration cycle [176]. In $GdFeO_3$, the Fe spin orders antiferromagnetically around T_{N}^{Fe} ~678 K and the nonlinear canted G-type AFM ordering of the Fe sublattice gives rise to a weak ferromagnetism due to the Dzyaloshinskii-Moriya (DM) interaction [177]. The Gd moments also order antiferromagnetically but at a relatively low temperature 2.5 K [177, 178]. Due to the asymmetric nature of the DM interaction, the Fe^{3+} spins order antiferromagnetically along the crystallographic a axis and the Gd^{3+} spins order along the b axis [165, 179].

Our study reveals that both ΔS_{m} and ΔT_{ad} are very large over a wide temperature range and ΔS_{m} is almost temperature independent below 5 K. This behavior of $GdFeO_3$ is very different from that observed in several magnetically ordered systems and rare-earth ortho-ferrites [130, 131, 132, 133, 134]. The values of the magnetocaloric parameters are also quite large for low or moderate field strength.

5.2 Sample preparation and experimental details

Polycrystalline $GdFeO_3$ sample was prepared by conventional solid-state reaction method using high purity Gd_2O_3 (99.9%) and Fe_2O_3 (99.9%) powder. Before use, Gd_2O_3 was heated at 900 °C for 12 h to remove any adsorbed water and CO_2. The well-mixed powder of Gd_2O_3 and Fe_2O_3 in a stoichiometric ratio 1:1 was heated at 1150 °C for few days with intermediate grindings. The polycrystalline $GdFeO_3$ sample was then reground and pressed into two rods of 6 mm in diameter under hydrostatic pressure. Finally, the rods were sintered at 1400 °C for 24 h in air. The single crystal of $GdFeO_3$ was grown in a four-mirror image furnace (Crystal System Inc.) Special attention was paid to achieve the oxygen stoichiometry close

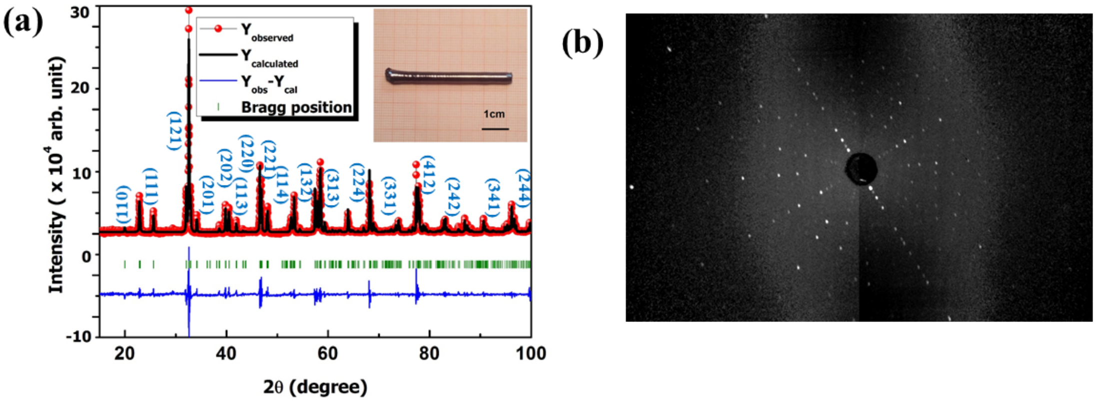

Figure 5.1: (a) The x-ray diffraction pattern of the powdered single crystal of $GdFeO_3$ grown in a floating zone image furnace and the he inset shows the optical image of the grown crystal. (b) The Laue diffraction pattern of $GdFeO_3$ single crystal along c axis.

to 3. For this reason, the crystal was grown in oxygen atmosphere with a typical growth rate 4 mm/h. During the growth, the feed and seed rods were rotated in opposite directions at a speed of 25 rpm. The phase purity and the crystal structure of the grown single crystal have been determined by high-resolution x-ray powder diffractometer. For the structural analysis, the Rietveld refinement of the diffraction pattern of the powdered $GdFeO_3$ single crystal was done using with the Fullprof software. The experimental x-ray intensity profile with the theoretical fit are shown in Figure 5.1(a). The vertical lines correspond to the Bragg positions in the Figure 5.1(a). All the peaks in the diffraction pattern can be indexed well with the distorted orthorhombic unit cell having Pbnm crystallographic symmetry. The lattice parameters determined from the Rietveld profile analysis are a=5.3460, b=5.5879, and c=7.6680 Å, which are very close to the previously reported values [175, 177]. As grown single crystal has been shown in the inset of Figure 5.1(a). We have also characterized the sample by the Laue diffraction technique and observed very sharp Laue diffraction spots which is displayed in Figure 5.1(b) along

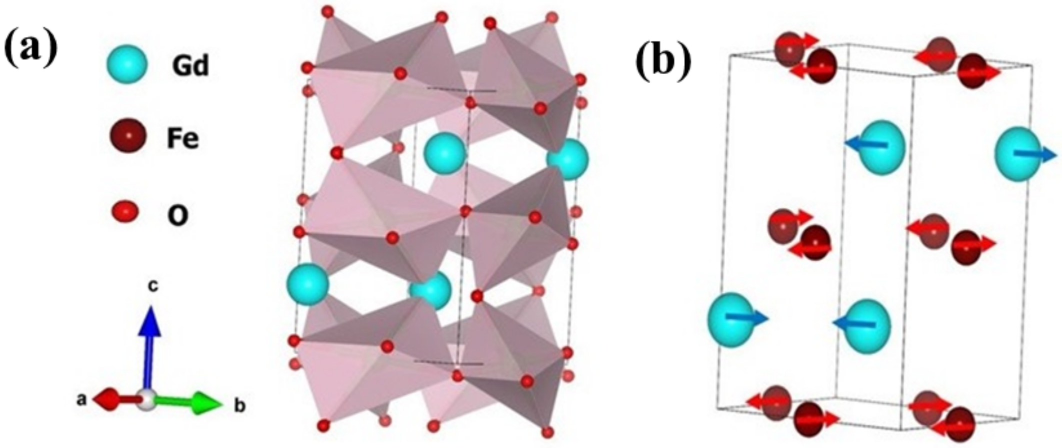

Figure 5.2: (a) The orthorombic crystal structure of $GdFeO_3$ single crystal and (b) the magnetic structure of $GdFeO_3$ single crystal below the antiferromagnetic ordering temperature of Gd. The arrows represent the direction of magnetic moment of Gd and Fe.

c direction. This suggests good crystalline quality of the studied sample. The crystallographic structure of $GdFeO_3$ is shown in Figure 5.2(a) and the approximate magnetic structure has been shown in Figure 5.2(b). The Gd^{3+} spins order along the orthorhombic **b** axis. Though the direction of Fe^{3+} spin alignment is **a** axis, a small zero-field moment is expected along the longest **c** axis due to the DM interaction. The complexity in spin structure due to the DM interaction has not been portrayed in the figure. The details of the spin orientation will be discussed in the results and discussion section.

A small piece of single crystal was used for the heat capacity (C_p) measurements, which were performed in a PPMS (Quantum design). Magnetic measurements were done both in a PPMS and SQUID-VSM (Quantum design). The magnetization measurements for high temperature has been done in a high T VSM set up. To minimize the demagnetization effect, we have used a long parallelepiped sample and the field was applied along the longer dimension which is c axis. Data have been recorded for the isothermal dc magnetization measurement with field up to 9 T at different temperatures between 2 and 36 K, and the temperature dependence of magnetization was measured in the range 2-300 K. The heat capacity has been measured by the relaxation technique at different applied fields (0-8 T) along c axis.

5.3 Results and discussion

5.3.1 Temperature dependence magnetization

The magnetization of $GdFeO_3$ single crystal has been measured as a function of temperature for two temperature regions 540-740 K and 2-300 K under field-cooled condition with field along c axis. The Fe^{3+} spins show canted AFM ordering at T_N^{Fe}~715 K as shown in Figure 5.2(a). The main panel of Figure 5.2(b) shows $M(T)$ curves for two applied fields, 100 and 500 Oe, as representatives. The expanded view of the $M(T)$ curves in the low-temperature region is shown in the inset of Figure 5.2(b) for different applied fields below 500 Oe. It is clear from the figure that the nature of $M(T)$ curve at low field is very complex due to the strong competition between 3d moment of Fe^{3+} and 4f moment of Gd^{3+} [91, 177]. Below T_{N}^{Fe}, the Fe spin shows a canted G-type AFM ordering, due to the antisymmetric nature of the DM exchange interaction between the Fe moments, which prefers interacting spins to align themselves perpendicular to each other. As a result, a weak ferromagnetic-like component is observed at low temperature below T_{N}^{Fe}. Furthermore, the antisymmetric exchange interaction or the pseudo dipolar interaction between the Gd and Fe moments produces an effective magnetic

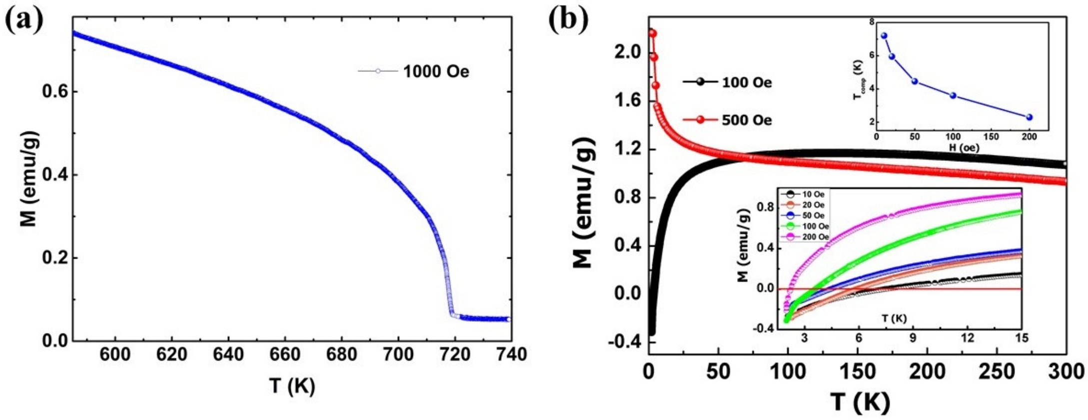

Figure 5.3: (a) The temperature dependence of magnetization at 1000 Oe for the temperature range 540-740 K and (b) $M(T)$ at 100 Oe and 500 Oe for the temperature range 2-300K and the lower inset shows the variation of magnetization for the some fields at low temperature regime and the upper inset shows the variation of compensation temperature with magnetic field for GdFeO$_3$ single crystal .

field at the Gd^{3+} site, whose direction is opposite to the canted Fe^{3+} moment. This internal field (H_I) is attributed to the higher-order anisotropic exchange interaction [177]. One can see that M becomes negative at low temperature for applied field H≤200 Oe. The temperature, T_{comp}, below which M becomes negative is sensitive to the field strength. T_{comp} decreases from 7.3 to 2.2 K as the strength of field increases from 10 to 200 Oe. At around T_{comp}, the moments of the two sublattices become equal in magnitude but opposite in direction, as a result, the net resultant moment is very close to zero. This is known as the compensation temperature [177]. Below T_{comp}, the net magnetic moment aligns in the opposite direction to the applied magnetic field and hence M becomes negative. At higher temperature well above T_{comp}, where the Fe^{3+} moment dominates over Gd^{3+}, M is positive and decreases very slowly with increasing temperature. Several features manifested in the low-field $M(T)$ curves progressively weaken with increasing field strength and disappear above a certain field. For example, M at H=500 Oe is positive, increases monotonically with decrease in T and shows no anomalous behavior in the measured temperature range 2-300 K. From the T_{comp} versus H plot, we have estimated the value of critical field $H_c \sim$ 350 Oe above which the sign reversal phenomenon disappears. It may be noted that this value of H_c is very close to the internal magnetic field produced by the Fe^{3+} sublattice at the Gd^{3+} site [91, 177]. The magnetization reversal phenomenon has also been observed in other ortho-ferrites (RFeO$_3$) and in several AFM perovskites such as orthochromites, orthovanadates, and manganites [166, 180, 181, 182, 183]. T_{comp} for $GdFeO_3$ is comparable to that reported for $NdFeO_3$ ortho-ferrite [165]. On the other hand, T_{comp} and H_I are as high as 130 K and 5.5 kOe, respectively for $GdCrO_3$ [184].

5.3.2 Isothermal magnetization and Arrott plot

In order to understand the evolution of magnetization in $GdFeO_3$ single crystal with the application of magnetic field, we have measured the isothermal magnetization up to 9 T at different temperatures. The magnetic field dependence of magnetization along c axis is shown in Figure 5.3(a) for some selected temperatures. It is clear from Figure 5.3(a) that even at low field, M increases monotonically with the decrease in T as in the case of a typical ferromagnet. This behavior of M is very different from the expected field-induced metamagnetic transition in a simple AFM. Usually, for AFM systems, M exhibits nonmonotonic temperature dependence in the low-temperature and low-field region [130, 131, 132, 133]. At 2 K and 9 T, the value of magnetic moment is about 7.2 μ_B/Gd which is 3% higher than the spin only moment of Gd (7 μ_B/Gd). This indicates some contribution from the Fe sublattice.

The smooth evolution of M with H indicates that the field-induced transition

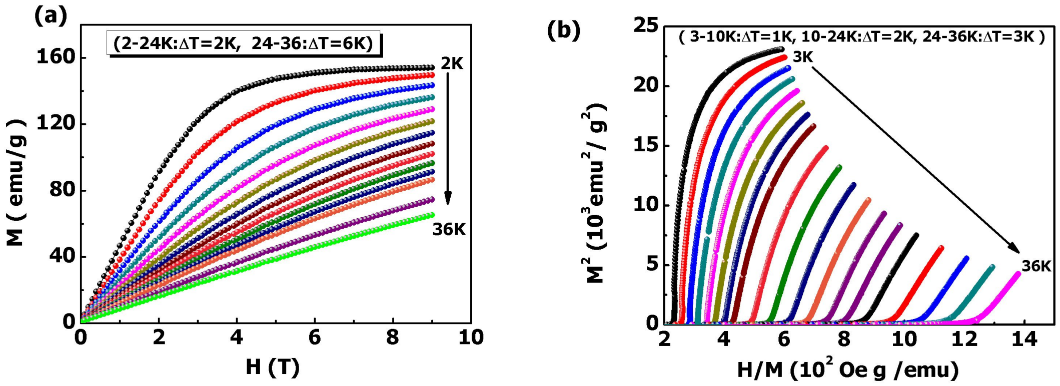

Figure 5.4: (a) Some representative isothermal magnetization plots are shown for $GdFeO_3$ single crystal in the temperature range of 2-36K and (b) the Arrott plots for the $GdFeO_3$ single crystal crystal.

is second order in nature. To determine the exact nature of the field-induced magnetic phase transition, the $M(H)$ curves have been transformed into the well-known Arrott plots. Figure 5.3(b) shows M^2 versus H/M plots for the $GdFeO_3$ single crystal. The slope of M^2 versus H/M curve is useful to determine the order of both temperature and field driven magnetic phase transition. The negative slope of the Arrott plot often indicates a first-order nature of the transition, while the positive slope implies a second-order transition. The positive slope of the M^2 versus H/M curves suggests that the field-induced phase transition in $GdFeO_3$ single crystal is second-order continuous in nature.

Field-dependent magnetization along different crystalographic directions has been investigated in single crystals of several $R\mathrm{FeO_3}$ (R=Dy, Er, Tb, Ho, Tm) compounds [130, 131, 132, 133, 134]. In all the cases, M shows strong anisotropy. Both the value of M and the nature of $M(H)$ curve are extremely sensitive to direction of applied field. For example, the values of M for $DyFeO_3$ at 2 K and 7 T are 4.4, 7.8 and 0.8 μ_B/Dy along a, b and c axis, respectively which correspond to only 44, 78 and 80% of the expected moment of Dy^{3+} [131]. Also, the nature of

$M(H)$ curve changes dramatically with the field direction. Along the easy axis, M increases abruptly and tends to saturate at a relatively small applied field while for the hard axis M increases almost linearly with field. We have also measured M with field along a and b axis in $GdFeO_3$. In all three crystallographic directions, the value of M at 9 T and 2 K is large and close to the expected moment for Gd^{3+} ion and the H dependence of M is found to be very similar to Figure 5.3(a). This suggests that the field response of M in $GdFeO_3$ is very different from that reported for other ortho-ferrites. The observed differences in magnetic properties of $GdFeO_3$ and other ortho-ferrites are due to the magnetocrystalline anisotropy which arises from the spin state of RE ion. Gd^{3+} is unique among the rare-earth elements. The Gd^{3+} ion has no orbital angular momentum (L=0) contribution to the total angular momentum (J). Only spin angular momentum (S=7/2) contributes to J. So, the crystal field effect which is responsible for magnetocrystalline anisotropy is negligible in $GdFeO_3$ compound and as a result, magnetization is expected to be almost isotropic and large [185, 186].

5.3.3 Magnetic entropy change

The large field-induced magnetization in $GdFeO_3$ single crystal gives an indication on giant magnetic entropy change. To test whether this material is suitable for the magnetic refrigeration, we have calculated the magnetic entropy change using the Maxwell equation, $\Delta S_m = \int_0^H (dM/dT)dH$. As the magnetization measurements are done at discrete field and temperature intervals, ΔS_m is numerically calculated

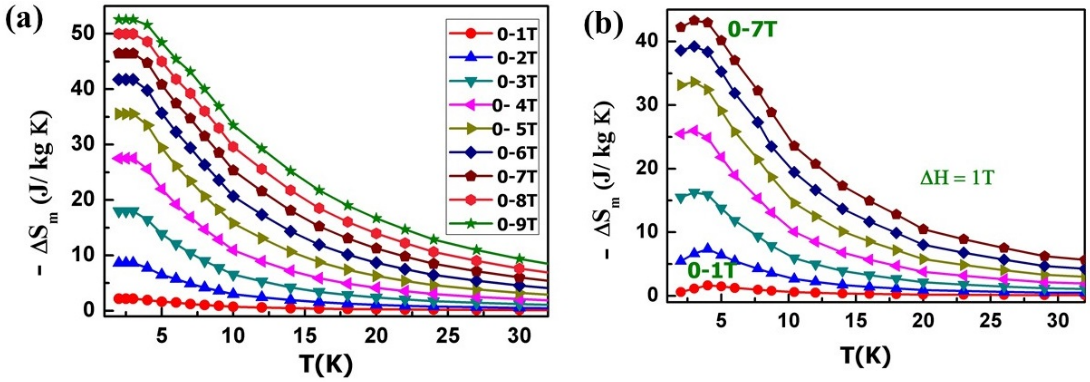

Figure 5.5: The temperature variation of ΔS_m calculated from the magnetization data for $GdFeO_3$ (a) single crystal (b) polycrystalline.

using the following expression,

$$\Delta S_\mathrm{m} = \sum_i \frac{M_{i+1} - M_i}{T_{i+1} - T_i} \Delta H_i \tag{5.1}$$

where M_i and M_{i+1} are the magnetic moments at temperatures T_i and T_{i+1}, respectively for a small change in magnetic field ΔH_i. The temperature dependence of ΔS_m has been deduced from the magnetic field dependence of the magnetization using the above relation. Figure 5.4(a) presents the temperature dependence of ΔS_m for the field variation up to 9 T. It is very clear from the figure that ΔS_m is very large and negative down to the lowest measured temperature. The maximum value of ΔS_m ($\Delta S_\mathrm{m}^{max}$) increases with the increase in field and reaches as high as 52.5 J/kg K for the field change of 0-9 T, which is more than double of the reported values of ΔS_m for other members of the ortho-ferrite series [133, 134, 131, 130, 132]. This difference in magnetocaloric properties arises mainly due to the magnetocrystalline anisotropy of the rare-earth ions.

We would also like to mention that the observed value of ΔS_m is significantly larger than that reported for several rare-earth transition metal oxides and intermetallic compounds [121, 122, 123, 124]. Apart from the value, the nature of temperature dependence of ΔS_m is also very important for the application in low-temperature refrigeration. We have already mentioned that ΔS_m in a typical ferromagnet or antiferromagnet shows a sharp decrease at low temperature due to the onset of long-range magnetic ordering. For examples, the Gd sublattice in $GdVO_4$ and $RuSr_2GdCu_2O_8$ also orders antiferromagnetically at 2.5 K but ΔS_m in these systems decreases rapidly below 5 K and becomes very small and even changes its sign [147, 150]. On the other hand, in the present system, ΔS_m does not show any decrease down to 2 K but a saturation-like behavior appears below 5 K. For application, ΔS_m should have reasonably large value at low or moderate magnetic field strength. From Figure 5.4(a), one can see that ΔS_m is quite large even at low field. For example, the values of $\Delta S_\mathrm{m}^{max}$ are 9 and 18 J/kg K for the field change of 2 and 3 T, respectively which can be achieved using a permanent magnet.

From the application point of view, it is important to investigate the magnetocaloric properties for the polycrystalline sample. The temperature dependence of ΔS_m has been shown in Figure 5.4(b) for the $GdFeO_3$ polycrystalline sample. The value of ΔS_m for the polycrystalline sample is also very large. $\Delta S_\mathrm{m}^{max}$ is 44 J/kg K at 7 T which is about 4% smaller than the corresponding value at 7 T for the single crystal. However, the nature of $\Delta S_\mathrm{m}(T)$ curve for the polycrystalline sample is slightly different. With the decrease in temperature, ΔS_m increases up to about 3-4 K and then decreases. Though ΔS_m decreases at low temperature, the decrease is very slow as compared to several other low-temperature magnetic refrigerant including ortho-ferrites. This suggests polycrystalline $GdFeO_3$ can also be considered for the magnetic refrigeration. Though the observed giant MCE in

Table 5.1: Comparison of electrical and mechanical efficiency of different magnetocaloric materials with respect to $GdFeO_3$

Parameters	$GdFeO_3$	$DyMnO_3$	$GdVO_4$	$EuDy_2O_4$	$HoMn_2O_5$
$T_0(K)$	5	5	5	5	5
$\mu_0\Delta H_0$(T)	2(5)	2(5)	2(5)	2(5)	2(5)
Q (J cm^{-3})	0.28(1.06)	0.03(0.12)	0.25(1.06)	0.31(0.83)	0.053(0.134)
Electrical Work (J cm^{-3})	2.04(12)	2.54(12.31)	2.13(12.40)	2.83(14.88)	1.18(11)
Electrical Efficiency (%)	14(9)	1.20(1)	11(8)	10(5)	3(1.2)
Mechanical Work (J cm^{-3})	0.49(2.74)	1.01(4.8)	0.56(2.60)	1.10(4.10)	0.358(1.8)
Mechanical Efficiency (%)	57(39)	3(2)	44(40)	30(20)	15(7.4)
Reference	This work	[97]	[150]	[94]	[164]

T_0, operating temperature; $\mu_0\Delta H_0$, change in applied magnetic field; μ_0, permeability of free space; Q, heat; W, work; effeciency = [Q/W]. Data for $\mu_0\Delta H_0$ = 5 T are presented parenthetically.

$GdFeO_3$ is mainly due to the high moment of Gd^{3+}, much weaker crystal field effect also plays an important role.

5.3.4 Mechanical effeciency

How much work is done during the reversible thermal changes in the materials themselves is an important parameter for the application purpose [154]. For this, the energy efficiency for the $GdFeO_3$ single crystal has been calculated and compared with other low-temperature magnetic refrigerants. The amount of heat (Q) released during the isothermal process has been deduced using the relation $Q = T_0 S_m$, where T_0 is the operating temperature. We have also estimated the required amount of mechanical work (W_m) or electrical work (W_e) to drive the reversible caloric effects using the method described by Moya et al. [154]. As the value of Q is very sensitive to T , we have used $T_0 = 5$ K, around which $S_m(T)$ exhibits a maximum. Using these parameters, both mechanical efficiency (η_m) and electrical efficiency (η_e) are calculated for the $GdFeO_3$ single crystal and other systems from the reported data. For comparison, η_m and η_e are shown in Table I. It is clear from the table that both η_m and η_e are higher for $GdFeO_3$ as compared to manganites, vanadates, and RR_2O_4-type compounds, which also exhibit large MCE. We have also calculated η_m and η_e at 2 K, i.e., below the liquid helium temperature and at the liquid hydrogen temperature, 20 K. The values of η_m at 2 T are 18.3% and 118% at 2 and 20 K, respectively, and the corresponding values of η_e are 6% and 13%. At low temperature below T_0, Q decreases rapidly due to the decrease of both T and S_m. As S_m for $GdFeO_3$ is almost temperature independent down to 2 K, the decrease in Q is due to the decrease of T only. As a result, its efficiencyis

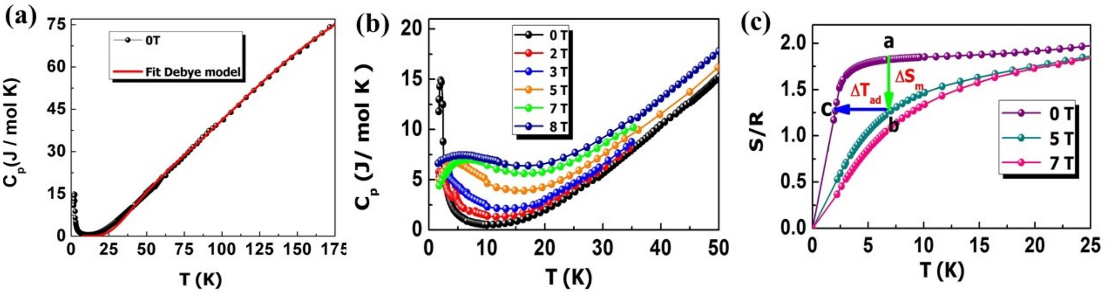

Figure 5.6: (a) Temperature dependence of zero-field heat capacity. The solid line is the Debye model fit to the experimental data of $GdFeO_3$ single crystal. (b) The temperature dependence of heat capacity for $GdFeO_3$ single crystal at different magnetic fields. (c) The temperature dependence of magnetic entropy of $GdFeO_3$ single crystal due to the ordering of Gd sublattice obtained from heat capacity data. The vertical arrow shows the isothermal magnetization ΔS_{m} for the magnetic field change (0-5T) and a to d and b to c represent cooling and heating effects respectively in adiabatic demagnetization and adiabatic magnetization at the 6K, for a change of 5 T magnetic field as an example.

expected to be higher compared to other systems.

5.3.5 Heat capacity of analysis

For better understanding the nature of the magnetic and magnetocaloric properties, we have also measured the heat capacity of the $GdFeO_3$ single crystal. At zero field, C_p decreases with the decrease in temperature down to 10 K and then increases with further decrease in temperature and exhibits a prominent λ-like anomaly at around 2.5 K; indicating a paramagnetic to AFM transition of Gd sublattice. To calculate the lattice heat capacity, the zero-field $C_p(T)$ curve in the high-temperature region has been fitted using the Debye model as shown by the solid line in Figure 5.5(a). With the application of field, the peak broadens due to the Schottky effect and shifts toward higher temperature. Qualitatively, similar behavior has been observed in $Gd(HCOO)_3$ which also exhibits large MCE at low temperature [135]. The temperature dependence of C_p for different applied fields is shown in Figure 5.5(b). The obtained lattice part was subtracted from the total heat capacity to determine the magnetic contribution (C_m) to the heat capacity and hence the entropy (S_m) associated with the AFM ordering at 2.5 K. S_m is obtained by integrating $(C_m/T)\mathrm{d}T$ and shown in Figure 5.5(c). At zero field, the estimated saturation value of S_m is 17.3 J/mol K which is very close to that expected for the Gd^{3+}. It may be further noted that more than 85% of the magnetic entropy is released just below the AFM transition. This suggests that a major fraction of 4f spins is taking part in the magnetic ordering. However, the magnetic entropy shifts rapidly toward higher temperature side with the application of magnetic field.

5.3.6 ΔS_m calculated from heat capacity

To check the consistency in our results on magnetic entropy change estimated from $M(H)$ data, ΔS_m has also been calculated independently from the field dependence of heat capacity using the relation

$$\Delta S_m = \int_0^T \frac{[C_p(H_2,T) - C_p(H_1,T)]}{T}\,dT \tag{5.2}$$

where $C_p(H,T)$ is the specific heat at a field H. ΔS_m as calculated from the heat capacity data is shown in Figure 5.6(a) as a function of temperature. It is clear from the plots that the values of ΔS_m calculated from the magnetization and heat capacity data are close to each other.

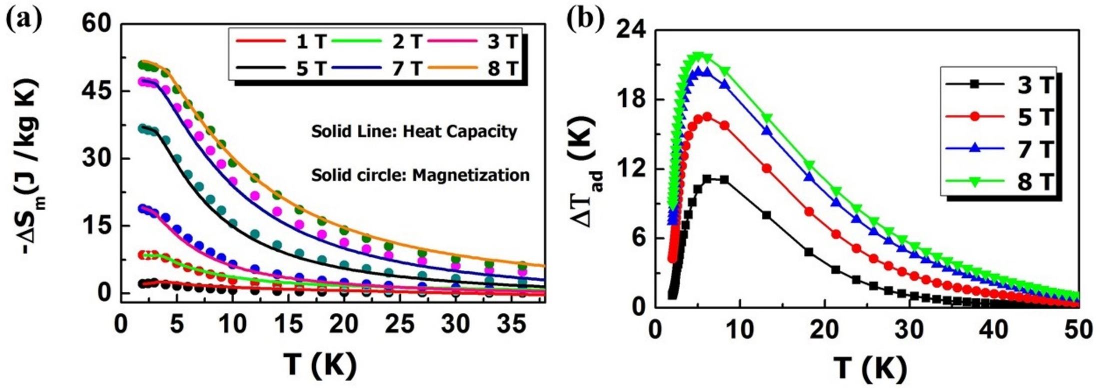

Figure 5.7: (a) Comparison between ΔS_{m} calculated from magnetization and that calculated from heat capacity data in $GdFeO_3$. (b) The temperature dependence of ΔT_{ad} for $GdFeO_3$ single crystal.

5.3.7 Adiabatic temperature changes ΔT_{ad}

It has already been mentioned that another very important parameter related to the magnetic refrigeration is ΔT_{ad} which is the isentropic temperature difference between $S(H,T)$ and $S(0,\,T)$. ΔT_{ad} can be calculated from the zero-field $C_p(T)$ and $\Delta S_{\mathrm{m}}(H,T)$ data. For this, we have calculated the entropy $S(H,T)$ at field H after subtracting $\Delta S_{\mathrm{m}}(H,T)$ determined using the heat capacity data, from the zero-field entropy $S(0,T)$. The temperature dependence of ΔT_{ad} is shown in Figure 5.6(b). The maximum value of ΔT_{ad} reaches as high as 22 K at 8 T and 6 K. Thus, both ΔS_{m} and ΔT_{ad} are very large in $GdFeO_3$ ortho-ferrite. Similar to ΔS_{m}, ΔT_{ad} is also quite large at low and moderate field strength. We would like to mention that these magnetocaloric parameters have reasonably good values close to 20 K, the boiling point of hydrogen. In this context, it may be noted that undoped and doped $EuTiO_3$, $EuDy_2O_4$ and $GdVO_4$ exhibit huge MCE at low temperature [74, 148, 149, 150, 187]. The values of $\Delta S_{\mathrm{m}}^{max}$ in these compounds are also comparable to the present system. However, $\Delta S_{\mathrm{m}}(T)$ shows a strong decrease in the low-temperature region. In magnetic refrigeration, ΔS_{m} per unit volume is important. As the density of the studied material (7.4 g cm^{-3}) is high, the value of ΔS_{m} per unit volume for $GdFeO_3$ is also quite large.

5.4 Summary

In summary, we have studied the magnetocaloric properties of single crystalline $GdFeO_3$ sample through magnetization and heat capacity measurements. The maximum values of the adiabatic temperature change and isothermal entropy change are as high as 22 K at 8 T and 52.5 J/kg K at 9 T, respectively. The isothermal entropy change calculated from magnetization data for polycrystalline sample is also very high. This compound also demonstrates a remarkable magnetocaloric effect even at low and intermediate applied fields. Unlike several potential magnetic refrigerants with similar transition temperature, ΔS_{m} in the present compound does not decrease at low temperature. Our result suggests that $GdFeO_3$ could be a potential material for magnetic refrigeration below 40 K.

6

Unusual critical behavior in double perovskite Gd_2CoMnO_6

6.1 Introduction

Double perovskites R_2MM$'$O$_6$ (R: rare-earth ions or Y, La; M, M': transition metal ions) have attracted considerable research interest due to their various fascinating properties like multiferroicity [66, 188, 189], spin-phonon coupling [190, 191, 192], cationic ordering [193, 194], colossal magnetoresistance [195], large magnetocapacitance, etc [52, 196]. These compounds crystallize either in monoclinic structure with P2_1/n space group for ordered state or in the orthorhombic Pbnm structure for disordered state [197]. Most of the ordered double perovskites exhibit ferromagnetism due to the superexchange interaction between the M^{2+} and M'^{4+} ions [198]. Even in the ordered state itself, some of the M and M' cations interchange their crystallographic positions and introduce antisite disorder. [190, 199, 200] Such disorders instigate additional AFM interactions in the form of M^{2+}-O-M^{2+} or M'^{4+}-O-M'^{4+} and, thus weaken the ferromagnetism.

There are several reports on magnetic and magnetodielectric properties of double perovskites R_2(Co/Ni)MnO$_6$, but majority of them addresses La-based systems [66, 188, 52, 201, 44]. As R changes from La to Lu, the reduction in size of rare-earth element causes significant modification in Co-O-Mn/Ni-O-Mn bond angle and bond length and as a consequence, the FM transition temperature (T_C) decreases [202] and multiple magnetic interactions develop in the system, leading to an inhomogeneous magnetic ground state, as observed in several perovskite manganites in the form of clustered or phase separated states [190, 199, 203].

Among the various forms of clustered phases, the "Griffiths-like" phase has drawn more attention due to its interesting magnetic response. The formation of Griffiths phase (GP) occurs below a characteristic temperature, called the Griffiths temperature (T_{GP}). For $T_C<T<T_{GP}$, the system is in an unusual magnetic state where the short-range FM clusters of different sizes exist [33, 204, 205, 206]. In this narrow range of temperature, magnetic properties show several characteristics such as, (i) the inverse susceptibility (χ^{-1}) starts to deviate in downward direction from the linear Curie-Weiss behavior just below T_{GP}, as temperature approaches T_C from above, (ii) χ^{-1} follows a power-law behavior [204, 206]

$$\chi^{-1}(T) = A\left(T - T_C^R\right)^{1-\lambda}, \tag{6.1}$$

where T_C^R is the critical temperature below which χ diverges and λ is an exponent such that $0<\lambda<1$ for $T_C^R<T<T_{GP}$ and $\lambda=0$ for $T > T_{GP}$ and (iii) the downturn in χ^{-1} gradually suppresses with increasing field strength and eventually disappears [204, 206].

In several magnetic systems, including perovskite-type manganites and cobaltites, the presence of GP has been experimentally verified [203, 204, 207]. The GP has also been reported in some double perovskites such as Tb_2NiMnO_6 [190], Pr_2CoMnO_6 [208], Ho_2NiMnO_6 [209] and Nd_2CoMnO_6 [210] etc., whereas Dy_2NiMnO_6 [211] and Lu_2NiMnO_6 [212] do not show GP-like behavior. The presence of "Griffiths-like" clustered phase in the above mentioned compounds has been claimed solely from the downturn behavior of $\chi^{-1}(T)$ curve slightly above the T_C [205]. However, this downturn in $\chi^{-1}(T)$ is not sufficient to claim the formation of GP in the temperature region $T_C<T<T_{GP}$. The analysis of critical behavior is one of the important techniques to confirm the GP formation [206, 205, 213].

In this work, we present the detailed analysis of critical behavior of ferromagnetic double perovskite Gd_2CoMnO_6 (GCMO). To the best of our knowledge, this is the first scaling analysis in double perovskite system to determine the nature of clustered phase. The critical exponents β, γ and δ, obtained through the scaling analysis of magnetization data and the magnetocaloric results, clearly demonstrate that "Griffiths-like" phase is absent in the studied system. Moreover, the deduced values of the exponents are quite far from any known universality class.

6.2 Experimental Details

The polycrystalline sample of GCMO was prepared by conventional solid-state reaction method using high purity Gd_2O_3 (99.9%), Co_3O_4 (99.9%) and $MnCO_3$ (99.9%) powders [198]. Before use, Gd_2O_3 was pre-heated at 950°C for 24 h. The starting materials were mixed thoroughly in an appropriate ratio, and heated at 1200°C in air for few days with intermediate grindings. Finally, the product was reground, pressed into pellets and sintered at 1350°C in air for 24 h. The phase

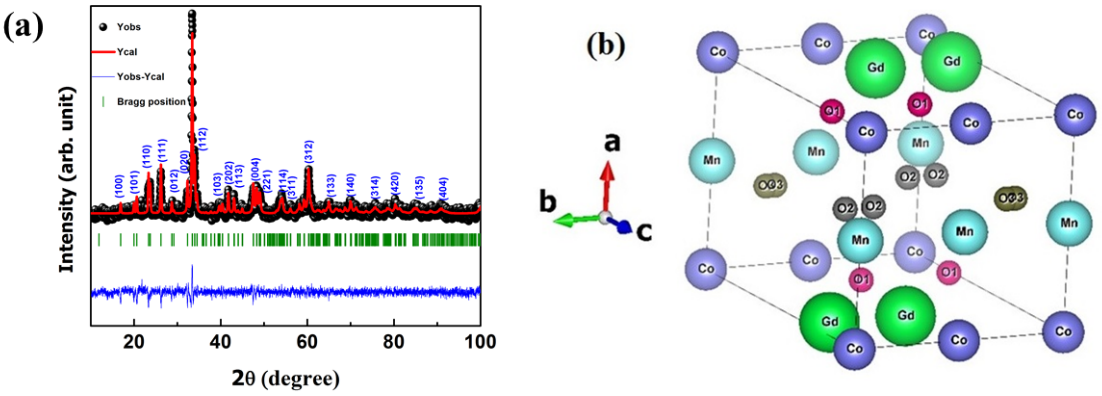

Figure 6.1: (a) The x-ray diffraction pattern and (b) the schematic crystal structure of Gd_2CoMnO_6.

purity and crystal structure of the samples have been determined by x-ray powder diffraction technique. The experimental x-ray intensity profile along with the theoretical fit and the Bragg positions are shown in Figure 6.1(a). All the peaks in the diffraction pattern can be indexed well with monoclinic unit cell having P21/n crystallographic symmetry [214]. The lattice parameters determined from Rietveld analysis are a =5.467, b =5.510, and c =7.651 Å with β=89.951°, which are close to the previously reported values [214]. The schematic crystal structure of GCMO has been shown in the Figure 6.1(b).

A small piece of rectangular shape sample of approximate dimensions $\sim 4\times 0.5\times 0.4$ mm^3 was cut from the polycrystalline pellet for dc magnetization (M) measurements in a 7 T SQUID-VSM (Quantum Design). The data for each isotherm were recorded in the field range of 0-7 T at different temperatures between 2 and 150 K and the temperature dependence of magnetization was measured in the range 1.8-390 K. To minimize the demagnetization effect, the magnetic field was applied along the longest dimension of the sample. For each isothermal magnetization measurement, the sample temperature was stabilized for 30 mins. Data were col-

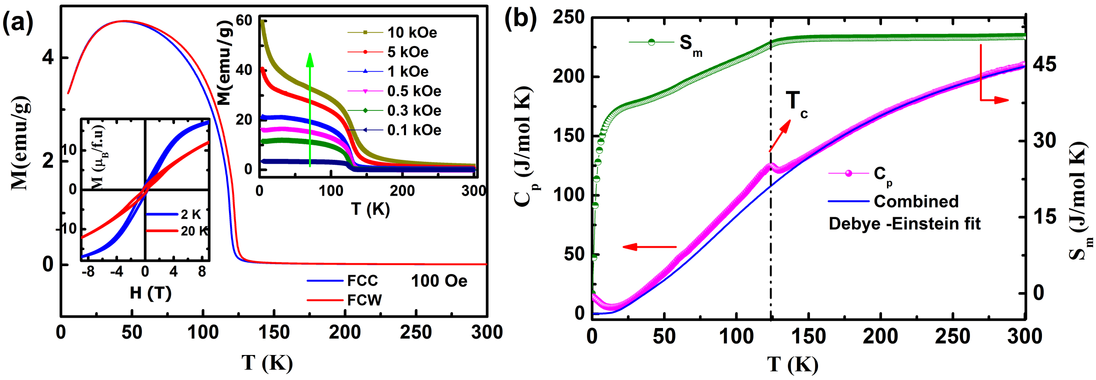

Figure 6.2: (a) The main panel shows the temperature (T) dependence of magnetization (M) of GCMO at H = 100 Oe for both field-cooled-cooling (FCC) and field-cooled-warming (FCW) conditions. The upper inset shows $M(T)$ curves for different H where the arrow indicates the direction of increase of magnetic field strength. The lower inset displays $M(H)$ hysteresis loop at 2 and 20 K. (b) T dependence of heat capacity (C_p) along with the combined Debye-Einstein model fit (solid line) and magnetic entropy (S_m) of GCMO. The arrow indicates the transition temperature T_C.

lected for both increasing and decreasing fields. We did not observe any difference in $M(H)$ between increasing and decreasing field above 114 K. Magnetization has been measured using two different protocols: (a) the field-cooled-cooling (FCC) magnetization and (b) the field-cooled-warming (FCW) magnetization. In FCC cycle, the measurement was performed during the cooling process under applied magnetic field. In FCW cycle, the sample was cooled down to lowest temperature in an applied magnetic field and the measurement was performed during the heating cycle. To check the saturation behavior, magnetization was measured at 2 K for fields up to 9 T in a PPMS (Quantum Design). The heat capacity measurement was done in a the same PPMS (Quantum Design) by relaxation method in the temperature range 5-300 K.

6.3 Results and Discussion

6.3.1 Temperature dependence magnetization and heat capacity

Figure 6.2(a) shows the temperature dependence of FCC and FCW magnetization for GCMO at a field of 100 Oe. In the PM state, M increases slowly with decreasing temperature down to $\approx$ 123 K. However, M increases sharply below 123 K, indicating the onset of long-range FM ordering. With further decrease in T, M continues to increase like a Brillouin function down to $\sim$43 K, below which M starts to decrease. Similar behavior in $M(T)$ has also been observed in other double perovskite systems [198, 199, 214, 215, 216]. The decrease in M at low temperature has been attributed to complex interplay of magnetic interaction of Gd and Mn/Co sublattices [198, 202, 214, 216]. Similar to the previous report a very weak thermal hysteresis has been observed between FCC and FCW magnetization cycles [217]. With the increase in magnetic field strength, the anomaly below 43 K progressively suppresses and M shows a sharp increase at low temperature for field above 1 kOe, as shown in the upper inset of Figure 6.2(a). This sharp increase in M is due to the contribution of large PM moment of rare-earth Gd^{3+} ion, which aligns along the direction of field above a threshold value. The lower inset of Figure 6.2(a) displays $M(H)$ hysteresis loops at low temperature well below T_C. Even at 2 K, we did not observe saturation-like behavior in $M(H)$ curve at high field up to 9 T. At 2 K and 7 T, the value of magnetization is 16.6 μ_B/f.u. The obtained value of M matches well with the previous reports [198, 214].

The FM ordering temperature T_C, estimated from the $M(T)$ curve is also confirmed through heat capacity (C_p) data as shown in Figure 6.2(b), where a peak has been observed at around 123 K [214]. As expected, no anomaly is seen in C_p curve at low temperature where M is observed to decrease. However, $C_p(T)$ curve shows an upturn below ∼20 K. Similar increase in C_p has also been reported earlier in single crystal of GCMO and other double perovskite compounds such as Tb_2CoMnO_6 [198, 214, 218] and attributed to the short-range AFM ordering of rare-earth moments. Thus this upturn in GCMO is due to the short-range AFM ordering of the Gd^{3+} moments. For understanding the nature of FM phase transition, we have estimated the magnetic entropy (S_m) using the expression, $S_m(T) = \int \left(\frac{C_m}{T}\right) dT$, where C_m is the magnetic contribution to heat capacity and has been calculated by subtracting the lattice part from the total heat capacity. The lattice heat capacity has been calculated using the combined Debye-Einstein model [74]. The variation of S_m with T is shown in Figure 6.2(b). The continuous change in $S_m(T)$ around T_C indicates that the FM transition is second-order in nature.

6.3.2 Magnetic susceptibility

The main panel of Figure 6.3(a) presents the temperature dependence of inverse dc susceptibility, χ^{-1} ($=H/M$), for various applied fields. At high temperature above ∼250 K, χ^{-1} increases almost linearly with T. However, below 250 K, χ^{-1} starts to deviate from the linear behavior and shows a downward curvature. Often, this faster decrease of χ^{-1} in the PM state has been attributed to the formation of short-range FM clusters [204, 205, 206, 213]. To check whether the clustered phase has the characteristics of GP, the T dependence of χ below T_{GP} has been analyzed in details. We observe that $\chi^{-1}(T)$ does not follow the power-law expression, as

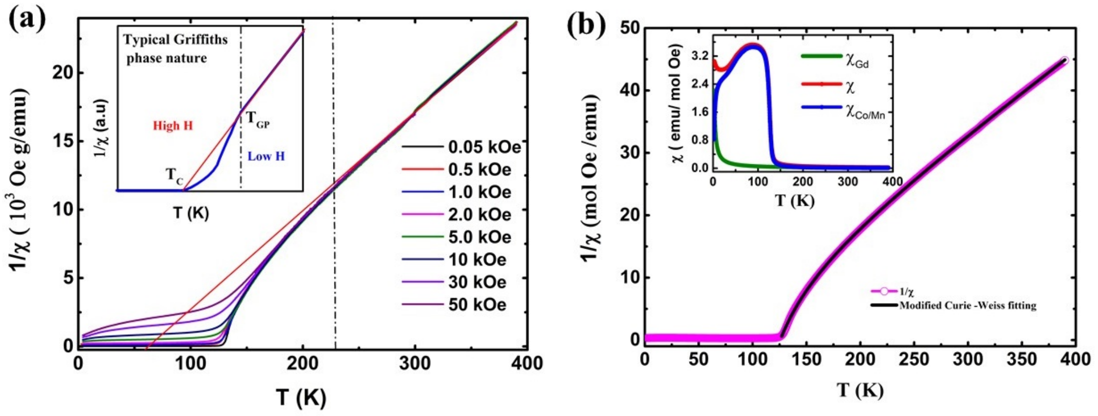

Figure 6.3: (a) The main panel shows the temperature dependence of inverse dc susceptibility ($\chi^{-1} = H/M$) of GCMO for different applied fields. The red line shows the linear fit to the Curie-Weiss law. The inset shows the expected nature of the Griffiths phase. (b) The main panel shows the temperature dependence of inverse dc susceptibility ($\chi^{-1} = H/M$) of GCMO at H= 500 Oe. The blue curve shows the modified Curie-Weiss fitting and the inset shows the contribution of the χ_{Gd} and $\chi_{Co/Mn}$ to the total experimental susceptibility χ.

described in Eq. (6.1), suggesting that the clustered phase is not "Griffiths-like". For the accurate determination of T_C^R and λ in GP, T_C^R should be varied in such a way so that λ becomes zero for $T > T_{GP}$ [204]. This criterion suggests that T_C^R should be very close to the temperature obtained by extrapolation of the high temperature linear part of $\chi^{-1}(T)$ to zero. In compounds where GP is observed, T_C^R is found to be slightly higher than T_C [204, 209]. However, the T_C^R (≈75 K) in GCMO is much lower than T_C (≈123 K), not consistent with the behavior expected for GP. For further confirmation of the nature of clustered phase, we have examined the effect of magnetic field on $\chi^{-1}(T)$, which is displayed in Figure 6.3(a). In case of GP, the downturn in $\chi^{-1}(T)$ curve gradually weakens with increasing field strength and disappears at high field, as shown schematically in the inset of Figure 6.3(a) [204, 205, 206, 213]. On the other hand, for GCMO, the downturn in χ^{-1} does not suppress even under application of magnetic field as high as 50 kOe. This kind of field dependence of χ^{-1} indicates "non-Griffiths-like" nature of the clustered phase [219].

The downward curvature in inverse susceptibility versus temperature plot in Figure 6.3(a) suggests that both rare-earth (Gd^{3+}) and transition metal ion (Co^{2+}/Mn^{4+}) sublattices contribute to the total susceptibility. Hence, we have used the modified Curie Weiss (CW) expression to incorporate the contribution of the individual sublattice to the total magnetic susceptibility,

$$\chi(T) = \chi_{RE} + \chi_{TM} = \frac{C_{RE}}{T} + \frac{C_{TM}}{T - \Theta_{TM}}, \tag{6.2}$$

where C_{RE} and C_{TM} are the Curie constants of the rare-earth and transition metal ion sublattices, respectively. Whereas the Θ_{TM} is the CW temperature for the Co^{2+}/Mn^{4+} sublattice. The subscripts RE and TM denote the parameters for rare-earth Gd^{3+} and transition metal sublattices, respectively. As Gd^{3+} moments do not show any long-range ordering down to 2 K, we have used CW temperature Θ_{RE}=0. Also, the Curie constant C_{RE} for the Gd sublattice was calculated using the theoretical value of effective paramagnetic moment μ_{eff}=15.8 μ_B/f.u and the Landé g-factor g=2. The measured susceptibility has been fitted with Eq. (2) and shown in Figure 6.3(b). It is clear from the figure that experimental data can be fitted with Eq. (2) over a wide temperature range. In this context, we would like to mention that similar type of fit has been used for GCMO and other compounds where both rare-earth and transition metal sublattices are present [209, 220, 221]. The fit yields Θ_{TM}=125.3 K, which is close to T_C and the effective paramagnetic moment of the Co^{2+}/Mn^{4+} sublattice is 5.4 μ_B/f.u., which is close to the theoretical value [220]. The contribution of each sublattice to the total susceptibility has also been plotted in the inset of Figure 6.3(b). The plots show that the contribution of

χ_{TM} is significantly larger as compared to χ_{RE} when T approaches T_C, i.e., in the the critical region. For example, χ_{TM}=2.9 emu/mol Oe and χ_{RE}=0.046 emu/mol Oe at 120 K. However, at low temperature where χ shows a sharp increase with decreasing temperature, Gd^{3+} moment dominates magnetic susceptibility. We have also calculated the contribution to magnetization due to Gd moment using the relation M_{Gd}=$\chi_{RE}H$ and it is found that the value of Gd^{3+} moment is less than 1% of the total moment in the critical region.

6.3.3 Field-induced metamagnetic transition

From the temperature and magnetic field dependence of magnetization and susceptibility, several groups reported multiple magnetic phase transitions in GCMO [216, 217, 222]. GCMO exhibits complex magnetic behavior due to strong competition between rare-earth and transition metal sublattices which is yet to understand. Also, some of the reported features such as metamagnetic transition, spin-glass behavior [217, 222, 223] appear to be sensitive, to some extent, on sample quality. For this reason, we have recorded $M(H)$ loop at different temperatures using our highly sensitive SQUID-VSM facility. The data were collected in a stable mode in a small interval of magnetic field. We did not observe any characteristics of metamagnetism associated with first-order transition even at very low applied magnetic field in the temperature range 100-115 K as shown in Figure 6.4(a). However, $M(H)$ curves show a weak hysteresis below 115 K. One representative plot is shown in Figure 6.4(b) at 110 K, which reflects the typical behavior of a ferromagnet. Similar to previous reports, however, a weak metamagnetic behavior has been observed at low temperature as shown in Figure 6.4(c) at 70 K as a representative

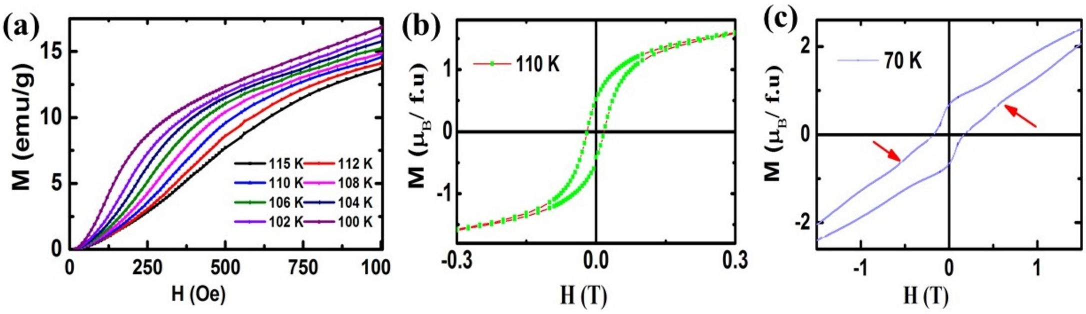

Figure 6.4: (a) Shows the low-field initial magnetization curves in the temperature range 100-115 K whereas (b) shows the $M(H)$ hysteresis loop at 110 K and (c) for 70 K for GCMO. The red arrow indicates the weak metamagnetic nature of the material at low field at 70 K.

[222, 217]. Above 80 K, the anomaly is too weak to detect, though the FM loop sustains (see Figure 6.4(b). We would like to mention that the anomaly associated with the metamagnetic transition in the present sample is much weaker as compared to that reported for sample with smaller magnetic moment and lower T_C [217]. Clark *et al.* first reported the field-induced metamagnetic transition below 115 K in pollycrystalline GCMO sample and explained this phenomenon on the basis of a transition between uncompensated antiferromagnetic and ferromagnetic state below T_C [222]. However, in single crystal, they did not observe metamagnetic transition above 70 K [222]. Moon *et al.* also mentioned that in their single crystal, the metamagnetic transition is absent above 100 K [214].

6.3.4 Critical behavior and scaling analysis

As there are no in-depth analysis of magnetic properties of GCMO such as critical behavior , etc. no consensus has been reached upon the nature of magnetic phase transitions in this system. The nature of FM to PM phase transition and the existence of GP-like clusters can also be studied through the detailed analysis of critical behavior. To investigate the critical behavior associated with FM transition, we have measured $M(H)$ isotherms in the temperature range 105 K$<T<$143 K and for fields up to 7 T. Few representative plots in the vicinity of T_C are shown in Figure 6.5(a). We observe that even at low field, M decreases monotonically with increase in temperature. This behavior is typical of a ferromagnet.

The $M(H)$ isotherms have been transformed into Arrott plots (M^2 versus H/M) which are shown in the lower inset of Figure 6.5(a) [224]. The positive slope of the Arrott plots indicates that the FM transition is second-order in nature [225]. In the vicinity of a second-order transition point, the diverging correlation length leads to the universal scaling laws for spontaneous magnetization (M_S), initial susceptibility (χ_0) and magnetization at T_C via a set of critical exponents β, γ and δ, which are defined as [31, 226],

$$M_S(0,t) \sim (-t)^{\beta}, \qquad t<0, \tag{6.3}$$

$$\chi_0{}^{-1}(0,t) \sim (t)^{\gamma}, \qquad t>0, \tag{6.4}$$

$$M(H,0) \sim (H)^{1/\delta}, \qquad t=0, \tag{6.5}$$

where t=$(T-T_C)/T_C$ is the reduced temperature. All the three exponents β, γ and δ are not independent of each other, rather they are related via the Widom scaling relation,

$$\delta = 1 + \frac{\gamma}{\beta}. \tag{6.6}$$

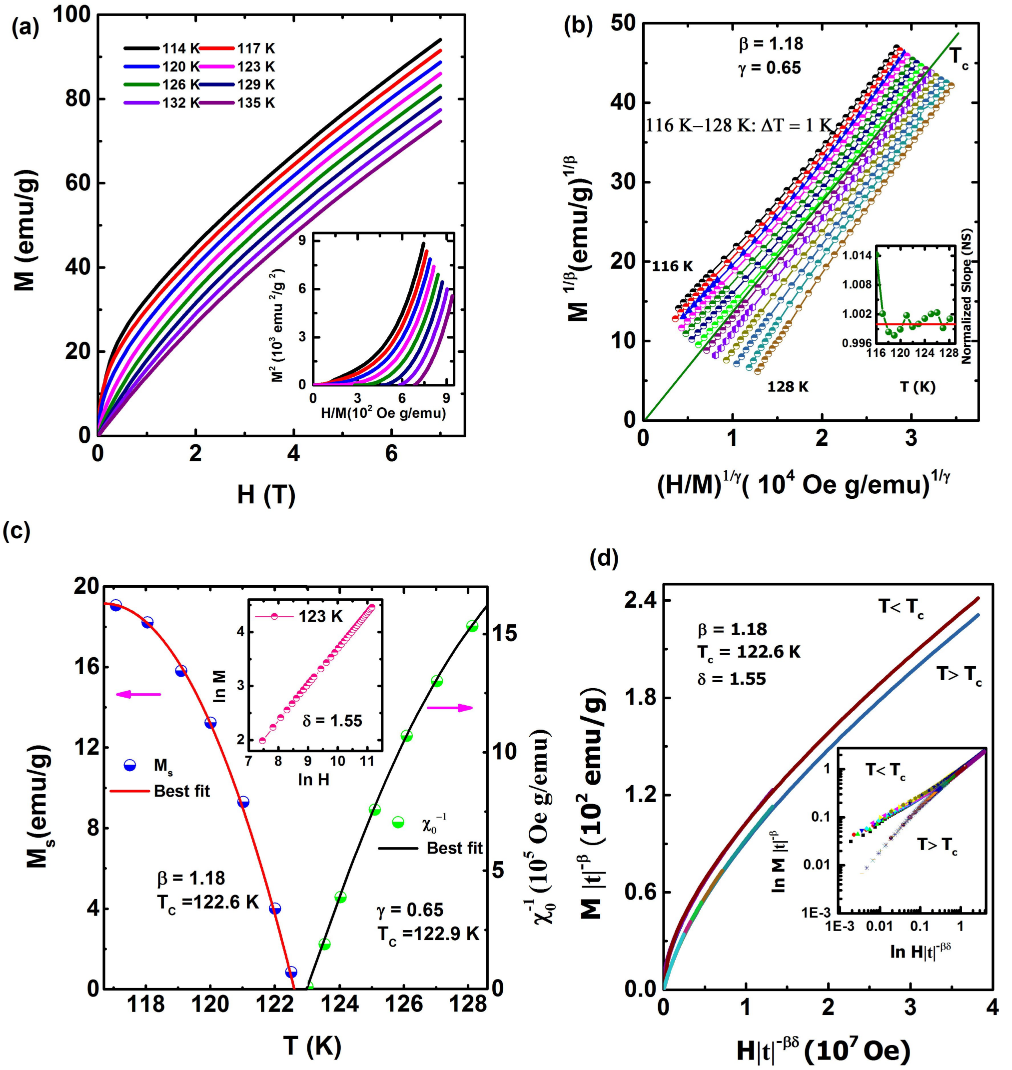

Figure 6.5: (a) $M(H)$ isotherms of GCMO between 114 K (top) and 135 K (bottom) in 3 K interval (data with increasing field are shown). The lower inset shows the Arrott plot (M^2 vs H/M) of $M(H)$ isotherms. (b) Modified Arrott plot [$M^{1/\beta}$ vs. $(H/M)^{1/\gamma}$] using $\beta = 1.18$ and $\gamma = 0.65$. The inset shows T dependence of normalized slope (NS). (c) Temperature dependence of spontaneous magnetization (M_S) and initial inverse susceptibility (χ_0^{-1}). The lines represent the best-fit curve according to **Eqs. (6.3)** and **(6.4)**. The inset shows log-log plot of $M(H)$ isotherm for 123 K, the nearest one to the critical isotherm. (d) Scaling plots below and above T_C according to **Eq. (6.7)**. The different symbols represent different temperatures. Inset shows the same plot in log-log scale.

Furthermore, the field and temperature dependence of magnetization in the critical regime obeys a universal scaling relation of the form,

$$M(H,t) = |t|^{\beta} f_{\pm} \left[\frac{H}{|t|^{(\beta\delta)}} \right], \tag{6.7}$$

where f_+ is for $t > 0$ and f_- is for $t < 0$.

To calculate the critical exponents and T_C, we use the modified Arrott plot based on the Arrott-Noakes equation of state,

$$\left(\frac{H}{M} \right)^{1/\gamma} = at + bM^{1/\beta}, \tag{6.8}$$

where a and b are constants [31, 226]. The Figure 6.5(b) shows almost parallel straight lines in the high field regime. During the least-squares fitting to the isotherms, the low-field data have been excluded because they represent mainly the rearrangement of magnetic domains. The convergence in the fitting is achieved for $\beta = 1.18$ and $\gamma = 0.65$. The obtained values of exponents are quite far from any conventional universality class.

Here, we would like to mention that in several related double perovskite systems, magnetization is reported to follow conventional scaling behavior. La_2NiMnO_6 and Y_2NiMnO_6 obey scaling behavior belonging to 3D Heisenberg and 3D Ising class, respectively [227, 228] while the values of critical exponents for Pr_2CoMnO_6 and Lu_2NiMnO_6 are close to that for mean field [229, 212]. From Figure 6.5(b), it is clear that an isotherm between 122 and 123 K will pass through the origin, suggesting T_C is very close to 122.5 K, consistent with T_C determined from the heat capacity data. To check whether the straight lines in Figure 6.5(b) are parallel to each other, we have plotted the normalized slope $NS(T)$=d$M^{1/\beta}$/d$(H/M)^{1/\gamma}$ for different isotherms as shown in the inset of Figure 6.5(b). The values of NS for different temperatures near T_C are close to 1, indicating that the isotherms in modified Arrott plot are almost parallel to each other. The intersections of these isotherms for $T<T_C$ on $M^{1/\beta}$ axis and for $T>T_C$ on $(H/M)^{1/\gamma}$ axis give the values of M_S and χ_0^{-1}, respectively. The temperature dependence of M_S and χ_0^{-1} are shown in Figure 6.5(c). The power-law fitting to M_S and χ_0^{-1} according to the Eqs. (6.3) and (6.4), respectively reveals β = 1.18±0.06 with T_C = 122.6±0.2 K and γ = 0.65±0.01 with T_C = 122.9±0.3 K. Another exponent δ has been determined from $M(H)$ curve at T = 123 K, the nearest one to the critical isotherm. The log-log plot of $M(H)$ curve at T = 123 K gives δ=1.55±0.03 [Eq.(6.5)], which is shown in the inset of Figure 6.5(c). With the obtained values of β, δ and T_C, we have plotted the scaling relation $M|t|^{-\beta}$ vs. $H|t|^{-\beta\delta}$, which is shown in Figure 6.5(d). Similar plot of the scaling relation in log scale has been shown in the inset of Figure 6.5(d). Depending on the sign of t, the magnetization data fall onto two branches of the curve. This suggests that the critical exponents and T_C are reasonably accurate. Moreover, one can see that the Widom scaling relation [Eq. (6.6)] is also satisfied [31]. It may be mentioned that the critical behavior of GCMO has also been analyzed after subtracting the Gd^{3+} moment ($\chi_{RE}H$) from the measured magnetization (not shown) and the critical exponents are found to be β=1.2, γ=0.64 and δ=1.53. Thus the change in the values of critical exponents is very small and within our experimental error.

In this work, the critical phenomenon has been studied on polycrystalline GCMO sample. In an anisotropic compound, the polycrystalline nature of the sample may affect the scaling behavior. For systems with strong magnetic anisotropy, the

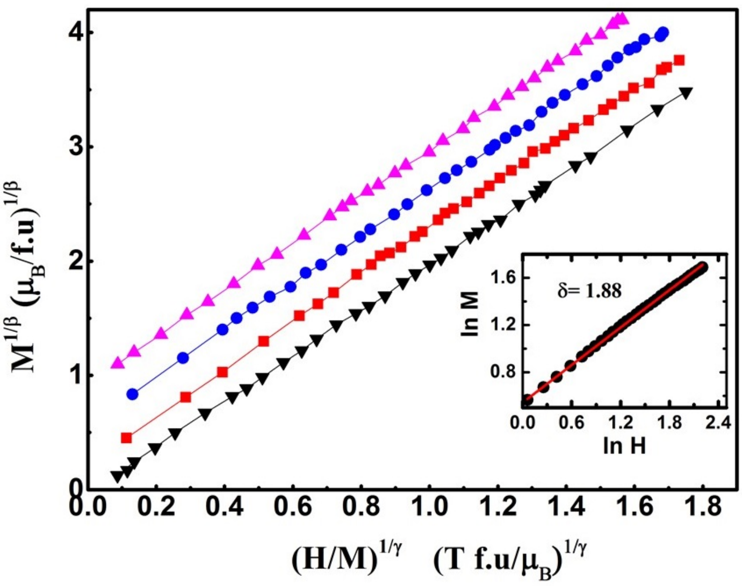

Figure 6.6: The modified Arrott plot [$M^{1/\beta}$ vs. $(H/M)^{1/\gamma}$] using β= 1.88 and γ=0.65 of the easy-axis magnetization data of GCMO single crystal. The magnetization data were taken from the Reference [214]. The inset shows the log-log plot of $M(H)$ isotherm close to T_C.

magnetization along the easy axis exhibits critical phenomenon, whereas the hard axis can show non-critical behavior. In such cases, the non-critical magnetization along hard axis becomes negligibly small and does not affect the analysis of critical behavior in polycrystalline sample. Experimental studies on GCMO single crystal reveal that the magnetic anisotropy in this system is strong [214]. We have analyzed the reported $M(H)$ isotherms along magnetic easy axis as well as hard axis of GCMO single crystal in the vicinity of FM transition [214]. The easy-axis magnetization is found to obey critical behavior similar to that we have observed in polycrystalline sample, whereas hard axis does not exhibit any critical behavior. Few $M(H)$ curves just below the T_C have been analyzed and observed that $(H/M)^{1/\gamma}$ versus $M^{1/\beta}$ plot, as shown in Figure 6.6, becomes linear for β and γ close to 1.18 and 0.65, respectively. We have also determined the exponent δ =1.88

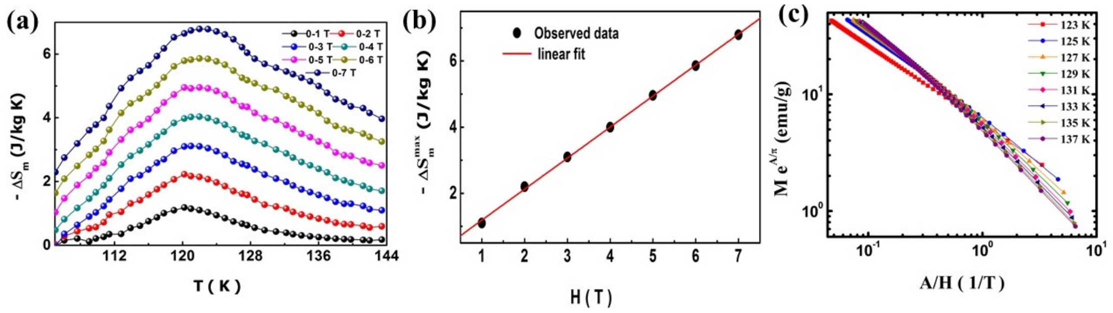

Figure 6.7: (a) Temperature dependence of magnetic entropy change (ΔS_m) for different field change. (b) H dependence of maximum magnetic entropy change (ΔS_m^{max}). The solid line corresponds to linear fit. (c) Data collapse of magnetization M(h, t) followed by equation (11) in logarithmic scale.

from the log-log plot of $M(H)$ very close to T_C for applied field parallel to the easy axis of magnetization ($H \parallel$ c) which is close to our polycrystalline data $\delta = 1.55$.

6.3.5 Scaling analysis from magnetocaloric behaviour

Generally, the common method to identify the critical behavior of materials undergoing second order phase transition is the modified Arrott plots. But the critical exponent may also be determined through magnetocaloric analysis. Another method based on the field dependence of magnetic entropy change can be used to show the intrinsic relation between MCE and the universality class. According to the approach proposed by Oesterreicher and Paker [230]. The change in magnetic entropy (ΔS_m) has been calculated using the Maxwell relation [231]. The temperature dependence of ΔS_m for different magnetic fields is shown in Figure 6.7(a). $\Delta S_m(T)$ exhibits a peak at T_C ($\sim$ 123 K). The maximum value of ΔS_m, ΔS_m^{max}, is observed to follow a power-law behavior [232]

$$\Delta S_m^{max} \approx H^n. \tag{6.9}$$

We have plotted ΔS_m^{max} as a function of field in Figure 6.7(b). Figure shows that ΔS_m^{max} increases almost linearly with H, which means n is close to 1. According to the Arrott-Noakes equation of state, n is related to critical exponents β and γ through the relation [232]

$$n = 1 + \frac{\beta - 1}{\beta + \gamma}. \tag{6.10}$$

Using the value of β and γ as calculated from magnetization scaling analysis, we deduce $n = 1.09$, an excellent agreement with the above mentioned experimental value, indicating that the values of critical exponents are unambiguous and self-consistent. On the basis of the mean-field approach, the field dependence of the magnetic entropy change at the Curie temperature corresponds to $n = 2/3$ [233, 234]. The deviation of n value from the mean-field behavior refers basically to the presence of magnetic inhomogeneities in the vicinity of transition temperature [235].

6.3.6 Scaling analysis from analytical method

In case of GP, the conventional scaling theory breaks down due to the non-analytical nature of magnetization. From the Yang-Lee theory of phase transition, one can derive an approximate magnetization scaling relation for phase transition from FM state to GP, which is given by [213]

$$\frac{M(h,t)}{\mu} = e^{-\left[\frac{A(t)}{\pi}\right]} \left[f_M\left(\frac{A(t)}{h}\right) + O(h) \right], \tag{6.11}$$

where

$$f_M(x) = -g_0 Im\left[exp(ix/2)E_1(ix/2)\right], and E_1(x) = \int_x^\infty \frac{e^{-t}}{t}dt.$$

μ is the magnetic moment of individual spin, h=$\mu H/k_B T_C$, and $A(t)$=$A_0 t^{2-\beta_r}$, where A_0 is constant and β_r is the order parameter exponent whose value reflects the universality class. Following Eq. (6.11), we have tried to collapse $M(H)$ isotherms of GCMO onto a single curve by plotting $Me^{A/\pi}$ versus A/H. By varying the parameters β_r and A_0, we have tried to achieve the convergence in fitting and the best scaling plot is obtained for β_r = 1.8 and A_0 = 0.98, which is shown in Figure 6.7(c). It is clear from the figure that the data points can't be scaled at all, suggesting that GP does not exist in GCMO. It may be mentioned that the presence of GP in $La_{0.7}Ca_{0.3}MnO_3$ has been confirmed through such type of scaling analysis [33, 205, 213]. The asymptotic behavior of $M(h,t)$ in Griffiths ferromagnet reveals [213]

$$M(h,t) \to \frac{\mu g_0 \pi}{2},$$

as h and A tend to zero. Thus, there should be a discontinuity in $M(h,t)$, which is characterized by the large value of the exponent δ. Indeed, the critical exponent δ is found to be unusually large in several colossal magnetoresistive compounds due to the presence of GP [33, 205, 236]. On the contrary, the small value of δ in GCMO implies the non-Griffiths-like behavior of the clustered phase.

6.4 Conclusion

In conclusion, we have studied the nature of clustered phase, in double perovskite GCMO. The evolution of inverse susceptibility with temperature and external field are not consistent with Griffiths phase. Furthermore, the calculated values of critical exponents β, γ, and δ associated to ferromagnetic to paramagnetic phase transition are far from any known existing universality class.

7

Nonlinear Magnetodielectric and Magnetocaloric properties of Double Perovskite Ho_2FeCoO_6

7.1 Introduction

The double perovskite compounds of the series R_2MM$'$O$_6$ [R= rare-earth element and M and M$'$ are the transition metals] are FM due to the double-exchange interaction between the two transition metal ions via the oxygen atoms [197, 198, 200, 237]. The magnetocaloric (MCE) properties have been reported for this series of compounds R_2(Ni/Co)MnO$_6$ [R= Gd, Dy, Ho and Er] [198, 238] for low temperature [200]. Also the compounds R_2(Ni/Co)MnO$_6$ show large magnetodielectric effect near room temperature [44]. But less attention has been paid to the Fe based compounds in this series. If such a rare double perovskite material can be found where these two effects (magnetodielctric and MCE) coexist that would be rather promising.

We have chosen Ho_2FeCoO_6 (HFCO) as our study compound to investigate its unseen magnetodielectric and magnetocaloric properties in details. The magnetodielctric effect (MD) of this compound shows a nonlinear nature in the low temperature region below 45 K and a large response of its MD has been observed at the high temperature due to the grain boundary effect. The observed magnetocaloric parameters are also reasonable and larger than the other reported DP compounds [238] for its application at the low temperature cryogenic regime.

7.2 Experimental details

The polycrystalline Ho_2FeCoO_6 sample was prepared by conventional solid-state reaction method as described previously [239]. The phase purity and crystal structure of the sample have been determined by x-ray powder diffraction with the same source at room temperature. The Rietveld refinement was used for the structural analysis of diffraction pattern of powdered Ho_2FeCoO_6 sample with Fullprof software. The experimental x-ray intensity profile along with the theoretical fit is shown in main panel of Figure 7.1(a). All the observed peaks in the diffraction pattern can be indexed well with orthorhombic unit cell having Pbnm crystallographic symmetry [239]. The schematic crystallographic structure has been shown in Figure 7.1(b). Where the Fe/Co are occupied in the same position and they are orientated along the crystallographic c axis and the rare-earth ions are sandwiched between the two transition metals layers [239]. We did not observe any peak due to the impurity phase within the x-ray resolution. The lattice parameters were determined from the Rietveld profile analysis are a =5.234, b =5.505,

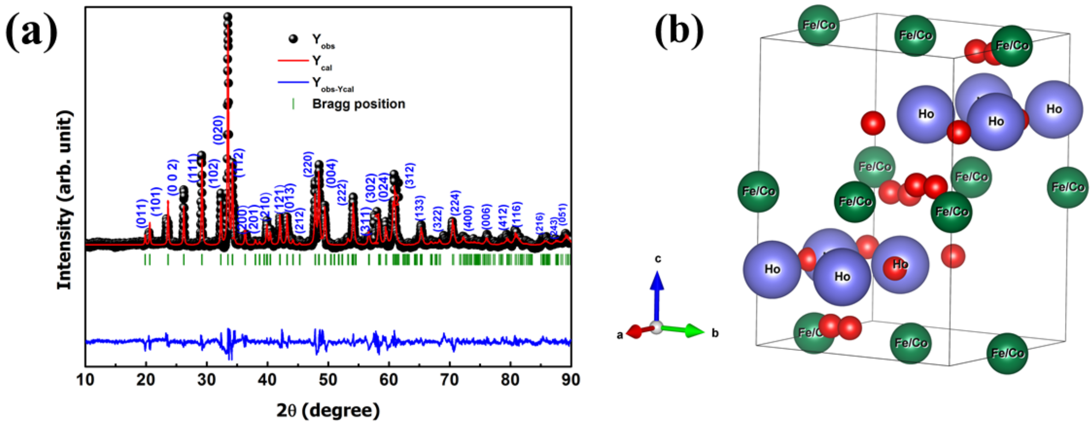

Figure 7.1: (a) The x-ray diffraction pattern of the polycrystalline powder and (b) the crystallographic structure of Ho_2FeCoO_6 compound.

and c =7.475 Å which are closed to the reported values [239]. The temperature and magnetic field dependence magnetization have been carried out using the same SQUID-VSM. The dielectric measurement has been done in a cryostat (Cryogenic limited) with 9 T magnet and with an ultra precision AH 2700A capacitance bridge.

7.3 Results and discussions

7.3.1 Temperature dependence magnetization

The main panel of Figure 7.2(a) shows the temperature dependence magnetization in the range (2-350 K) for the applied field 500 Oe. Near 270 K and 45 K, an AFM phase transition (T_N) of Fe^{3+} spins has been observed. Also an anomaly due to the continuous spin reorientation of Fe^{3+} spins has been seen as reported earlier [239]. With decreasing T, the moment (M) increased sharply below 15 K due to the dominating superexchange interactions of rare-earth Ho^{3+} moments. Both the

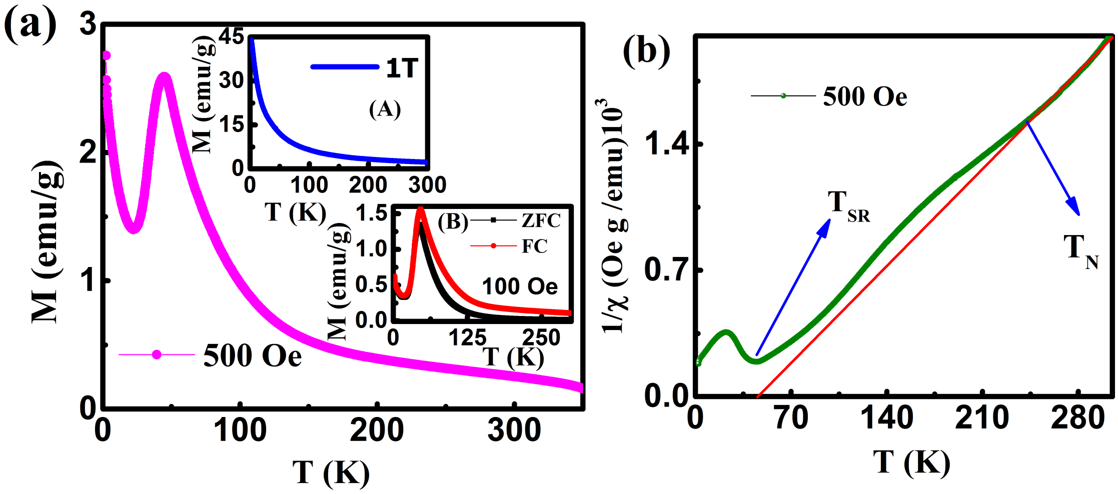

Figure 7.2: (a) The main panel shows the temperature dependence magnetization for 500 Oe field where as the inset (A) shows the $M(T)$ for the magnetic field 1 T and (B) shows the $M(T)$ for 100 Oe for both ZFC and FC cycle. (b) Shows the inverse χ with temperature for 500 Oe of Ho_2FeCoO_6 compound.

transitions (T_N and T_{SR}) become broader with increasing the magnetic field and for the critical field near 1 T the transition diminished as shown in the inset (A) of the Figure 7.2(a). Interestingly, large hysteresis between ZFC and FC protocol over a wide temperature range at low field below $\leq$ 300 Oe has been also observed as shown in the inset (B) of Figure 7.2(a). This is due to the presence of mixed magnetic phase in the region 45 K$\leq$T$\leq$270 K [239]. The temperature dependence of inverse susceptibility χ^{-1} has been plotted for 500 Oe field as shown in the Figure 7.2(b). χ^{-1} has been fitted well with the Curie Weiss fitting [200] down to 270 K. Below 270 K, χ^{-1} starts to deviate from its linear behaviour , which corresponds to the antiferromagnetic ordering of Fe^{3+} (T_N^{Fe}). The deduced values of the fitting parameters θ_{cw} and P_{eff} are very close to the earlier reports [239].

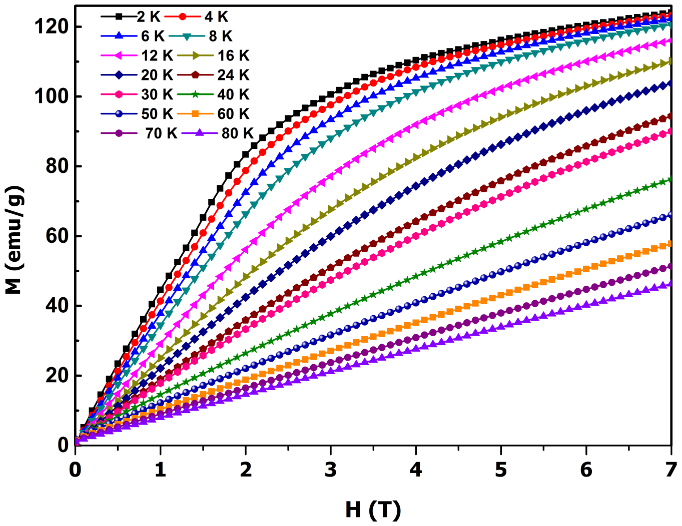

Figure 7.3: Isothermal magnetization plot of the some representative temperature for Ho_2FeCoO_6 compound.

7.3.2 Isothermal magnetization

To observe the field evolution of the studied compound HFCO, we have measured the isothermal magnetization for 0-7 T in the temperature range 2-80 K as shown in the Figure 7.3. At low temperature below 10 K, the magnetization has been increased smoothly upto the critical field 2.5 T and there has no tendency of saturation at high field upto 7 T. The value of the magnetization has been reached to the value 120 emu/g at 2 K & 7 T .

7.3.3 Dielectric properties

In the main panel of Figure 7.4(a), the temperature dependence of real part of dielectric constant ϵ' has been shown for zero applied magnetic field and 1 kHz frequency (f) in the temperature range 2-300 K. The dielectric properties that arise from the dipolar relaxation, which is originated from the asymmetric hopping of

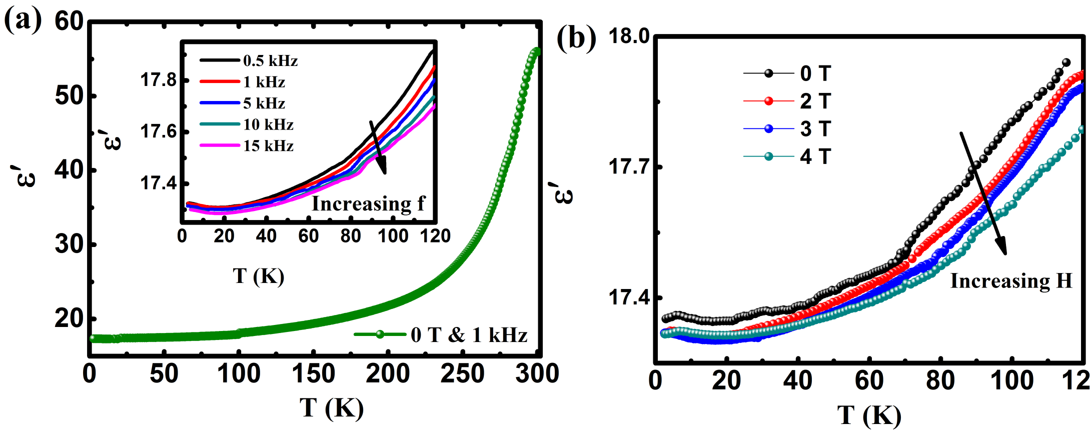

Figure 7.4: (a) The main panel shows the temperature dependence of the ϵ' for 0 T and 1 kHz and the inset shows the frequency variation of the ϵ'. (b) Shows the field dependency of ϵ' at frequency 1 kHz for Ho_2FeCoO_6.

charge carriers under the applied electric field [240], is shown below 120 K in the Figure 7.4(a). At low temperature, the dielectric constant becomes temperature and frequency independent as shown in the inset of Figure 7.4(a), which indicates the intrinsic dielectric properties of the material. The strong frequency dependency and large variation of ϵ' with T, above 120 K denote the extrinsic polarization due to Maxwell-Wagner effect [241]. The systematic variation of the dielectric properties with magnetic field below 120 K has been shown in the Figure 7.4(b) where we can see the variation of ϵ' with magnetic field.

7.3.4 Magnetodielectric properties

With the help of the field dependence dielectric constant, we have calculated the magnetodielectric effect of the material. The magnetodielectric effect is defined as MD [$\Delta\epsilon'(H)/\epsilon'(0)$] % = [($\epsilon'(H)$ - $\epsilon'(0))/\epsilon'(0)$]% where $\epsilon'(H)$ and $\epsilon'(0)$ are the dielectric constant under applied and zero magnetic field, respectively. Figure 7.5 demonstrates the magnetic field variation of dielectric constant measured at

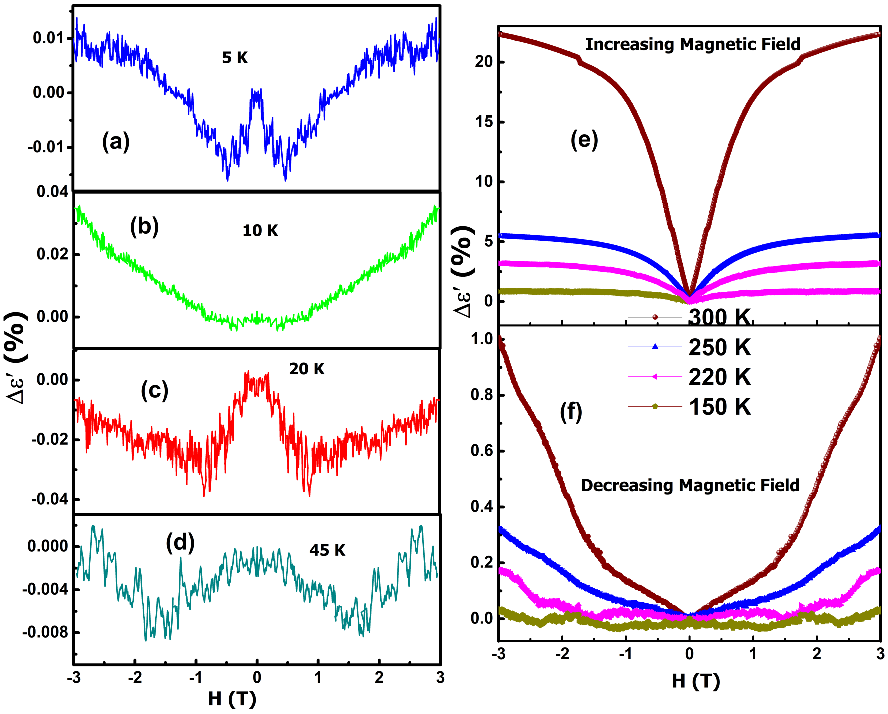

Figure 7.5: (a-d) The variation of $\Delta\epsilon'(H)$ with the magnetic field for some representative temperatures in the range 5-45 K for Ho_2FeCoO_6. (e-f) The variation of $\Delta\epsilon'(H)$ with the magnetic field for some representative temperatures at high temperature for both increasing and decreasing in magnetic field respectively.

1 kHz between the magnetic field +3 T and -3 T at various temperatures. $\Delta\epsilon'$ changes in a highly nonlinear fashion in presence of an external magnetic field. At 5 K, during increasing magnetic field, $\Delta\epsilon'$ decreases linearly upto 0.5 T, then increases up to the highest field of 3 T as shown in the Figure 7.5(a). We did not observe any hysteresis in $\Delta\epsilon'$ within the accuracy of our experimental set up. The deep valley in $\Delta\epsilon'$ tends to suppressed gradually as the temperature is increased as shown in Figure 7.5(b). Below 10 K, the magnetodielctric effect has been governed by the short range rare earth ions, may be some field induced phase transition of the short range ordered Ho^{3+} moments effects the dielectric constant. Above 10 K, the magnetodielctric effect has been suppressed as Figure 7.5(c) and

disappeared complectly above the T$_{SR}$ as shown in Figure 7.5(d), suggesting that the magnetic moment of Ho^{3+} ions and the dielectric effect of the materials are interconnected. The non linear magnetodielectric effect between 10 K $< T <$ 45 K is due to the interaction between the Ho^{3+} and transition metal ions, suggesting that the magnetic exchange interaction between the Ho^{3+}- Fe^{3+} ions and the dielectric properties of the material are interconnected. Note that, the large rare earth moments plays a major role in the enhanced magnetodielctric functionality in the low temperature. Similar to the another DP compound Gd_2NiMnO_6 [242]. The investigation of comprehensive magnetic structures and magnetic field dependence of dielectric properties on the single crystalline HFCO, has been desirable to clarify the exact origin of highly nonlinear magnetodielectric behaviour in the low temperature regime. At high temperature 150-300 K, the magnetodielectric effect $\Delta\epsilon'$ develops again as shown in the Figure 7.5(e) and (f). At 150 K the $\Delta\epsilon'$ reached to the value $\approx$ 0.5 % for 3 T. At 300 K, the maximum of $\Delta\epsilon'$ at 3 T increases four times and $\Delta\epsilon'$ exhibits a smooth bending in the small magnetic field regime. The large hysteresis in $\Delta\epsilon'$ has been also observed during the magnetic field cycling for the multi domain orientation of the grain boundaries. For example, at 300 K, $\Delta\epsilon'$ goes to 23 % and 1% during increasing and decreasing field respectively. The much enhanced magnetodilectric effect even above T_N^{Ho} originates from the extrinsic effect accompanied by the increase of dielectric loss which is influenced by grain boundaries or material-electrode interfaces.

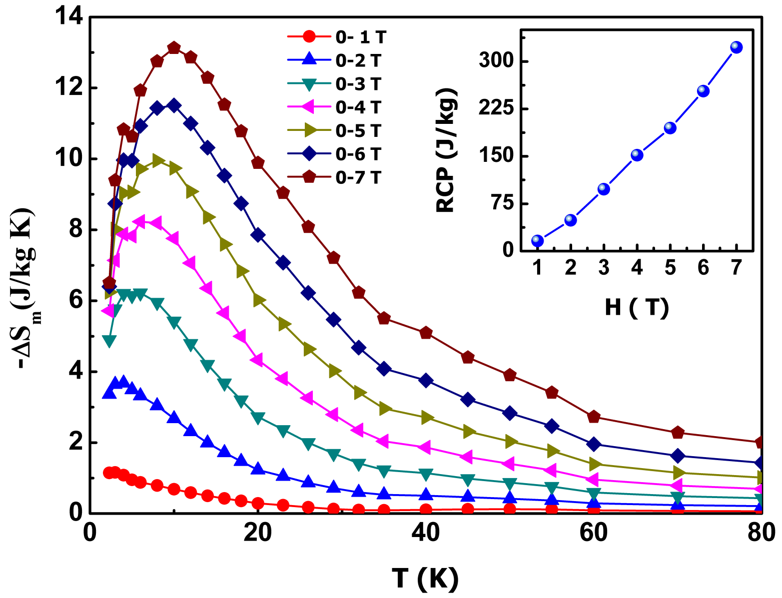

Figure 7.6: The main panel shows the temperature dependence of isothermal magnetic entropy change (-ΔS_m) where as the inset shows the magnetic field dependence of the refrigeration cooling power (RCP) for $\mathrm{Ho_2FeCoO_6}$.

7.3.5 Magnetocaloric properties

We have also calculated the magnetocaloric parameter, the isothermal magnetic entropy change -ΔS_m, from the measured M-H data as shown in the Figure 7.3 with the help of the Maxwell equation [74]. The temperature dependence -ΔS_m has been plotted in the main panel of the Figure 7.6. The -ΔS_m curve shows the maximum value near T = 10 K and then decreases at both side of T. The peak position of the -$\Delta S_\mathrm{max}(T)$ shifts towards high T with increasing the magnetic field which indicates the increasing the Zeeman coupling between the $\mathrm{Ho^{3+}}$ and external magnetic field as well as Schottky entropy associated with the $\mathrm{Ho^{3+}}$ moments. The maximum value of the ΔS_m reaches to 13 J/kg K for the 0-7 T. We have also calculated the refrigeration cooling power (RCP) from the FWHM of the ΔS_m curve. The value of RCP reached to the maximum value 300 J/kg for 0-7 T. This value of ΔS_{max} is comparable as well as larger than the value of the several reported materials [243, 244] including the double perovskite compounds R_2CoMnO$_6$ [R= Dy, Ho and Er] [238] in the same temperature range and for the field change 0-7 T. But the value is less than the other DP compounds Gd$_2$(Co/Ni)O$_6$ and other reported compounds like TmZn, HoPdIn and ErMn$_2$Si$_2$ [244].

7.4 Conclusion

In summary we have explored the magnetic, magnetodielectric and magnetocaloric properties of the double perovskite Ho$_2$CoFeO$_6$ compound. Highly nonlinear change of the dielectric constant ϵ' in presence of the external magnetic field was accomplished at the low temperature regime. Whereas for a high temperature enhanced magnetodielectric effect has been observed due to the extrinsic polarization from the grain boundaries. Besides the obtained magnetocaloric parameters also suggest for magnetic refrigerant like several other materials at low temperature.

8

Summary

8.1 Summary

In this chapter, we summarize the works presented in the previous chapters of the thesis. The main motivation of the present thesis is to investigate the magnetic, thermal and dielectric properties of some less studied rare-earth transition metal based oxides.

In **Chapter 1**, we first introduced the novel magnetic oxides in a general manner and their physical properties are discussed with the basis of some fundamental aspect of physics point of view as well as their modern technological applications are highlighted. Some mechanisms like Dzylonshki Moriya interaction, single-ion anisotropy and magnetic frustration behind these interesting magnetic properties of the studied materials are discussed thoroughly. The basic principles and applications of magnetocaloric phenomenon are described. Besides, a general overview of the theory of phase transition and critical phenomena of the double perovskite compounds have been addressed. Finally the magnetodielectric properties of the oxide materials are addressed briefly.

In **Chapter 2**, an overview of solid state reaction method for preparation of polycrystalline sample and the description of single crystal growth using traveling solvent float zone method is presented. The basic principle of operation of the characterization tools such as powder x-ray and Laue diffraction are demonstrated. Different magnetic and physical property measurement techniques are described in this chapter.

In **Chapter 3**, We have investigated the nature of magnetic ground state of the new members of RCrTiO$_5$ (R = Dy and Ho) series of compounds through dc magnetization and heat capacity measurements. Due to the strong competition between the Cr^{3+} and R^{3+} sublattice moments, several intriguing phenomena like magnetization reversal have been observed when the magnetic state is probed at low field. In both the systems, the Cr^{3+} sublattice undergoes a long-range antiferromagnetic ordering below T=139 K with a weak FM moment perpendicular to c axis as evident from the hysteresis in $M(H)$ curve. For both the samples, the strong coupling between the two magnetic sublattices is manifested in the temperature dependence of coercive field. Another interesting phenomenon, the spin reorientation transition, has been observed below T_{SR} = 37 K, where the easy axis of FM moment of Cr^{3+} starts to rotate from one crystallographic axis toward another in DyCrTiO$_5$ but no such transition has been observed in HoCrTiO$_5$. The other members of RCrTiO$_5$ series do not show such kinds of interesting magnetic properties.

In **Chapter 4**, We report the role of exchange frustration on the magnetocaloric properties of GdCrTiO$_5$. Due to the highly frustrated nature of magnetic interactions, in GdCrTiO$_5$, the long-range antiferromagnetic ordering of Gd^{3+} moments occurs at a much lower temperature $T_N = 0.9$ K and the magnetic cooling power enhances dramatically relative to that observed in several geometrically frustrated systems. Below 5 K, the isothermal magnetic entropy change ($-\Delta S_{\mathrm{m}}$) is found to be 36 J kg^{-1} K^{-1} for a field change (H) of 7 T. These magnetocaloric parameters are significantly larger than that reported for several potential magnetic refrigerants, even for small and moderate field changes. The present result not only suggests that $GdCrTiO_5$ could be considered as a potential magnetic refrigerant at cryogenic temperatures but also promotes further studies on the role of exchange frustration on the magnetocaloric effect. In contrast, only the role of geometrical frustration on the magnetocaloric effect has been previously reported theoretically and experimentally investigated on very few systems.

In **Chapter 5**, we have investigated the magnetocaloric properties of single crystalline $GdFeO_3$ have been investigated in the temperature range 2–36 K by magnetization and heat-capacity measurements. Remarkably large and reversible magnetic entropy change, $\Delta S_{\mathrm{m}} = -52.5$ J/kg K, has been observed for a field change of 0–9 T. The adiabatic temperature change, T_{ad}, is also found to be very large, 22 K, slightly above the antiferromagnetic ordering temperature ($T_{\mathrm{N}}^{Gd} = 2.5$ K) of the Gd^{3+} moment, for a field change of 0–8 T. These magnetocaloric parameters remain large down to the lowest temperature measured and are significantly larger than that reported for the other members of rare-earth (R) ortho-ferrites ($R\mathrm{FeO}_3$) and several potential magnetic refrigerants in the same temperature range. Both ΔS_{m} and T_{ad} are also quite large for a small field change. The large values of magnetocaloric parameters suggest that $GdFeO_3$ could be considered as a potential refrigerant in low-temperature magnetic refrigeration technology, such as liquefaction of hydrogen in the fuel industry.

In **Chapter 6**, we have shown that ferromagnetic double perovskite Gd_2CoMnO_6 exhibits the characteristics of clustered phase, which are quite different from that of Griffiths phase observed in several perovskite compounds. The critical exponent δ for Gd_2CoMnO_6, determined from magnetization scaling analysis, comes out to be very small ($\delta = 1.55 \pm 0.03$). The small value of δ suggests that the continuous ordering is slow, indicating non-Griffiths-like cluster formation in the studied system, which is further supported by the evolution of susceptibility with temperature and magnetic field. Also, the observed values of all the three exponents β ($= 1.18 \pm 0.06$), $\gamma(= 0.65 \pm 0.01)$, and δ are far from any existing universality class and they deviate from the mean-field values in the opposite direction to that for the conventional universality.

In **Chapter 7**, We have investigated the magnetic, magneto-dielectric and magnetocaloric properties of the double perovskite (DP) compound Ho_2FeCoO_6. The Neel temperature T_N and the spin reorientation transition T_{SR} have been observed near 270 and 45 K respectively. At low temperature below T_{SR} highly nonlinear variation of the dielectric constant $\Delta\epsilon'$ (H) has been observed under application of the magnetic field. At high temperature the enhancement of $\Delta\epsilon'$ (H) has been observed due to grain boundaries. An extremely large hysteresis in $\Delta\epsilon'$ (H) in presence of magnetic field suggests the strong irreversible electrical dipole orientation along the applied field. During the increasing and decreasing the magnetic field, $\Delta\epsilon'$ (H) reached to 23% and just 1%, respectively at 300 K for the magnetic field change 3 T. The isothermal magnetic entropy change -ΔS_m and refrigeration cooling capacity (RCP) have been reached to 13 J/kg K and 325 J/kg respectively for 7 T magnetic field below 10 K.

Bibliography

[1] J. A. Blanco *et al.*, Eur. J. Php. **16** 195-198 (1995).

[2] T. Moriya *et al.*, Phys. Rev. Lett. **4**, 228 (1960).

[3] I. Dzialoshinski *et al.*, J. Phys. Chem. Solids. **4**, 241 (1958).

[4] P.W. Anderson *et al.*, Phys. Rev. **115**, 2 (1959).

[5] A. H. Morrish *et al.*, Canted Antiferromagnetism: Hematite (World Scientific, Singapore), (1994).

[6] C. G. Shull *et al.*, Phys. Rev. **83**, 333 (1951).

[7] L. Neel *et al.*, Rev. Mod. Phys. **25**, 58 (1953).

[8] J. Miyawaki *et al.*, Phys. Rev. B **96**, 214420 (2017).

[9] Y. Tokura *et al.*, Rep. Prog. Phys. **77** 076501 (2014).

[10] R. G. Mohammadi *et al.*, Phys. Rev. B **101**, 075421 (2020).

[11] M. Schmitt *et al.*, Nature Commu. **10** 2610 (2019).

[12] V. Vleck *et al.*, Phys. Rev. **52**, 1178 (1937).

[13] J. Dubowik *et al.*, Phys. Rev. B **54**, 2 (1996).

[14] L. K. Varga *et al.*, J. Mag. Mag. Mater. **254-255** 477-479 (2003).

[15] W. Sucksmith *et al.*, Proc. Roy. Soc. (London) **A225**, 362 (1954).

[16] B. D. Cullity *et al.*, Introduction to Magnetic Materials (Addison-Wesley, Reading, MA), (1972).

[17] T. M. Perekalina *et al.*, SOVIET PHYSICS JETP **19**, 6 (1964).

[18] C. Andersson *et al.*, Phys. Rev. Lett. **99**, 177207 (2007).

[19] G.H. Wannier *et al.*, Phys. Rev. **79**, 357 (1950).

[20] G. Toulouse *et al.*, Commun. Phys. **2**, 115 (1977).

[21] J. Vannimenus *et al.*, J. Phys. C **10**, L537 (1977).

[22] B. D. Gaulin *et al.*, Hyperfine Interactions **85** 159-171 (1994).

[23] M. J. Harris *et al.*, Phys. Rev. Lett. **79**, 2554 (1997).

[24] P. Tierno *et al.*, Phys. Rev. Lett. **116**, 038303 (2016).

[25] H. Szymczak *et al.*, ACTA PHYSICA POLONICA A **114**, 1 (2008).

[26] O. A. Petrenko *et al.*, AIP Conference Proceedings **479**, 90 (1999).

[27] H. Ren *et al.*, Phys. Rev. B **51**, 15885 (1995).

[28] S. R. Mohapatra *et al.*, J. Mater. Sci. Nanomater. **2** 1 (2017).

[29] S. Rufo *et al.*, Physica A **518**, 349-362 (2019).

[30] M. Rutonjski *et al.*, arXiv:2002.10773.

[31] N. Khan *et al.*, Phy. Rev. B **82**, 064422 (2010).

[32] A. Oleaga *et al.*, Phys. Rev. B **92**, 024409 (2015).

[33] M. B. Salamon *et al.*, Phys. Rev. Lett. **88**, 197203 (2002).

[34] C. V. Mohan *et al.*, J. Mag. Mag. Mater. **183** 348-355 (1998).

[35] H. Yanagihara *et al.*, Phys. Rev. B **65**, 092411 (2002).

[36] C. Meneghini *et al.*, Phys. Rev. Lett. **103**, 046403 (2009).

[37] G. D. Ngantso *et al.*, Current Applied Physics **16**, 211-219 (2016).

[38] R. Saha *et al.*,Phys. Rev. B **94**, 014428 (2016).

[39] M. Kaur *et al.*, Electronic Materials Letters **14**, 370-375 (2018).

[40] S. Tiwari *et al.*, Sci. Rep. **8**, 11619 (2018).

[41] I. E. Dzyaloshinskii *et al.*, Sov. Phys. JETP **10**, 628-629 (1960).

[42] D. N. Astrov *et al.*, Sov. Phys. JETP **11**, 708-709 (1960).

[43] X. Shen *et al.*, NPG Asia Materials **11**, 50 (2019).

[44] J. Krishnamurthy *et al.*, AIP Conf. Proc. No. **1447**, 1235 (2012).

[45] P. Yanda *et al.*, Phys. Rev. B **100**, 104417 (2019).

[46] N. Mufti *et al.*, Phys. Rev. B **83**, 104416 (2011).

[47] A. Maignan *et al.* Phys. Rev. B **97**, 161106(R) (2018).

[48] Y. Fang *et al.*, Sci. Rep. **4**, 3860 (2014).

[49] J. Hwang *et al.*, Phys. Rev. B **85**, 024415 (2012).

[50] S. Ghara *et al.*, Phys. Rev. B **95**, 094404 (2017).

[51] Y. Cao *et al.*, Sci. Rep. **7**, 14079 (2017).

[52] N. S. Rogado *et al.*, Adv. Mater. **17**, 2225 (2005).

[53] Y. Q. Lin *et al.*, Ceramics **94**, 782-787 (2011).

[54] R. J. Hill, *The Rietveld Method*, Oxford University Press (1995).

[55] J. R.-Carvajal, *An Introduction to the Program FullProf 2000*, Laboratoire Leon Brillouin, CEA-CNRS, Saclay (2001).

[56] *Magnetic Property Measurement System: SQUID VSM User Manual*, Quantum Design, USA (2009).

[57] *Physical Properties Measurement System User Manual*, Quantum Design, USA (2002).

[58] *Physical Property Measurement System, Heat Capacity Option User's Manual*, Part Number 1085-150, H-1 (Quantum Design).

[59] M. Balli *et al.*, Crys. **7**, 44 (2017).

[60] G. R. Blake *et al.*, Phys. Rev. B **71**, 214402 (2005).

[61] Y. Noda *et al.*, J. Phys.: Condens. Matter **20**, 434206 (2008).

[62] T. C. Han *et al.*, J. Apl. Phys. **99**, 08J508 (2006).

[63] Y. Ishii *et al.*, Phys. Rev. B **93**, 064415 (2016).

[64] S. Wakimoto *et al.*, Physica B **404**, 2513 (2009).

[65] J. M Liu *et al.*, J. Adv. Diel. **2**, 1530003 (2015).

[66] J. Hwang *et al.*, Phys. Rev. B **85**, 024415 (2012).

[67] G. Buisson *et al.*, J. Phys. Chem. Solids **31**, 1171 (1970).

[68] J. Saha *et al.*, J. Magn. Magn. Mater. **360**, 34 (2014).

[69] E. B. Guedes *et al.*, J. Alloy. Compd. **724**, 67 (2017).

[70] X. L. Qian *et al.*, Physica B **495**, 1 (2016).

[71] S. Kori *et al.*, Phys. Rev. B **91**, 144403 (2015).

[72] T. Basu *et al.*, J. Appl. Phys. **118**, 234103 (2015).

[73] T. Basu *et al.*, Phys. Rev. B **96**, 184431 (2017).

[74] M. Das *et al.*, Phys. Rev. B **98**, 104420 (2018).

[75] V. V. Mazurenko *et al.*, Phys. Rev. B **78**, 195110 (2008).

[76] H. Wu *et al.*, Phys. Rev. B **90**, 144415 (2014).

[77] J. P. Bolletta *et al.*, Phys. Rev. B **98**, 134417 (2018).

[78] A. H. Cooke *et al.*, J. of Phys. C: Solid State Phys. **7**, 3133 (1974).

[79] L. D. Tung *et al.*, Phys. Rev. B **75**, 104404 (2007).

[80] H. C. Nguyen *et al.*, Phys. Rev. B **52**, 324 (1995).

[81] Y. Ren *et al.*, Phys. Rev. B **62**, 6577 (2000).

[82] E. W. Gorter *et al.*, Phys. Rev. **90**, 487 (1953).

[83] R. Pauthenet *et al.*, J. Appl. Phys. **29**, 253 (1958).

[84] N. Menyuk *et al.*, Phys. Rev. Lett. **4**, 119 (1960).

[85] P. Mandal *et al.*, Phys. Rev. B **82**, 100416 (R) (2010).

[86] S. Mahana *et al.*, J. Phys. D: Appl. Phys. **51**, 305002 (2018).

[87] Y. Su *et al.*, J. rare earth **29**, 1060 (2011).

[88] S. A. Uporov *et al.*, J. Mater. Sci. **48**, 7673 (2013).

[89] T. Yamaguchi *et al.*, J. Phys. Chem. Solids **35**, 479 (1974).

[90] G. R. Haripriya *et al.*, J. Phys.: Condens. Matter **29**, 475804 (2017).

[91] F. Pomiro *et al.*, Phys. Rev. B **94**, 134402 (2016).

[92] M. Das *et al.*, Phys. Rev. B **96**, 174405 (2017).

[93] Y. S. Vishnyakov *et al.*, Phys. Rev. B **93**, 094422 (1970).

[94] A. Midya *et al.*, Phys. Rev. B **93**, 094422 (2016).

[95] Z. Y. Zhao *et al.*, Phys. Rev. B **89**, 224405 (2014).

[96] L. Li *et al.*, Appl. Phys. Lett. **100**, 152403 (2012).

[97] A. Midya *et al.*, Phys. Rev. B **84**, 235127 (2011).

[98] R. M. Bozorth *et al.*, Phys. Rev. Lett. **1**, 3 (1958).

[99] A. J. Berton *et al.*, Appl. Phys. **39**, 1367 (1968).

[100] A. McDannald *et al.*, J. Appl. Phys. **114**, 113904 (2013).

[101] A. McDannald *et al.*, Phys. Rev. B **91**, 224415 (2015).

[102] S. K. S. Patel *et al.*, J. Mater. Chem. C **6**, 526 (2018).

[103] V. Singh *et al.*, Phys. Rev. B **82**, 054417 (2010).

[104] A. Jaiswal *et al.*, J. Phys. Chem. C **115**, 2954 (2011).

[105] F. Radu *et al.*, Nat. Commun. **3**, 1728 (2012).

[106] A. Duran *et al.*, Phys. Rev. Mater. **2**, 014409 (2018).

[107] R. Padam *et al.*, J. Phys. Condens. Matter **29**, 055803 (2017).

[108] A. H. Morrish *et al.*, The Physical Principles of Magnetism (IEEE Press, New York) **344**, 310 (2001).

[109] K. A. Gschneidner *et al.*, Rep. Prog. Phys. **68**, 1479 (2005).

[110] O. Gutfleisch *et al.*, Adv. Mater. **23**, 821 (2011).

[111] B. G. Shen *et al.*, Adv. Mater. **21**, 4545 (2009).

[112] B. F. Yu *et al.*, Int. J. Refrig. **26**, 622 (2003).

[113] J. Liu *et al.*, Nature Mater. **11**, 620 (2012).

[114] O. Tegus *et al.*, Nature **415**, 150 (2002).

[115] M. Foldeaki *et al.*, J. Appl. Phys. **77**, 3528 (1995).

[116] V. K. Pecharsky *et al.*, Phys. Rev. Lett. **78**, 4494 (1997).

[117] V. K. Pecharsky *et al.*, J. Magn. Magn. Mater. **167**, L179 (1997).

[118] H. Zeng *et al.*, Bull. Mater. Sci. **34**, 825 (2011).

[119] P. J. V. Ranke *et al.*, Phys. Rev. B **58**, 18 (1998).

[120] J. C. Patnino *et al.*, Intermetal. **64**, 59 (2015).

[121] L. Li *et al.*, Appl. Phys. Lett. **100**, 152403 (2012).

[122] A. Rostamnejadi *et al.*, J. Magn. Magn. Mater. **323**, 2214 (2011).

[123] M. Baazaoui *et al.*, Mater. Lett. **65**, 2093 (2011).

[124] R. Mondal *et al.*, J. Appl. Phys. **113**, 17A930 (2013).

[125] E. Bruck *et al.*, J. Magn. Magn. Mater. **310**, 2793 (2007).

[126] H. Wada *et al.*, Appl. Phys. Lett. **79**, 3302 (2001).

[127] E. Bruck *et al.*, J. Mag. Mag. Mater. **290**, 8 (2005).

[128] P. Mukherjee *et al.*, Adv. Funct. Mater. **27**, 1701950 (2017).

[129] P. Sarkar *et al.*, Appl. Phys. Lett. **92**, 182506 (2008).

[130] Y. J. Ke *et al.*, Sci. Rep. **6**, 19775 (2016).

[131] K. Y. Jiao *et al.*, Chin. Phys. B **24**, 037501 (2015).

[132] Y. Cao *et al.*, J. Appl. Phys. **119**, 063904 (2016).

[133] R. Huang *et al.*, Appl. Phys. Lett. **103**, 162412 (2013).

[134] M. Shao *et al.*, Solid. State. Commun. **152**, 947 (2012).

[135] E. K. G. Lorusso *et al.*, Adv. Mater. **25**, 4653 (2013).

[136] S. Pakhira *et al.*, Phys. Rev. B **94**, 104414 (2016).

[137] M. E Zhitomirsky *et al.*, Phys. Rev. B **67**, 104421 (2003).

[138] S. S. Sosin *et al.*, Phys. Rev. B **71**, 094413 (2005).

[139] M. Greenblatt *et al.*, J. Solid State Chem. **10**, 371 (1974).

[140] J. Hwang *et al.*, Phys. Rev. B **85**, 024415 (2012).

[141] T. J. Sato *et al.*, Phys. Rev. B **68**, 014432 (2003).

[142] T. Katsufuji *et al.*, Phys. Rev. B **64**, 104419 (2001).

[143] T. Katsufuji *et al.*, Phys. Rev. B **66**, 134434 (2002).

[144] B. Paul *et al.*, Phys. Rev. B **95**, 054103 (2017).

[145] M. Balli *et al.*, Appl. Phys. Lett. **108**, 102401 (2016).

[146] G. Heng *et al.*, Chin. Phys. B **22**, 057502 (2013).

[147] A. Midya *et al.*, J. Appl. Phys. **116**, 223905 (2014).

[148] S. Roy *et al.*, Appl. Mater. **4**, 026102 (2016).

[149] A. Midya *et al.*, Appl. Phys. Lett. **101**, 132415 (2012).

[150] K. Dey *et al.*, J. Mater. Chem. C. **5**, 1646 (2017).

[151] L. H. Yin *et al.*, J. Mater. Chem. C. **4**, 11198 (2016).

[152] N. B. Amor *et al.*, J. Alloys Compd. **563**, 28 (2013).

[153] N. B. Amor *et al.*, J. Sup. Nov. Magn. **26**, 3455 (2013).

[154] X. Moya *et al.*, Nat. Phys. **11**, 202 (2015).

[155] E. Palacios *et al.*, Phys. Rev. B **90**, 214423 (2014).

[156] S. Y. Li *et al.*, Phy. Rev. Let. **95**, 156603 (2005).

[157] J. D. Song *et al.*, Phy. Rev. B. **96**, 174425 (2017).

[158] J. D. Song *et al.*, Phy. Rev. B. **95**, 224419 (2017).

[159] P. A. Sharma *et al.*, Phys. Rev. Lett. **93**, 177202 (2004).

[160] X. Zhao *et al.*, Appl. Phys. Lett. **108**, 242405 (2016).

[161] X. M. Wang *et al.*, Phys. Rev. B **82**, 094405 (2010).

[162] Y. Yang *et al.*, Chem. Commun. **51**, 7317 (2015).

[163] K. Berggold *et al.*, Phys. Rev. B **76**, 094418 (2007).

[164] M. Balli *et al.*, Appl. Phys. Lett. **104**, 232402 (2014).

[165] S. J. Yuan *et al.*, Phys. Rev. B **87**, 184405 (2013).

[166] S. Cao *et al.*, Sci. Rep. **4**, 5960 (2014).

[167] A. V. Kimel *et al.*, Nature (London) **429**, 850 (2004).

[168] H. J. Zhao *et al.*, J. Phys.: Condens. Mater. **26**, 472201 (2014).

[169] H. Wu *et al.*, Phys. Rev. B **90**, 144415 (2014).

[170] Y. Tokunaga *et al.*, Phys. Rev. Lett. **112**, 037203 (2014).

[171] Y. Tokunaga *et al.*, Nat. Mater. **8**, 558 (2009).

[172] Y. Tokunaga *et al.*, Phys. Rev. Lett. **101**, 097205 (2008).

[173] S. Geller *et al.*, J. Chem. Phys. **24**, 1236 (1956).

[174] G. W. Durbin *et al.*, J. Phys. C: Solid State Phys. **10**, 1975 (1977).

[175] F. Arfat *et al.*, Afr. Phys. Rev. **3**, 0006 (2009).

[176] Z. Y. Zhao *et al.*, Phys. Rev. B **83**, 014414 (2011).

[177] J. D. Cashion *et al.*, J. Phys. C: Solid State Phys. **3**, 1612 (1970).

[178] M. A. Gilleo *et al.*, J. Chem. Phys. **24**, 1239 (1956).

[179] H. J. Zhao *et al.*, Nat. Commun. **8**, 14025 (2017).

[180] A. Kumar *et al.*, Phys. Rep. **556**, 1 (2015).

[181] T. Bora *et al.*, J. Appl. Phys. **114**, 033906 (2013).

[182] O. V. Billori *et al.*, J. Phys.: Condens. Matter **28**, 476003 (2016).

[183] P. Gupta *et al.*, Inorg. Chem. **54**, 9509 (2015).

[184] A. H. Cooke *et al.*, J. Phys. C: Solid State Phys. **7**, 3133 (1974).

[185] R. Skomki *et al.*, J. Rare Earth **27**, 4 (2009).

[186] G. Gorodetsky *et al.*, Phys. Rev. **135**, A97 (1964).

[187] K. Rubi *et al.*, Appl. Phys. Lett. **104**, 032407 (2014).

[188] J. Meng *et al.*, Phys. Chem. Chem. Phys. **18**, 23613 (2016).

[189] J. Su *et al.*, Appl. Mater. Inter. **7**, 13260 (2015).

[190] H. S. Nair *et al.*, J. Appl. Phys. **110**, 123919 (2011).

[191] P. N. Lekshmi *et al.*, Mater. Sci. Forum **830-831**, 513 (2015).

[192] R. B. M. Filho *et al.*, Appl. Phys. Lett. **102**, 192902 (2013).

[193] J. Blasco *et al.*, Phys. Rev. B **93**, 214401 (2016).

[194] G. King *et al.*, J. Mater. Chem. **20**, 5785 (2010).

[195] R. N. Mahato *et al.*, J. Appl. Phys. **107**, 09D714 (2010).

[196] L. Y. Wang *et al.*, J. Am. Ceram. Soc. **97**, 2024 (2014).

[197] H. Y. Zhou *et al.*, J. Phys.: Condens. Matter **29**, 145701 (2017).

[198] J. K. Murthy *et al.*, J. Phys. D: Appl. Phys. **48**, 355001 (2015).

[199] A. K. Singh *et al.*, Solid State Commun. **242**, 74 (2016).

[200] H. S. Nair *et al.*, J. Appl. Phys. **116**, 123907 (2014).

[201] R. Masrour *et al.*, Chin. Phys. B **25**, 087502 (2016).

[202] M. Nasir *et al.*, ACS Appl. Electron. Mater. **1**, 141 (2019).

[203] M. Triki *et al.*, J. Solid. State Chem. **201**, 63 (2013).

[204] D. Bhoi *et al.*, J. Phys. Chem. C **117**, 16658 (2013).

[205] M. B. Salamon *et al.*, Phys. Rev. B **68**, 014411 (2003).

[206] W. Jiang *et al.*, Phys. Rev. B **77**, 064424 (2008).

[207] S. M. Zhou *et al.*, J. Appl. Phys. **114**, 163903 (2013).

[208] W. Liu *et al.*, J. Appl. Phys. **116**, 193901 (2014).

[209] T. Chakraborty *et al.*, J. Phys.: Condens. Matter **29**, 025804 (2017).

[210] R. R. Das *et al.*, J. Alloys Compd. **773**, 770 (2019).

[211] S. A. Ivanov *et al.*, J. Mater. Sci.: Mater. Electron. **29**, 18581 (2018).

[212] L. Zhang *et al.*, J. Alloys Compd. **763**, 613 (2018).

[213] P. Y. Chan *et al.*,Phys. Rev. Lett. **97**, 137201 (2006).

[214] J. Y. Moon *et al.*, Sci. Rep. **7**, 16099 (2017).

[215] R. I. Dass *et al.*, Phys. Rev. B **67**, 014401 (2003).

[216] M. Retuerto *et al.*, Inorg. Chem. **54**, 10890 (2015).

[217] J. Krishna Murthy *et al.*, J. Alloys Compd. **719**, 341 (2017).

[218] J. Y. Moon *et al.*, Phys. Rev. B **98**, 174424 (2018).

[219] C. He *et al.*, Phy. Rev. B **76**, 014401 (2007).

[220] R. C. Sahoo *et al.*, J. Mag. Mater. **460**, 409-417 (2018).

[221] P. Mandal *et al.*, Phy. Rev. B **65**, 144506 (2002).

[222] A. Marsh *et al.*, Philosophical Magazine **19:159**, 449-463 (1969).

[223] X. L. Wang *et al.*, Solid State Commun. **118**, 27-30 (2001).

[224] A. Arrott *et al.*, Phys. Rev. Lett. **19**, 786 (1967).

[225] B. K. Banerjee *et al.*, Phys. Lett. **12**, 16-17 (1964).

[226] H. Eugene Stanley *et al.*, Science (Introduction to Phase Transitions and Critical Phenomena) (Oxford University Press, New York) **176**, 502 (1971).

[227] X. Luo *et al.*, J. Phys.: Condens. Matter **20**, 465211 (2008).

[228] H. Nhalil *et al.*, AIP Con. Proc. **1728**, 020184 (2016).

[229] I. N. Bhattia *et al.*, Phys. B Cond. Mat. **558**, 59-64 (2019).

[230] H. Oesterreicher *et al.*, J. Appl. Phys. **55**, 4336 (1984).

[231] V. K. Pecharsky *et al.*, Phys. Rev. Lett.**78**, 4494 (1997).

[232] V. Franco *et al.*, Appl. Phys. Lett. **89**, 222512 (2006).

[233] M. Pekala *et al.*, J. Appl. Phys. **108**, 113913 (2010).

[234] H. Oesterreicher *et al.*, J. Appl. Phys. **55**, 4334 (1984).

[235] T. L. Phan *et al.*, Solid State Commun. **167**, 49 (2013).

[236] W. Jiang *et al.*, Phys. Rev. Lett. **99**, 177203 (2007).

[237] S. H. Oh *et al.*, J. Phys. D: Appl. Phys. **48**, 445001 (2015).

[238] Y. Jia *et al.*, Ceramics International **43**, 15856 (2017).

[239] G. R. Haripriya *et al.*, J. Phys. Cond. Matter **29**, 475804 (2017).

[240] A. R. V. Hippel *et al.*, Dielectrics and Waves (MIT Press, Cambridge, MA), (1966).

[241] D. O. Neill *et al.*, Appl.Phys. Lett. **77**, 1520 (2000).

[242] S. H. Oh *et al.*, J. Phys. D: Appl. Phys. **48**, 445001 (2015).

[243] J. J. Mboukama *et al.*, Physica B **536**, 505-509 (2018).

[244] H. Drulis *et al.*, Sol. Sta. Communi. **151**, 1240 (2011).